



The University of
Nottingham

UNITED KINGDOM · CHINA · MALAYSIA
Department of Electrical and Electronic Engineering
Faculty of Engineering

Strategies to Model and Reduce High Frequency Copper Losses in Electrical Traction Machine

Eraldo Preci

Submitted to the University of Nottingham for the degree of Doctor of Philosophy

In memory of my mother.

Since I was a child, she taught me and made me understand
the importance of having an education.

ACKNOWLEDGEMENT

My thanks go to all those who helped and contributed to realise and complete the Ph.D. project discussed in this work.

My first debt of gratitude must go to Professor Chris Gerada, who believed in me and gave me the opportunity to start this journey.

A special thanks goes to my supervisors Professor Giampaolo Buticchi and Doctor David Gerada who supported me along these years with many precious suggestions to overcome the difficulties on my way. Even if he was not formally my supervisor, I would thank Professor Michele Degano for his constant contribution in all research activities that I did.

I would also like express my gratitude to Professor Davide Barater and Doctor Stefano Nuzzo for their scientific support and their hospitality during the period as visiting Ph.D. student at the University of Modena and Reggio Emilia.

Heartfelt thanks go to Prof. Paolo Bolognesi for the "transfer of knowledge" provided during my MSc years. He is always source of inspiration and his love for research caught on with me since the first moment when I have met him.

My warmest thankfulness goes to my father: thousands of pages are not enough to thanks him for the sacrifices which he did for me and to always support me in all decisions.

Finally, thanks to Melania who walked close to me along this journey and to have always been a point of reference during difficulties and have helped me with the right words in the right moment.

Abstract

Nowadays, one of the challenges in transport electrification is the reduction of the components' size and weight for improving the power density. This is often achieved by designing electrical machines with higher rotational speeds and excitation frequencies. In addition, the converter needs to control the machine over a wide speed range given by the mission profile.

However increase of the electrical frequency presents some drawbacks as well: the losses can increase significantly leading to some thermal fault if not considered at design stage; in addition the use of converters could lead to some fault to the winding insulation materials because of the uneven voltage distribution due to the pulse width modulation, which can cause overvoltage in specific portions of the winding.

With regards to losses, the main components can be identified in iron and copper losses. To reduce the iron losses big investments are needed in term of materials and technology, being possible to reduce them using exotic ferromagnetic materials with a very low thickness, which comes at a cost. Copper losses can be reduced by adopting smart distribution strategies and optimised layouts instead.

In this thesis two main winding types have been investigated in detail: the random distributed wires and the hairpin technology. The first one, is mainly adopted in large volume production lines where the stator's design is the same for all the batches, where each winding manufactured can present differences in strands distribution because of the non ideal distribution of the wires in the slot. This leads to different winding losses and manufacturing uncertainties. A method to predict the losses of random distributed windings is proposed in this thesis, resulting in a better understanding of the physics behind the phenomena and minimising their estimation errors. This aspect has been experimentally validated by using custom made trial windings and motorettes, representative of real electrical machines for automotive applications. The hairpin winding concept has been investigated, looking at reducing the copper losses occurring at high frequency, common in high-speed applications. An hairpin topology has been proposed

and as a result of the work, a peak 28% reduction has been achieved and experimentally validated, with respect to the classical hairpin distribution.

Thesis Outline

The thesis collects the work published in the papers listed below. The mainstream of the research over the PhD programme is related to the physical phenomena which occurs into the winding when high frequency sources has been applied to the machine.

Chapter 1. General description of the electric machine assembly has been done, the components needed to realize it are listed. The winding topologies present in the industry market have been discussed, the wire insulation types are introduced as well.

Chapter 2. The main losses source in the electrical machines are explained, the aim of this chapter is to give the basis to evaluate these contributes. In addition, the contributes of the high frequency copper losses are physically explained thanks also with some simple finite element simulations.

Chapter 3. This chapter describe the electrical machine used as a reference for our study on the winding. A numerical tool chain has been realized, described and used to select the best electrical machine for a given specification. Based to the key performance indicator the electrical topology has been selected after rounds of optimization performed automatically by the developed tool.

Chapter 4. Focus on the high frequency copper losses for the random winding is paid in this chapter. An analytic model for a prompt copper losses estimation is proposed and validated via finite element. A detailed numerical model able to catch the copper losses for each strand has been made. A statistical method able to consider the strands position has been described and experimentally validated.

Chapter 5. The high frequency copper losses within hairpin winding has been treated. An analytical model derived from the one described in section 4 has been presented and validated via finite element. An academic case study has been used to evaluate the fill factor and slot number of pin layers to the losses for different level of frequency.

Chapter 6. A comparison between the experimental copper losses between different configurations of hairpin and random winding has been presented. In addition, a new winding topology has been discussed, considering electromagnetic and manufacturing aspects compared to the standard ones.

Chapter 7. The content of the chapter is voltage distribution within the windings caused by the PWM. The physic phenomena is described, a numerical tool through the combination between finite element software and Simulink/Matlab has been presented and experimentally validated und different load and voltage conditions.

List of Scientific Publications

- I. E. Preci *et al.*, "Rectangular and Random Conductors: AC Losses Evaluations and Manufacturing Considerations," *IECON 2020 The 46th Annual Conference of the IEEE Industrial Electronics Society*, Singapore, 2020, pp. 1076-1081. doi: 10.1109/IECON43393.2020.9254278.

- II. T. Transi, M. Murataliyev, M. Degano, E. Preci, D. Gerada and C. Gerada, "Influence of Rotor Design on Electromagnetic Performance in Interior Permanent Magnet Machines," *IECON 2020 The 46th Annual Conference of the IEEE Industrial Electronics Society*, Singapore, 2020, pp.1021-1026. doi: 10.1109/IECON43393.2020.9255237. ** This work received the Second Prize Paper Award of the Electrical Machines Technical Committee of IEEE IES.

- III. E. Preci *et al.*, "Experimental Statistical Method Predicting AC Losses on Random Windings and PWM Effect Evaluation," in *IEEE Transactions on Energy Conversion*, vol. 36, no. 3, pp.2287-2296, Sept.2021. doi: 10.1109/TEC.2020.3040265.

- IV. E. Preci *et al.*, "Hairpin Windings: Sensitivity Analysis and Guidelines to Reduce AC Losses," *2021 IEEE Workshop on Electrical Machines Design, Control and Diagnosis (WEMDCD)*, Modena, Italy, pp.8287. doi:10.1109/WEMDCD51469.2021.9425643.

- V. E. Preci *et al.*, "Segmented Hairpin Topology for Reduced Losses at High-Frequency Operations," in *IEEE Transactions on Transportation Electrification*, vol. 8, no. 1, pp. 688-698, March2022. doi: 10.1109/TTE.2021.3103821.

- VI. E. Preci *et al.*, "Modelling of Voltage Distribution within Hairpin Windings," *IECON 2021 – 47th Annual Conference of the IEEE Industrial Electronics Society*, Toronto, ON, Canada, 2021, pp.1-6. doi: 10.1109/IECON48115.2021.9589507

Contents

ACKNOWLEDGEMENT	III
Abstract	IV
Thesis Outline	VI
List of Scientific Publications	VIII
Contents	IX
List of Figures	XII
List of Tables	XVII
Chapter 1.	1
Introduction and literature Review	1
1.1. Electrical Motor Assembly	2
1.2 Random Wound Winding	4
1.3. Common Industrial Winding Types	5
1.3.1. Magnet Wire.....	5
1.3.2. Litz Wire.....	10
Chapter 2	12
Losses in Permanent Magnet Machine	12
2.2. Winding Copper Losses	13
2.3. Copper Losses with Low Frequency Fundamental.....	14
2.3.1. Zero Frequency Resistance	15
2.3.2. Winding Direct Current resistance	15
2.3.3. Mitigation of Direct Current copper loss	16
2.4. High Frequency Copper Loss	17
2.5. Description of the Skin Effect Losses	17
2.6. Description of Proximity effect Losses	20
2.7. Description of the Circulating Current Loss.....	22
2.8. First Finite Element Analysis of the fundamental losses in the winding.....	25
2.8.1. Skin Effect Evaluation via Finite Element	25
2.8.2. Proximity Effect Evaluation via Finite Element	26
2.8.3. Circulating Current Evaluation via Finite Element	27

Chapter 3	29
Traction Machine design for Automotive	29
3.1 Design Specifications and Tool Chain Adopted	30
3.2 Conclusion and Technical Considerations	33
Chapter 4	35
Analysis on Random Winding	35
4.1. Methods Adopted for AC Losses Evaluation	38
4.1.1. Analytical Method.....	39
3.1.2. Finite Element Model.....	42
4.1.3. Results.....	45
4.2. Proposed Method for Losses Evaluation.....	48
4.2.1. Theory of Statistics.....	48
4.2.2. Description of the Experimental Statistical Method (ESM)	50
4.3. Case Study	50
4.4. Experimental Characterization	52
4.4.1. Experimental Rig Setup	52
4.4.2. Iron loss estimation via Finite Element	54
4.5. Experimental Validation of the ESM	55
4.5.1.Motorette fed with Pure Sinusoidal Current	55
4.5.2.Motorette fed with Inverter	58
4.6. Conclusion	60
Chapter 5	62
Strategies to Reduce AC Losses Hairpin Winding	62
5.1. Models to predict high frequency copper losses.....	63
5.1.1. Domain definition.....	63
5.1.2. Model Definition.....	64
5.1.3. Theoretical Case studies.....	66
5.1.4. Analytical vs FE Results	68
5.2. Number of layer influence to the total AC losses	70
5.3. Fill factor influence to the total AC losses.....	73
5.4.Conclusion	76
Chapter 6	78
Proposed Hairpin Topology to Improve Performance at High Frequency	78
6.1. Introduction to the Proposed Concept	79
6.1.1. Manufacturing aspect of the Hairpin Topology.....	82
6.2. Analytical Calculation.....	83

6.2.1. End Winding Region Model Simplification	84
6.3. Finite Element Model.....	85
6.3.1. Slot Region Model	85
6.3.2. Hypothesis for the End Winding Region Model	85
6.4. Comparison between Analytical and FE Results	88
6.4.1. Slot Region Model: Analytical vs FE results	88
6.4.2. Complete Analytical Model vs. Complete FE Model	90
6.6. Experimental Validation of the Proposed Concept	91
6.7. Experimental Comparison Between Hairpin and Random	95
6.8. Conclusion	96
Chapter 7 Modelling of Voltage Distribution within rectangular wire	98
7.1 Background	98
7.2 Problem description	100
7.3 Modelling approach	101
7.3.1 Principles for modelling	101
7.3.2 Lumped-parameter model	104
7.3.3 Equations for the lumped-parameters model	106
7.3.4 2D Circuital parameters determination	109
7.3.5 Summary	118
7.4 Modelling results	119
7.4.1 Reference systems	119
7.4.2 Simulation results	121
7.4.3 Sensitivity analysis	123
7.5 Experimental Results	126
7.5.1 Test set-up and preliminary investigations	127
7.5.2 No Load Test Results	128
7.5.3 On Load Test Results	134
7.6. Comparison between Numerical model and Experimental Model.....	136
7.7. Conclusion and next steps	137
Conclusions	140
References	143
APPENDIX 1	152
APPENDIX 2	154

List of Figures

Fig. 1.1. Exploded view of PMSM.

Fig. 1.2. Stator lamination and its parts.

Fig. 1.3. Detail of the Slot Model.

Fig. 1.4: (a) Insulated round magnet wire, (b) Insulated square magnet wire, (c) Insulated rectangular magnet wire.

Fig. 1.5. Slot – filling comparison with theoretical positions for round and square magnet wire.

Fig. 1.6. Breakdown Voltage of different grades of magnet wire for varied nominal diameter.

Fig. 1.7. Percentage of total strand area occupied by the insulation coat (Grade 2).

Fig. 1.8. Litz wire.

Fig. 2.1. Isometric view of stator motorette.

Fig. 2.2. Skin effect in a conductor.

Fig. 2.3. Proximity effect.

Fig. 2.4. Finite – element analysis of Skin effect in strand.

Fig. 2.5: Proximity effect in the strands (a) with no supply current in strand 2, (b) with supply current in same direction for both strands, (c) with current in the opposite directions.

Fig. 2.6: (a) Model for investigating circulating current, (b) circuital representation of the connection in model, (c) Flux function and current density in the strands.

Fig. 2.7. Waveforms of the individual current in the strands and the source current.

Fig. 3.1. Tool Chain for Design Optimization.

Fig. 3.2. Permanent Magnet assisted SynRel motor sketch.

Fig. 1.3: Machine performance characteristic: a) speed- torque; b) speed-power.

Fig. 3.4. Traction Machines Overview in Automotive Industry.

Fig. 4.1: Magnetic field path: a) ratio high/width equal to 1.8, b) ratio high/width equal to 3.8, c) ratio high/width equal to 7.2.

Fig. 4.2. Sketch of one slot: discretized domain.

Fig. 4.3. Detailed Model.

Fig. 4.4. Strand Mesh Definition. Fig. 4.5. Finite Element Models: a) q2_VT, b) q2_HZ, c) q4_VT, d) q4_HZ.

Fig. 4.6. Finite Element Models: a) motorette_q4, b) motorette_q2, c) circuit of detailed slot, d) circuit of non detailed slots.

Fig. 4.7. Analytical Vs FEA results: a) Stator with q=2, b) Stator with q=4.

Fig. 4.8. K_{AC} error between analytical method and FE models.

Fig. 4.9. Current density distribution: a) Stator_q4, b) Stator_q2.

Fig. 4.10. Normal Distribution Example with $\mu = 4$ and $\sigma = 1, 0.5, 0.2$.

Fig. 4.11. Case study motorettes: with q=2 (left hand side) and q=4 (right hand side).

Fig. 4.12. Motorette parametric drawing.

Fig. 4.13. Pure sine wave experimental set up and schematic layout.

Fig. 4.14. PWM experimental setup and schematic layout.

Fig. 4.15. Experimental Absolute Frequency of K_{AC} for motorette with q=2 at 1000Hz.

Fig. 4.16. Experimental Absolute Frequency of KAC for motorette with q=4 at 1000Hz.

Fig. 4.17. Current waveforms for different switching frequencies: 10kHz, 20kHz, 40kHz.

Fig. 4.18. Experimental KAC obtained with pure sine and PWM for q=2.

Fig. 4.19. Experimental KAC obtained with pure sine and PWM for q=4.

Fig. 5.1. Discretized domain.

Fig. 5.2. Stator angular sectors built and analyzed in the FE models for a) q=4; b) q=3; c) q=2.

Fig. 5.3. Comparison between analytical and FE models used to evaluate the Stator Angular Sector AC losses: a) q=4; b) q=3; c) q=2.

Fig. 5.4. Current density (A/m) distribution for stators with q=2, k=8 and k=2 at a) 100 Hz and b) 3 kHz.

Fig. 5.5: a) Current density distribution in normal direction across the red line from the bottom until the top of the slot ; b) Current density distribution in the three directions.

Fig. 5.6. Stator with $q=4$ and $k=4$ with different slot fill factors: a) 1; b) 0.90; c) 0.8; d) 0.7; e) 0.6; f) 0.5.

Fig. 5.7. Stator with $q=4$ and $k=2$ (originally with $k=4$ and 2 conductors closest to the slot opening zone removed).

Fig. 5.8. AC losses for the case study with $q=4$ and $k=4$, with variable slot fill factors.

Fig. 5.9. Percentage loss reduction with respect to the case with fill factor equal to 1.

Fig. 5.10. Percentage loss reduction achieved by removing the closest conductors to the slot opening.

Fig. 6.1. Permanent Magnet assisted SynRel motor sketch.

Fig. 6.2: a) the proposed segmented hairpin concept and b) circuital schematic; c) conventional hairpin circuital schematic

Fig. 6.3. FE slot region model for the case study with $q=2$ and $k=4$.

Fig. 6.4. End Winding Region Models: a) Axially-extruded conductor (2D analysis) and b) Angularly-extruded conductor (3D analysis).

Fig. 6.5. End winding region model: a) $q=2$ and $k=4$; b) $q=4$ and $k=4$; c) $q=4$ and $k=4$ segmented; d) $q=4$ and $k=8$.

Fig. 6.6. Slot region models: analytical vs. FE results -a) $q=2$, $k=4$ and $q=4$, $k=8$; b) $q=4$, $k=4$ and $q=4$, $k=4$ segmented.

Fig. 6.7. Comparison between results obtained with the slot region model and complete model for $q=2$, $k=4$.

Fig. 6.8. Complete analytical model vs. complete FE model: comparison of results relative to the investigated conventional arrangements.

Fig. 6.9. Built motorettes.

Fig. 6.10. Experimental layout: a) Experimental setup and b) corresponding circuital schematic.

Fig. 6.11. Comparison between FE and experimental results: a) $q=2$, $k=4$ and $q=4$, $k=8$; b) $q=4$, $k=4$ and $q=4$, $k=4$ segmented.

Fig. 6.12. Experimental results: random vs. hairpin windings.

Fig. 7.2. Full representation of a machine coil and its subdivision.

Fig. 7.2. Cross section of a machine slot, with active sides and relevant circuital parameters highlighted.

Fig. 7.3. Equivalent lumped-parameter circuit.

Fig. 7.4. Model implementation in Matlab Simulink.

Fig. 7.5. Creation of the slot geometry and materials assignment.

Fig. 7.6. Dynamic view of the slot model.

Fig. 7.7. Solution mesh of the FE model in ElecNet.

Fig. 7.8. Solution mesh of the FE model in MagNet.

Fig. 7.9. Two case studies showing the model flexibility in terms of geometrical dimensions.

Fig. 7.10. Qualitative illustration of the automated procedure.

Fig. 7.11: sketch of the reference system slots: a) slot with $q=4$ and winding with 4 layers ; b) slot with $q=4$ and winding with 8 layers ; c) slot with $q=2$ and winding with 4 layers.

Fig. 7.12. Input voltage waveform from the converter output at $f_{PWM}=10\text{kHz}$, $V_{DC}=400\text{V}$, $dv/dt=20\text{Kv}/\mu\text{s}$ and $k_{DC}=0.5$.

Fig. 7.13: comparison between input voltages at two different dv/dt and V_{DC} , i.e. 1) $dv/dt=3\text{ kV}/\mu\text{s}$ & $V_{DC}=800\text{ V}$ and 2) $dv/dt=20\text{ kV}/\mu\text{s}$ & $V_{DC}=400\text{ V}$.

Fig. 7.14: Kind of winding considered: a) TYPE A; b) TYPE B.

Fig. 7.15: $v_{1,12}$ vs. dv/dt and V_{DC} for TYPE A : a) q_2 4layer ; b) q_2 4layer ; c) q_4 8layer.

Fig. 7.16: $v_{1,12}$ vs. dv/dt and V_{DC} for TYPE B : a) q_2 4layer ; b) q_2 4layer ; c) q_4 8layer.

Fig. 7.17. Built motorette.

Fig. 7.18. Experimental set-up.

Fig. 7.19. No Load Test schematic.

Fig. 7.20: oscilloscope capture for node voltages with motorette $q_2_4\text{Layer}$ at $k_{DC}=0.5$, with $f_{PWM}=30\text{kHz}$, $V_{DC}=200\text{ V}$: a) rise time = 8 ns ; b) rise time 17 ns.

Fig. 7.21: oscilloscope capture for node voltages with motorette $q_2_4\text{Layer}$ at $k_{DC}=0.5$, with $f_{PWM}=30\text{kHz}$: a) $V_{DC}=200\text{ V}$; b) $V_{DC}=275\text{ V}$; $V_{DC}=350\text{ V}$.

Fig. 7.22: oscilloscope capture for node voltages with motorette q4_4Layer at $k_{DC}=0.5$, with $f_{PWM}=30\text{kHz}$: a) $V_{DC}=200\text{ V}$; b) $V_{DC}=275\text{ V}$; $V_{DC}=350\text{ V}$.

Fig. 7.23: oscilloscope capture for node voltages with motorette q4_8Layer at $k_{DC}=0.5$, with $f_{PWM}=30\text{kHz}$: a) $V_{DC}=200\text{ V}$; b) $V_{DC}=275\text{ V}$; $V_{DC}=350\text{ V}$.

Fig. 7.24. On Load Test schematic.

Figure 7.25: Experimental acquisition of the voltage distribution: a) Q2_4layer; b) Q4_4layer; c) Q8_4layer.

Fig. 7.26. Turn has active sides in first and second layers.

Fig. 7.28. Comparison between numerical and experimental results (q2_4layers).

Fig.A1.1. Parallel strand positions.

Fig. A2.1. Motorette cross section with $q=2$ and $K=4$.

Fig. A2.2. Hairpin wiring diagram connection with $q=2$ and $K=4$.

Fig. A2.3. Motorette cross section with $q=4$ and $K=4$.

Fig. A2.4. Hairpin wiring diagram connection and electrical scheme, with $q=4$ and $K=4$.

Fig. A2.5. Motorette cross section with $q=4$ and $K=4$ segmented.

Fig. A2.6. Hairpin wiring diagram connection with $q=4$ and $K=4$ segmented.

Fig. A2.7. Electrical scheme of the wiring connections with $q=4$ and $K=4$ segmented.

Fig. A2.8. Motorette cross section with $q=4$ and $K=8$.

Fig. A2.9. Hairpin wiring diagram connection with $q=4$ and $K=8$.

Fig. A2.10. Electrical scheme of the wiring connections with $q=4$ and $K=8$.

List of Tables

TABLE 1.1. TEMPERATURE CLASS OF MAGNET WIRE.

TABLE 1.2. TEMPERATURE CLASS AND INSULATION MATERIAL.

TABLE 3.1. MOTOR GEOMETRICAL PARAMETERS.

TABLE 4.1. MOTORETTE GEOMETRICAL PARAMETERS.

TABLE 4.2. WINDING DETAILS.

TABLE 4.3. MATERIAL COEFFICIENT FOR 0.35 MM SILICON IRON LAMINATION (20C).

TABLE 4.4. μ AND σ VALUE OF K_{ac} PROBABILITY DISTRIBUTION.

TABLE 4.5. INCREASING OF LOSSES COMPARED WITH PURE SINE Q2.

TABLE 4.6. INCREASING OF LOSSES COMPARED WITH PURE SINE Q4.

TABLE 5.1. SLOT AND CONDUCTOR GEOMETRICAL PARAMETERS.

TABLE 5.2. BEST WINDING SOLUTION FOR STATOR WITH Q=4.

TABLE 5.3. BEST WINDING SOLUTION FOR STATOR WITH Q=3.

TABLE 5.4. BEST WINDING SOLUTION FOR STATOR WITH Q=2.

TABLE 5.5. RELATION BETWEEN SKIN DEPTH AND CONDUCTOR SIZE.

TABLE 6.1. MOTOR GEOMETRICAL PARAMETERS.

TABLE 6.2. MOTORETTE GEOMETRICAL PARAMETERS.

TABLE 6.3. BAR CROSS SECTION PARAMETERS.

TABLE 6.4. COMPARISON AC LOSSES AT 1KHZ BETWEEN 2D AND 3D END WINDING MODELS.

TABLE 6.5. CONDUCTOR END WINDING SIDE LENGTH.

TABLE 7.1. PRODUCTS AND SPECIFICATIONS OF THE SLOT ITEMS.

TABLE 7.2. HAIRPIN DIMENSIONS.

TABLE A1. MAGNITUDE AND PHASE VALUES OF THE CURRENT THROUGH THE PARALLEL STRANDS.

Chapter 1.

Introduction and literature Review

Increasing prosperity in developing economies has caused the demand for transportation to increase. Global demand for both passenger and freight transport services is forecasted to be more than double by 2040 which is consistent across road, aviation and marine [1]. Despite increase in use of alternative fuels, particularly natural gas and electricity, the transport sector is still dominated by oil. The projections in Evolving Transition (ET) scenario [1], oil demands accounts for around 85 percent of total transport fuel demand in 2040 while the natural gas, electricity and combination of 'other' types of fuels such as biofuels and hydrogen are projected to account for approximately 5 percent of transport fuel. As such, the main challenges faced worldwide are (i) increased emissions, including the ones by greenhouse gases, (ii) increased energy demand versus limited non – renewable energy sources and rising prices. To tackle the challenges of emissions, most governments around the world are introducing stringent emissions standards. For example (e.g.), the Euro 6/VI vehicle emission standards. 90 percent of global vehicle sales are in the G – 20 countries, out of which 17 members follow the European regulatory pathway for vehicle emissions control [2]. Car manufacturers have chosen to satisfy these emission standards by making efficiency improvements and investing into research and innovation on the propulsion systems. To counter the challenges of limited non – renewable resources and to achieve a sustainable transportation, national and international policy makers have been promoting greener vehicles in the recent decade. The Electric Vehicles Initiative (EVI) and EV30@30 campaign are such forums dedicated to accelerating the deployment of electric vehicles worldwide [3]. EVs such as Plug – in Hybrids Electric Vehicles (PHEVs) and Battery Electric Vehicles (BEVs) for road transport boost energy efficiency by using high efficiency electric – drive systems and contribute to a wide range of transport goals such as enhanced energy security, better air quality, less noise and reduced greenhouse

gas emissions (in conjunction with low – carbon power generation mix). Rotating electrical machine is one of the main components in an EV. The permanent magnet synchronous machine (PMSM) has stand out as one of the suitable candidates for traction requirements due to combination of several advantages such as high efficiency, high power factor, high torque density, high overload capability, robustness, reduced maintenance, compactness and low weight. Apart from that, the absence of rotor copper loss allows for increase in the efficiency while high energy PM excitation allows for reduced overall volume or weight. Flux – weakening capability of the PM machine allows for operating in wider range of speed. However, the PM excitation has certain drawbacks, such as risk of demagnetisation at high temperature and relatively higher cost of rare – earth permanent magnets [4].

1.1. Electrical Motor Assembly

The PMSM is realized by assembling different elements with different physics and functions. Their combination is of paramount importance to satisfy the requirement of electromagnetic, mechanical and thermal constrains. An exploded view of a classical machine for automotive applications is shown in Fig.1.1, where the key components are highlighted.

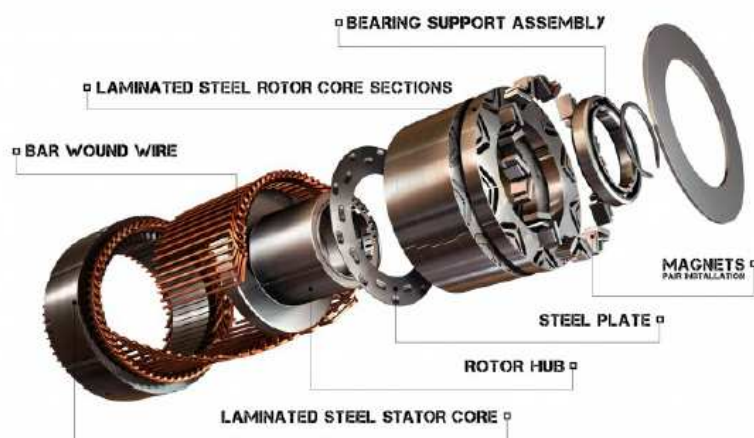


Fig.1.1. Exploded view of PMSM [5].

The parts playing a crucial role for the electromagnetic aspects are the laminated stator core, the armature winding, the laminated rotor core and the rotor magnets. The bearing support assembly, the steel plate, the rotor hub and the housing constitute the mechanical components of the machine (also called passive components). The housing provides support for the stator core and protect the machine parts from foreign objects such as water, dust, sand, and moisture. In addition, cooling system elements are embedded to improve the machine's performance, have a better extraction of the losses generated and improve the system thermal limits, which represents one of the main constraints to achieve higher power density. This motor topology needs active cooling to satisfy the power delivery requirements. Active cooling techniques require the use external devices such as fans, blowers, and pumps to force coolant (air or liquid) flowing through cooling channels either inside or outside, or both, of the motor [6].

The stator typically is the outer part of the electromagnetics components. It is made up of a stack of laminated steel with the inner region is usually presenting slots or grooves, where the stator windings are positioned. The sections adjacent to these slots are the teeth and the area that is radially outwards from the slots connecting the teeth is the stator yoke (also called back iron). The teeth and the yoke together form the stator core of the machine. The windings, the stator core and the insulation system used to physically separate the two, form the main stator components. The winding and the core form the active part of the stator, creating a rotating magnetic field and guiding the magnetic flux, respectively. The insulation is the passive component of the core. Fig. 1.2. shows the sketch of a stator core lamination with its various sections.

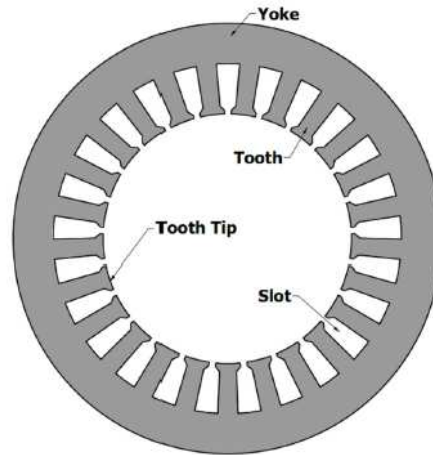


Fig. 1.2. Stator lamination and its parts.

1.2 Random Wound Winding

This kind of winding is normally used for machine with power rating ranging from very small power up to several hundreds of kilowatts, with at voltage levels typically less than 1000 V. This ranges are typically requested by automotive applications.

The components in the slot of a random – wound stator are the copper conductors, the slot liners, the wedge and the impregnation material. Fig.1.3. shows the cross section of a trapezoidal shaped slot in a random – wound stator.

The wedge at the top of the slot has the function to hold the conductors inside the slot. The round insulated cooper conductors (magnet wires) are continuously wound (usually by hand or in a former using a winding machine) through the slots in the stator core to form a coil. The slot liner provides ground insulation between the current carrying copper coils and the grounded stator slot. One of the insulation paper mostly used in this market is called Nomex, it is resistant to chemical attack and has a thermal classification of 220 C. The paper thickness varies from 0.1 mm to 0.5 mm depending on the voltage class of the machine. In random – wound stator, after the coils are inserted into the slots, the stator core is coated with a varnish or resin. This impregnating coat imparts resistance to moisture and contamination and improves the electrical breakdown strength of the windings. The impregnation is usually done with epoxy resin and is used to improves the

transmission of heat from the windings to the stator core. In addition, this impregnating material holds the conductors tight in the slot and reduces the tendency to move/vibrate under the magnetic forces [7]. More importantly, the resin is also used to fill the airgaps between conductors, as well as between slot walls, slot liner and main conductors. Any air pocket is subject to electric fields created by the different potential of the conducting parts and ferromagnetic core, and therefore at risk of partial discharges when the voltage levels are higher than the inception voltage, with consequent degradation of the insulation system.

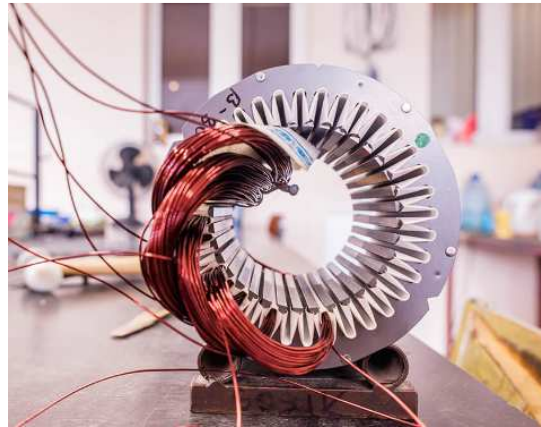


Fig. 1.3. Detail of the Slot Model [8].

1.3. Common Industrial Winding Types

1.3.1. Magnet Wire

The most common types and widely used electrical conductors for fabricating stator windings in small and medium sized electric motors is magnet wire. Magnet wire consists of a base metal (usually copper or aluminium) wire coated with a thin one – or multilayer of insulation materials such as enamel, fibrous polyester, fibreglass yarn, and polyamide. The insulation materials on the magnet wire allow winding wires to contact each other without forming electrical short circuits between them. The selection of the magnet wire is based on the motor operation conditions (working frequency, current, voltage, temperature, etc.), wire material properties, wire diameter for allowing maximum current density, thermal class, coating material, thickness of coating layer, and others.

The following are the most important features of magnet wire:

- a) Small and uniform insulation thickness
- b) Good electrical characteristics such as dielectric strength and insulation resistance
- c) Tough coating, resistant to external forces such as bending, stretching and friction
- d) Heat – resistance
- e) Resistant to solvents, chemical and varnishes
- f) Resistant to hydrolytic degradation
- g) Stable when combined with insulating material
- h) Resistant to water and moisture
- i) Easy to use

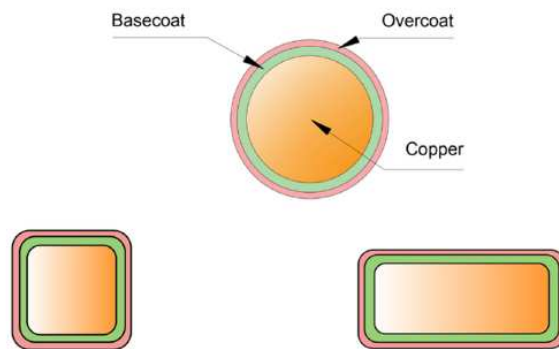


Fig. 1.4: (a) Insulated round magnet wire, (b) Insulated square magnet wire, (c) Insulated rectangular magnet wire.

Fig. 1.4. shows several cross – sectional shapes of magnet wires available for stator windings. The most common magnet wire for random – wound stators in use today is a round copper wire insulated with a polyamide – imide insulation (Class 200°C) or polyester with a polyamide – imide overcoat. The insulation thickness varies from 0.05 mm to 0.1 mm. Apart from the regular magnet wire, in some magnet wires, there is an additional adhesive enamel overcoat that which has a bonding feature. When the adhesive is activated by heat or solvent, the bond coating cements the winding turn – to – turn to create a compact self – supporting coil. NEMA MW 1000, JIS C – 3202, and IEC – 60317 – 0 – 01 are commonly used standards for magnet wires.

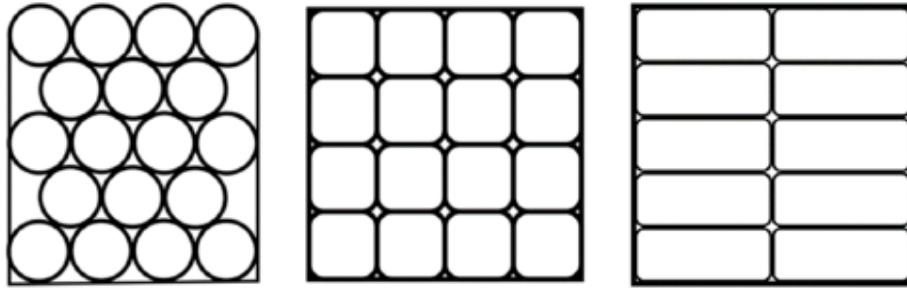


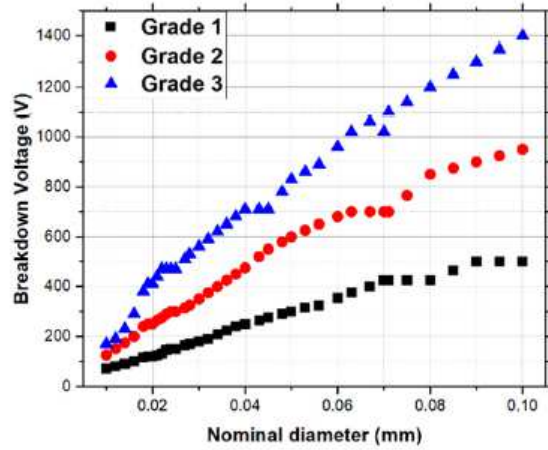
Fig. 1.5. Slot – filling comparison with theoretical positions for round and square magnet wire.

The use of square or rectangular wires can significantly increase the slot – filling factor as shown in Fig. 1.5, which shows the theoretical conductors positions to obtain the maximum slot fill factor. One such example is hairpin winding. Apart from higher slot fill factor, it offers the advantages such as shorter end turns, easy cooling and easier and fully automatic manufacturing [9]. However, when these bar conductors are used in high frequency applications, the bulky conductors induce additional losses due to skin effect, which causes the current to flow only through the outer surface of the conductors.

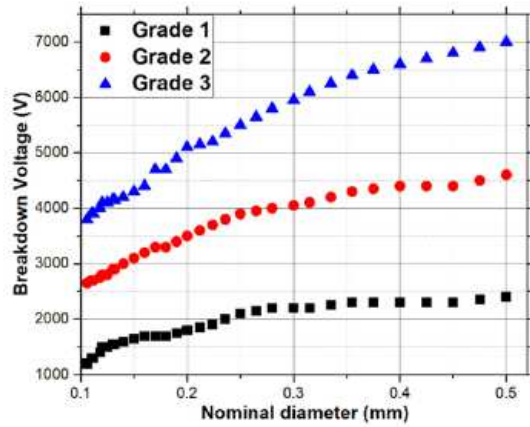
A. Classification of Magnet wire

Magnet wire is classified based on diameter (American Wire Gauge (AWG) number, British Standard Wire Gauge (SWG) or millimetres) or area (square millimetres), insulation class, and temperature class. Based on the breakdown voltage level, which affects the thickness of the insulation overcoat on the magnet wire, it is classified as Grade 1, Grade 2 and Grade 3, with Grade 1 having the weakest endurance level of breakdown voltage. The higher the grades, the thicker the insulation and thus higher the breakdown voltages.

Fig 1.6 shows the Breakdown Voltage (BDV) of different grades of the magnet wire and varied nominal diameter (according to IEC 60 317 [7]).



a) BDV for nom. dia. 0.01 to 0.1 mm.



b) BDV for nom. dia. 0.106 to 0.5 mm.

Fig. 1.6: Breakdown Voltage of different grades of magnet wire for varied nominal diameter.

Based on thermal endurance capacity, magnet wire is classified as [9], [10]:

TABLE 1.1. TEMPERATURE CLASS OF MAGNET WIRE.

CLASS	TEMPERATURE (°C)
O	90
A	105
E	120(IEC)
B	130
F	155
H	180
200(K)	200
220(M)	220
C	240+
250	250(IEC)

Materials used in the temperature classes are listed as follow in Table 1.2.

TABLE 1.2. TEMPERATURE CLASS AND INSULATION MATERIAL.

TEMPERATURE CLASS	INSULATION TYPES
90	Paper
105	Paper, cotton, nylon, polyvinyl acetal, formvar
105 solderable	Polyurethane
130	Epoxy
130 solderable	Polyurethane
155	Polyester, glass
155 solderable	Polyurethane
180	Polyester
180 solderable	Polyester, imide, polyurethane
200	Polyester/amide imide, AI
220	Amide-imide
240	Polyimide

It is worth noting that the thickness of the insulation of magnet wire does not depend on the temperature classes of the magnet wire but depends on the breakdown voltage i.e. if a strand diameter of a specific grade is selected, the insulation thickness will remain the same across all thermal classes of that explicit wire diameter.

B. Insulation versus strand diameter

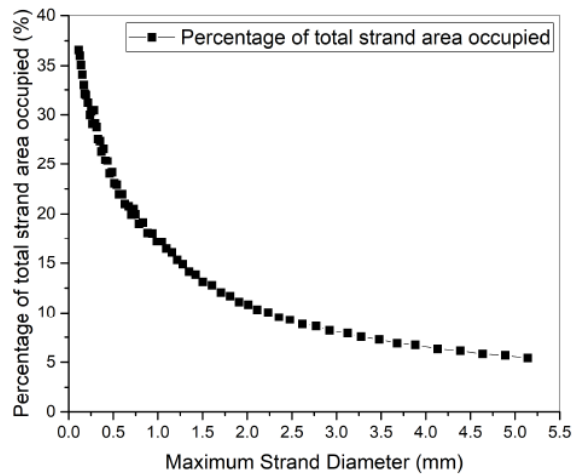


Fig. 1.7. Percentage of total strand area occupied by the insulation coat (Grade 2).

In Fig. 1.7, the abscissas show the total diameter (conductor area + insulation area) of strands and the axis of ordinates shows the percentage of total strand area that is being occupied by the insulation coat on it. With the smallest strand diameter of 0.113 mm, the insulation coat occupied about 36% of the total strand area. The area occupied by insulation decreases exponentially as the strand diameter increases. For largest strand diameter considered in the plot of 5.141 mm, the insulation only occupies approximately 5.4% of the total strand area. Thus, using larger cross – sectional magnet wire, better slot filling factor may be achieved. The data used in the plot is acquired from a standard magnet wire catalogue [11]. Grade 2 magnet wire is used for the aforementioned analysis.

1.3.2. Litz Wire

Litz wire is constructed from thin individual insulated magnet wires woven into a uniform pattern as shown in Fig. 1.8.



Fig. 1.8. Litz wire.

Litz wire is essentially used for high – frequency applications. It utilises the full cross – sectional area of the wire to carry current. Because each individual strand is thinner than the skin depth, the use of Litz wire can greatly minimise the skin and proximity effect losses in high – frequency windings. However, when used in high performance electrical machines operating in demanding environments, Litz wires have some manufacturing and assembling disadvantages such as [6], [12]:

a) Because strands are closely knit, it is difficult to ensure full impregnation of varnish.

- b) Encasing layer of insulation layer is often required to ensure a high degree of inter – coil insulation integrity as the insulation layer on the individual wire strands is very thin.
- c) The manufacturing cost of Litz wire is higher as compared to conventional round magnet wires
- d) Litz winding has a low copper fill factor and poor heat transfer across the winding bundle in comparison to winding former from single conductor turns.

Chapter 2

Losses in Permanent Magnet Machine

Electric motors are electromechanical devices that convert electrical energy to mechanical energy. However, in doing so, not all the electrical energy is converted to useful mechanical energy. This consumed energy is referred to as motor power loss. In motor design, it is important to consider motor power losses and it is desired to understand the mechanisms of various power losses associated with electric motors. The motor efficiency is defined as the ratio of the power output to the power input where power output equals input power minus power loss. Therefore, reduced power losses relate to higher motor efficiency. From economic standpoint, higher power losses are always associated with increased motor costs. A vast majority of power losses in electrical motors are converted into heat energy, which can substantially increase the temperature rise in the windings and deteriorate the performance characteristics of motor. Temperature is a major cause of degradation of insulation materials and accelerates the aging of the winding insulations; thus, reducing their lifetime. High temperature can significantly reduce magnetic properties of permanent magnets (PMs) to lower the performance of PMSM and may lead to risk of the permanent magnets to demagnetise permanently. The high temperature caused by the motor power loss adversely effects the bearing of the machines as well. To keep the machine temperature below the maximum allowed value, all the heat energy produced because of motor loss needs to be dissipated to the surrounding. Thus, selection of cooling method of machine is strongly affected by the power loss in the machine.

The power losses in PM machine can be categorised as no – load and load losses. As the name suggests, no – load losses do not require load torques. The major no – load losses include (a) core losses (also called magnetic losses), caused by the alternating magnetic flux in the stator and rotor cores, magnets and other machine components, (b) frictional and windage losses together grouped as mechanical losses. The load losses include (i)

resistive losses in the stator windings, (ii) stray losses that consists of various kinds of losses that cannot be accounted for.

2.2. Winding Copper Losses

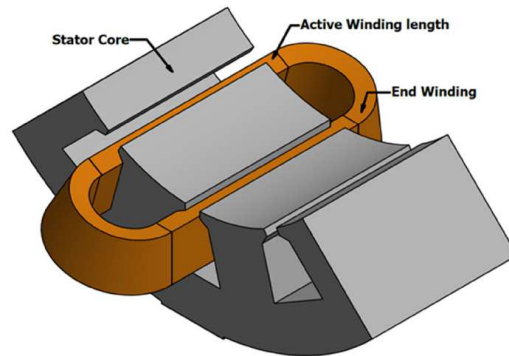


Fig. 2.1. Isometric view of stator motorette.

Fig. 2.1. shows an isometric view of a stator motorette with a single layer concentric winding on the teeth. The winding can be divided into two parts: the active winding length contained within the stator stack, responsible for creating the principal flux needed to produce torque. The principal flux is referred to the flux line which pass from the stator to the rotor and vice versa and their path interests three different zones: rotor, air gap and stator. The overhang area (or the commonly named end - winding), the only function is to form close loops of the coils.

Apart from these parts, in case of the three - phase machines, there may be lead wires connecting the terminals of the machine with the three - phase winding. Since, very few leakage fluxes interact with the lead wires and the end - winding region, the losses in these parts can be considered mainly due to the low frequency fundamental component of copper loss.

However, the part of the winding laying inside the slot are subjected to varying flux linkage. This result in apparent increase in the resistance of the winding due the AC effects, namely, skin and proximity effect and circulating current described in detail in later sections.

2.3. Copper Losses with Low Frequency Fundamental

When low frequency current or also called direct current when the frequency is zero, passes through a conductor (or copper coil), heat is generated in the conductor. This heating is known as ohmic/resistive heating or DC copper loss.

The power of heating generated by an electrical conductor (Joule's first law) is given as the product of the resistance of the material (copper conductor) and the square of the current.

$$P_{DC} = I^2 R_{DC} \quad (2.1)$$

where

P_{DC} is the power loss;

I is the direct current flowing through the conductor;

R_{DC} is the resistance of the conductor.

The ohmic loss in a conductor can also be given as [13]:

$$P_{ohmic} = \int_v \rho J J dv \quad (2.2)$$

Where

V is the volume of the conductor;

ρ is the resistivity of the conductor material;

J is the current density in the conductor.

2.3.1. Zero Frequency Resistance

The electrical resistance, R_{DC} , of a material is proportional to the resistivity of the material ρ (in $\Omega\text{-m}$) and the material length l (in m) and inversely proportional to the cross-sectional area of the material A (in m^2), that is

$$R_{DC} = \frac{\rho L}{A} \quad (2.3)$$

where ρ is a function of temperature T ,

$$\rho(T) = \rho_0(T_0) [1 + \alpha_0 (T - T_0)] \quad (2.4)$$

where

α_0 is the temperature coefficient of resistance of the material

T_0 is the reference temperature

2.3.2. Winding Direct Current resistance

The resistance of a coil is given as

$$R_{coil} = T_c \frac{\rho L_{av}}{n A_{strand}} \quad (2.5)$$

Where

T_c is number of turns in a coil

ρ is resistivity of the material in the coil

L_{av} is the average length of a coil turn

n is the number of parallel strands/ strands – in - hand

A_{strand} is the copper area of one strand

$$A_{strand} = \pi r_{strand}^2 \quad (2.6)$$

Where

r_{strand} is the copper radius of one strand

The phase resistance is given as

$$R_{ph} = \frac{N_c}{a^2} R_{coil} \quad (2.7)$$

Where

N_c is number of coils per phase

a is number of parallel paths

The number of turns in series per phase is

$$T = N_c \frac{T_c}{a} \quad (2.8)$$

Therefore, phase resistance can be given as

$$R_{ph} = \frac{T_{ph}}{a} \frac{\rho L_{av}}{n A_{strand}} \quad (2.9)$$

The average length, L_{av} , of a coil turn in a slot of low – voltage machine with round enamelled magnet wires is given approximately as [14],

$$L_{av} = 2l + 2.3 \tau_p \quad (2.10)$$

Where, l , is length of stator stack of the machine and

$$\tau_p = \pi \frac{\text{stator ID}}{p} \quad (2.11)$$

2.3.3. Mitigation of Direct Current copper loss

Copper filling factor in a slot is defined as:

$$\text{copper fill factor} = \frac{\text{Total copper area per slot}}{\text{Slot area}}$$

One general way of reducing DC copper loss is to aim for achieving high copper filling factor. Resistance of a material is inversely proportional to the area of the material; increasing the copper area in the slot reduces the resistance. Since DC copper loss is

proportional to resistance of the copper conductor, therefore increase in copper area results in reduction in DC copper loss. However, this increases the motor weight and cannot solve the conflict between efficiency and power density, especially in case of electric and hybrid vehicles where weight and space are premium [15]. Using rectangular conductors, representing big cross – sectional areas in the slots of electrical machines provides an opportunity to reduce DC losses.

2.4. High Frequency Copper Loss

Recent development and demand in electric and hybrid vehicles have created a trend of high - speed electrical machines. Increasing the rotational speed of PM machines increases the power density of the machines [16]. Higher power density reduces the volume and weight of the electric motor, and offers great potentials to reduce costs [15], [17]. High – speed machines often have few series turns because of high rate of change of flux linkage so they can have many parallel turns or strands – in – hand [18]. With trend for high – speeds and therefore high electrical frequencies, consideration of the AC effects such as skin and proximity effects, and circulating currents in the ‘strands – in – hand’ is getting more and more important.

In later sections, each of these AC effects are discussed in details and a literature review of the work carried out so far in analysis, modelling and mitigation of these losses is presented.

2.5. Description of the Skin Effect Losses

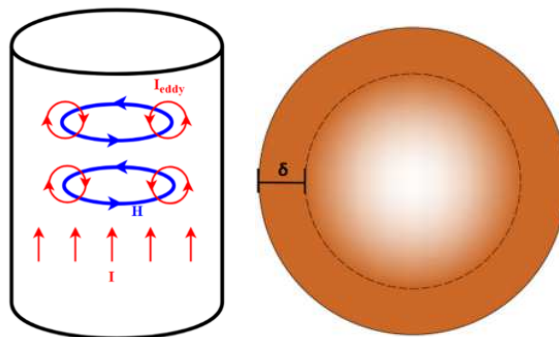


Fig. 2.2. Skin effect in a conductor.

Skin effect is the tendency of the AC current to flow towards the outer periphery/surface of the conductor if it is considered place in air without any other current sources close to it. The skin effect is due to opposing eddy currents induced by the changing magnetic field resulting from the alternating current. As shown in Fig. 2.2, an AC current, I , flowing through a conductor produces magnetic field, H , which in turn creates circulating current eddys inside the conductor. These eddys cancel the current flow in the centre of the conductor and reinforce the current flow towards the outer skin of the conductor, resulting in the current to distribute more towards the outer surface, as shown in Fig. 2.2. Thus, the effective resistance of the conductor increases.

The skin depth is defined as the distance from the conductor surface where the current density decreases exponentially to 36.8 percent as compared to current density at the surface of the conductor ($e = 2.71828$) [19], [20]. The skin depth (δ), can be calculated as [21],

$$\delta = \sqrt{\frac{\rho}{\pi f \mu_0 \mu_r}} \quad (2.12)$$

Where, ρ and $r \mu$ are the electrical resistivity and the relative permeability of the conductor respectively.

The effective resistance of the conductor increases due to skin effect and the factor by which the DC resistive losses have to be multiplied to get the AC resistive losses is the resistance factor k_{skin} . It is also the ratio of the AC and DC resistances of the conductor.

The resistance factor in the slot area is [22],

$$k_{skin} = \frac{R_{AC}}{R_{DC}} = \frac{P_{AC}}{P_{DC}} \quad (2.13)$$

The average resistance factor k_{skin} , over the slot can be calculated as [22],

$$k_{skin} = \varphi(\zeta) + \frac{Z_n^2 - 1}{3} \psi(\zeta) \quad (2.14)$$

Where φ and ψ are auxiliary functions specified as

$$\varphi(\zeta) = \zeta \frac{\sinh(2\zeta) + \sin(2\zeta)}{\cosh(2\zeta) - \cos(2\zeta)} \quad (2.15)$$

$$\psi(\zeta) = 2\zeta \frac{\sinh(\zeta) - \sin(\zeta)}{\cosh(\zeta) + \cos(\zeta)} \quad (2.16)$$

and the reduced strand height ζ , can be calculated as

$$\zeta = d_s \frac{\pi}{2} \sqrt{f \mu \sigma \sqrt{\frac{SFcu}{A_s}}} \quad (2.17)$$

Where

d_s is the strand diameter

f is the supply frequency

μ is the permittivity

σ is the electrical conductivity

$SFcu$ is the copper filling factor

A_s is the cross – sectional area of one strand

One way to mitigate the copper losses in electrical machines due to the skin effect, is by selecting the size of the strands properly [20], [23], [24]. For an operating frequency, if the ratio of the round magnet wire is equal to or smaller than the skin depth, the AC resistance tends to be close to the DC resistance. The optimal stranding to minimise the copper losses is defined by k_{skin} [25]. Another technique to reduce the skin effect is to transpose the coil along the slot [12], [18], [26], [27] or use Litz Wire [28] – [30]. However, with Litz wire, since the wire is stranded, the net copper area inside is reduced. Twisting the strands reduces the slot fill factor, increasing the DC resistance and thus the DC losses. Furthermore, twisting the strands adversely effects the thermal performance and the mechanical flexibility of the strands – in – hand [31] – [32].

2.6. Description of Proximity effect Losses

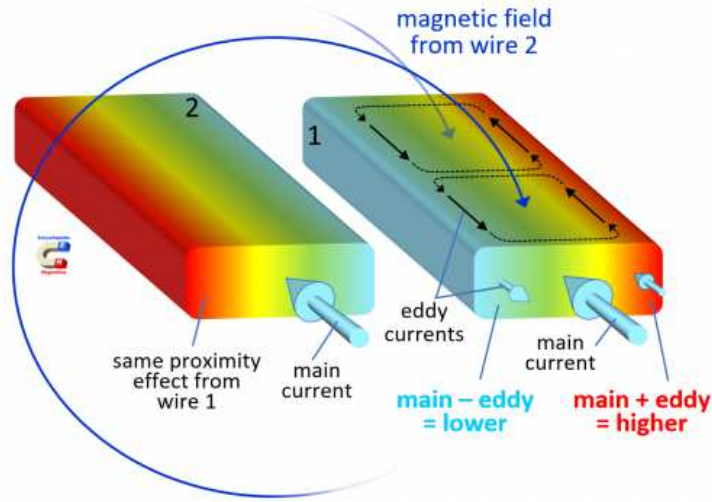


Fig. 2.3. Proximity effect [33].

The proximity effect is the tendency for current to flow in other undesirable patterns that form localised current loops or concentrated distributions due to the presence of a magnetic field generated by nearby conductors [24]. Fig. 2.3 shows the process of proximity effect. The main current, flowing through conductor on left creates a magnetic field, B and according to the Faraday's law, the flux created by this field induced eddy current loops, in the conductor on the right. Thus, if the right conductor is carrying current in the same direction as the left conductor, the eddy loops reinforces the main current in the conductor towards the side closer to the conductor on the left and opposes on the side further away. This creates uneven current distribution inside the conductor increasing the losses in the conductor.

According to [34], [35], the proximity effect losses for all the strands in the slot can be calculated as:

$$P_{proximity} = \frac{\pi \omega^2 l_{eff} d^4 B^2}{128 \rho} \quad (2.18)$$

where

$P_{proximity}$ is the strand – level proximity loss;

ω is the strand – level proximity loss;
 l_{eff} is the effective length of the strand;
 d is the strand diameter;
 B is the flux density amplitude at the strand location in the slot;
 ρ is the conductor resistivity.

Proximity losses in high speed electrical machines is a well – studied and researched area. Klauz in [36] investigated the losses in the windings of a Switched Reluctance Machine (SRM) due to proximity effect using FEA. Authors in [34] presented a 2D analytical model of the stator slots to predict the proximity losses in Surface PM machines including the effects of slot openings. In this paper, the difference between the AC losses in machines with single- and double-layer windings were investigated, and it is shown that the 2D analytical model provide good matches for the predicted flux densities at the AC losses in comparison to the FE results. Reddy [35] presented an integrated analytical tool for estimating the total proximity losses in stator windings for machines operating at high speeds. In [24], authors have noted that high ratios of ac to dc resistance can be exhibited in permanent magnet machines with fractional – slot concentrated windings due to proximity effects at high frequencies despite the adoption of stranded bundles. It is shown in the paper that the proximity effect can be significantly reduced with an appropriate choice of conductor shape, by placing the conductors towards the bottom of the slot and by minimising height in the radial direction of the parallel conductor bundle forming each turn. In [37], authors calculated the winding losses of inductors with rod cores caused by eddy currents in adjacent windings. The paper shows that the proximity losses in a turn depend on both the position of the turn in the winding and the geometry of the whole winding layout and proposed a winding geometry to reduce losses. Authors in [38] presented an investigation into proximity losses in the end – winding region of an ac power inductor using 3D FEA. They conclude that simpler 2D approach tends to overpredict the R_{ac}/R_{dc} ratio and show that endwinding proximity losses are lower than that generated

in the active length of conductors. Iwasaki [39], investigated the effect of high frequency current ripples induced by PWM on the proximity effect losses and concludes that the skin and proximity losses increase significantly due because of PWM. Authors in [40], developed a hybrid analytical – numerical loss calculation method which is computationally efficient for the deriving ac loss in the winding and provides a reasonable compromise between computational time and accuracy.

2.7. Description of the Circulating Current Loss

Parallel strands for coil turns located in the slot top and slot bottom experience proximity effect since there is different flux linkages between them due to leakage.

Due to the slot flux leakage, each strand sees a different flux linkage and thus have a different inductance. This leads to a difference in the total current of each parallel current, increasing the total resistive losses. The difference between the individual and average strand currents is the circulating currents and result in circulating current losses [41], [42], [33], [43]. The leakage may originate from the excitation field or the armature field. The losses induced by the excitation field primarily effects machines with windings in direct exposure to the field flux, such as slotless machines and these losses induced by the excitation field greatly diminish in the presence of the tooth tip [44].

According to [41], [45], the induced losses inside a strand subjected to an external magnetic field $e H$, can be given as

$$P_{cc} = \rho l H^2 D_s \quad (2.19)$$

With

$$D_s = 2 \pi Re \left\{ \frac{\alpha r I_1(\alpha r)}{I_0(\alpha r)} \right\} \quad (2.20)$$

Where

P_{cc} is power in one strand

ρ is the resistivity

L is the length

H is the peak of the magnetic field

$\alpha = \frac{1+j}{\sqrt{2\rho}} \sqrt{\omega \mu}$ is the inverse of the skin depth

R is the radius of the strand

I_0, I_1 are the Bessel functions

Circulating currents resulting from imbalances in the linked field flux by the strands in the slot cause the source current to be shared unevenly among the parallel strands. To minimise the effects of circulating current, each strand should be placed in various positions inside the slot, so that the impedance of all the strands are similar.

Reddy [31], used 3D FEA to investigate the effects of transposition of magnet wires in stator winding bundles on the copper losses in high – speed machines, that work has shown that straight un-transposed bundles have highest losses while bundles with 360° transpositions over the length of the slots produce the least losses. The authors in [46], proposed an analytical model for circulating current loss and compared stators with Litz and stranded conductors' windings to highlight the effect of circulating current losses. Popescu [42], studied the effect of circulating currents in the parallel rectangular strands using FEA and showed that the ac/dc loss ratio is over 50 for a leading-edge conductor at the top of a slot, at high speeds. Van der Geest [41], investigated several techniques to reduce circulating current in the strands in the slot. This includes increasing the number of parallel strands, partially filling the slot, changing the strand shapes, and decreasing the slot size. His findings with increasing number of parallel strands shows that a high number of parallel strands is unattractive, because small differences in strand placement lead to large loss variations. With partially filling slots, the author showed that it is beneficial to not fill the complete slot and place the strands towards the slot bottom. With varied strand shape, it is shown that maximising the slot fill factor does not result in immediate benefits and neither do changing the slot shape. In [32], the author presented a method based on impedance matrix (from 3D FEA) of the windings to estimate the uneven distribution of current across the strands, it showed that a 360° transposition in the winding over the length of the slot significantly reduces the losses. To reduce

circulating current loss, authors in [33] proposed (a) comparison of designs with different number of parallel paths in the winding, (b) partially filling the slot, leaving the slot top area unfilled, (c), varying the slot winding height and tooth width simultaneously, keeping the slot fill factor constant and plotting it against the resistance ratio. Authors in [47], investigated the influence of circulating currents in parallel wires' placement. In this paper, the authors considered two winding cases for a machine. It is experimentally shown that the bad winding has additional loss of 65% at high speed (11 krpm). Authors in [48] showed that for coils made with solid flat conductors, the circulating current losses can be minimised by transposing a single conductor at about 70% of the coil height (from bottom to the top of the slot) at the end winding. Authors in [49], studied the AC loss distribution in the winding with and without parallel strands and the impact on the insulation lifetime of the winding. The paper argues that although the AC loss is greater with higher parallel strands than with single solid conductor, the localised hotspot in case of solid conductor may lead to relatively faster insulation failure.

Arumugam in [50], investigated the influences of the winding arrangements on frequency – dependent resistances along with other investigation points and showed that by adopting winding arrangement that shares the slot leakage flux, the ac losses in the winding are minimized. Lehtikoinen in [43], proposed two alternative FE formulations, point – strand method and polygon – strand method to calculate circulating currents in thin parallel strands. Based on simulations, the author showed that both methods yield reasonable accuracy results and is computationally efficient compared to brute – force approach where the strands are finely meshed to obtain accurate skin – and proximity – effect losses. In [51], the author proposed a circuit – based model and a computationally efficient FE model to calculate circulating current in random – wound electrical machines. The author also proposed a process to generate random winding based on Monte Carlo analysis.

2.8. First Finite Element Analysis of the fundamental losses in the winding

In this section, the fundamental losses described in the above sections are analysed using finite – element, with commercially available software package, MagNet from Mentor Graphics. The parameters used for the purpose of this analysis are as following:

- 1 mm for the strand diameter;
- 100A for the current amplitude;
- 10 kHz for the frequency.

2.8.1. Skin Effect Evaluation via Finite Element

Fig. 2.4 shows the skin effect on a strand placed in air. The skin depth at the frequency of 10 kHz is 651.955 μm and the diameter of the strand is 1 mm, frequently used in the industry applications. It has been chosen a very high frequency to appreciate the physical phenomena with the conductor size selected. In Fig. 2.4, it can be clearly observed that the current density module in $\frac{A}{m^2}$ towards the periphery of the strand increases.

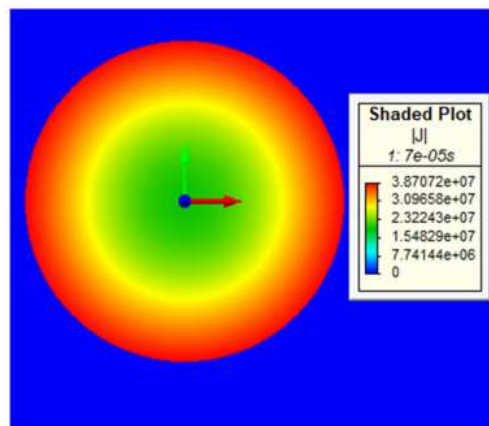
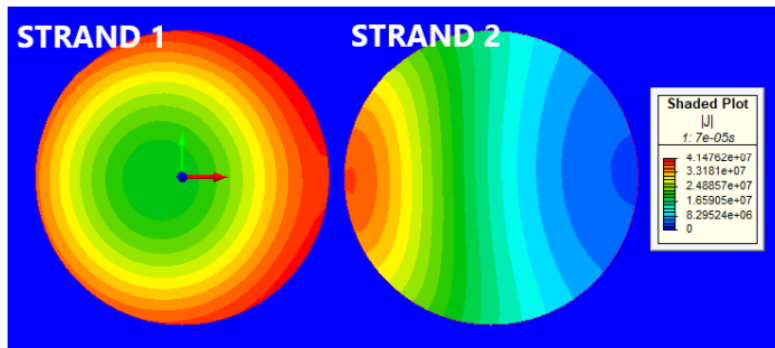
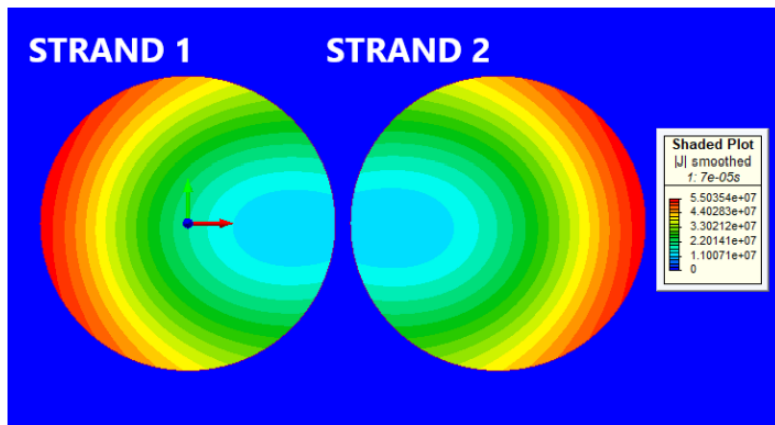


Fig. 2.4. Finite – element analysis of Skin effect in strand.

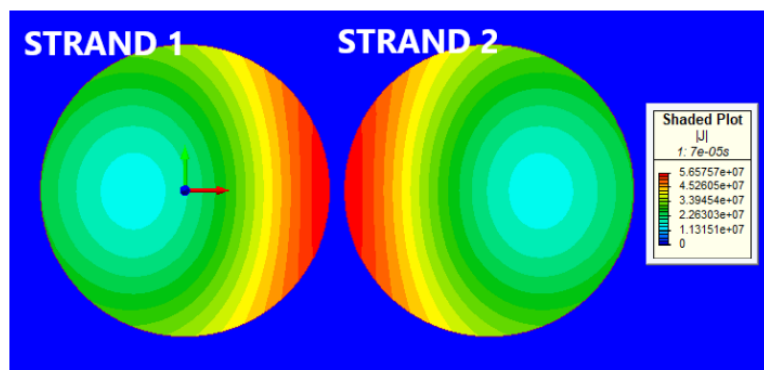
2.8.2. Proximity Effect Evaluation via Finite Element



(a)



(b)



(c)

Fig. 2.5: Proximity effect in the strands (a) with no supply current in strand 2, (b) with supply current in same direction for both strands, (c) with current in the opposite directions.

Fig. 2.5 shows the current density distribution in the strands due to proximity effect. For currents in the strands flowing in the same direction, the regions of higher current density are located towards the far side of each strand. In the case, where the currents in the strands are in opposite directions, the higher current density regions are towards the near side of the strands as shown in Fig. 2.5b and Fig. 2.5c respectively.

2.8.3. Circulating Current Evaluation via Finite Element

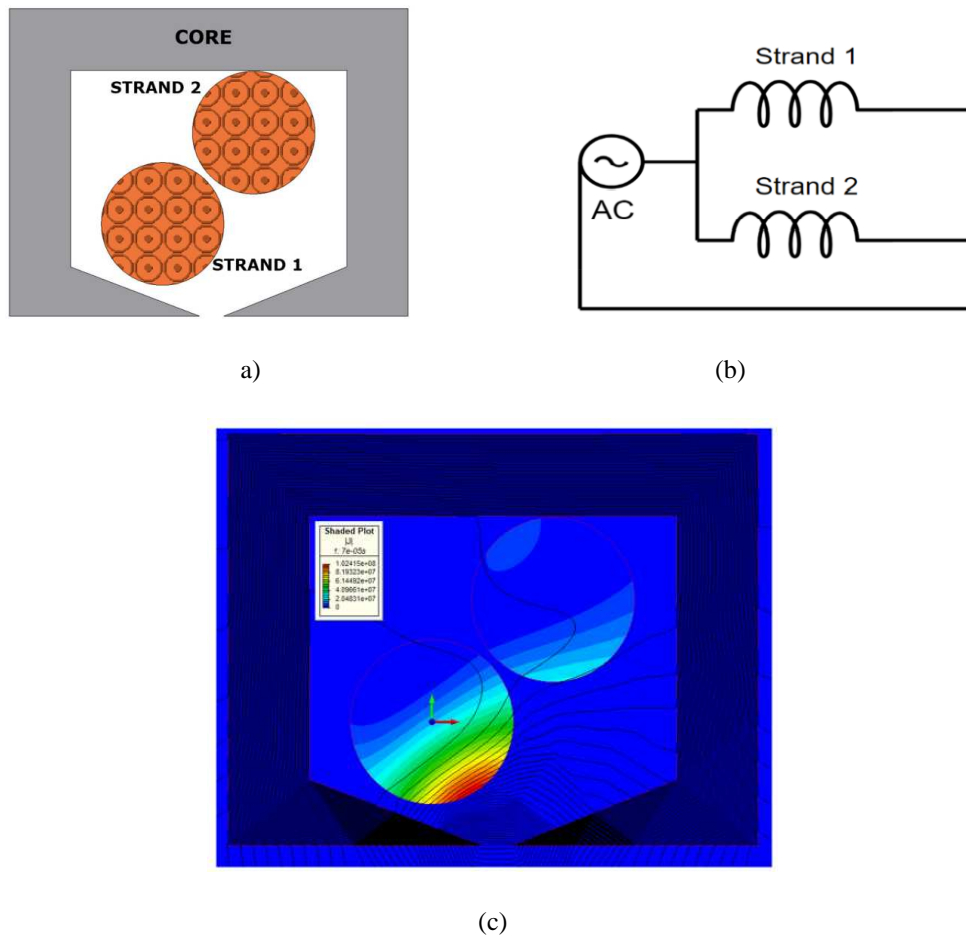


Fig. 2.6: (a) Model for investigating circulating current, (b) circuitual representation of the connection in model, (c) Flux function and current density in the strands.

Fig. 2.6a shows a model of a semi - closed slot core with two strands placed inside it. The strands are connected in parallel and the supply is fed from a current source as shown in Fig. 2.6b. Fig. 2.6c shows the current distribution in the strands at a time instant. The concentration of the slot leakage flux is higher towards the slot top (near the slot opening) than towards the bottom of the slot. The strand (Strand 1) placed near the slot top links with a different flux compared to the strand (Strand 2) placed towards the slot bottom. This causes a difference in the inductance of the parallel strands, the supply current in unevenly shared by them. Fig. 2.7. shows the current in the individual strands. It can be seen that, strand 1 is carrying the bulk of the supply current which may lead to hotspot and premature insulation failure of the strand.

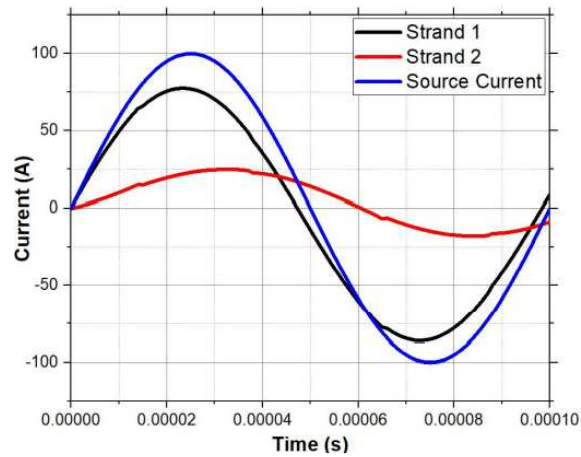


Fig. 2.7. Waveforms of the individual current in the strands and the source current.

Chapter 3

Traction Machine design for Automotive

This chapter provide a description of a design process adopted for an electrical machine suitable to match some of the exigencies required by the automotive market. The outcome of this chapter will be the case reference for the studies in the next chapters of this thesis. It is important to make clear that in this work only the electromagnetic aspects have been considered, keeping out the mechanicals, thermals and manufacturing ones, which they are as much important as the electromagnetic ones to make the e-Motor component suitable to be part of the vehicle architecture.

The automotive application considered for this work leading to multiple machine operating points, making interior PM (IPM) machines better candidates than the surface mounted ones [52]. Indeed, IPM machines are particularly attractive for automotive over the other machine topologies, because of their wide flux-weakening region, high torque density and efficiency [53]. In particular, they are more compact and present lower inverter capabilities, with respect to induction machines (IMs), when a large Constant Power Speed Ratio (CPSR) is required [53] as, theoretically, the maximum speed can be infinite [54]. Being the complexity of the vehicle architecture increasing with the years, for the this applications the volume available for each components is always limited, the trend at design stage is to increase the kW/m³ for the electrical machines.

The mechanical power delivered by the e-Motor is given by the equation :

$$P_{mech} = T_{mech} \omega_{mech} \quad (3.1)$$

Where ω_{mech} is the mechanical speed, T_{mech} is the mechanical torque

$$T_{mech} \propto l_{rotor} R_{rotor,out}^2 B_g A \quad (3.2)$$

l_{rotor} is the rotor length, $R_{rotor,out}^2$ is the rotor outer radius, B_g the airgap flux density and A the current loading.

High power density electric machines can be achieved by minimizing the non-active parts, such as the end winding and increasing the parameters in equations before:

- Increasing the airgap flux density by using a combination of magnets and core material
- higher ω_{mech}
- high current loading or high current density matching the thermal limits

3.1 Design Specifications and Tool Chain Adopted

The target vehicle considered has a total mass and frontal area equal to 2500 kg and 3.2 m², respectively. The peak wheel torque is 3500 Nm with a wheel radius equal to 0.32m. The electrical machine is connected to the wheel through a gearbox with a ratio of 12:1. The peak power for short pulses of 40 s is 160 kW at the base speed (5000 krpm) and a power of 110 kW must be delivered at the maximum speed (19krmp). The inverter driving the electric motor, it is supposed to have the maximum capability of 600V for the DC link and 450Arms for the current.

In this work a tool has been developed, as per Fig. 3.1, to consider the machine preliminary design stage and allows the designer to identify the most promising machines that meet the requirements needed for the application, power density, efficiency and cost in this particular case. Indeed, traditional machine sizing would result being too time consuming and impractical due the big number of permutations involved. Therefore, a design tool that rapidly evaluates optimal electrical machines is required for this kind of analysis. The design tool employs a multi-objective Genetic Algorithm to maximize the efficiency, machine power to volume ratio and minimize the cost.

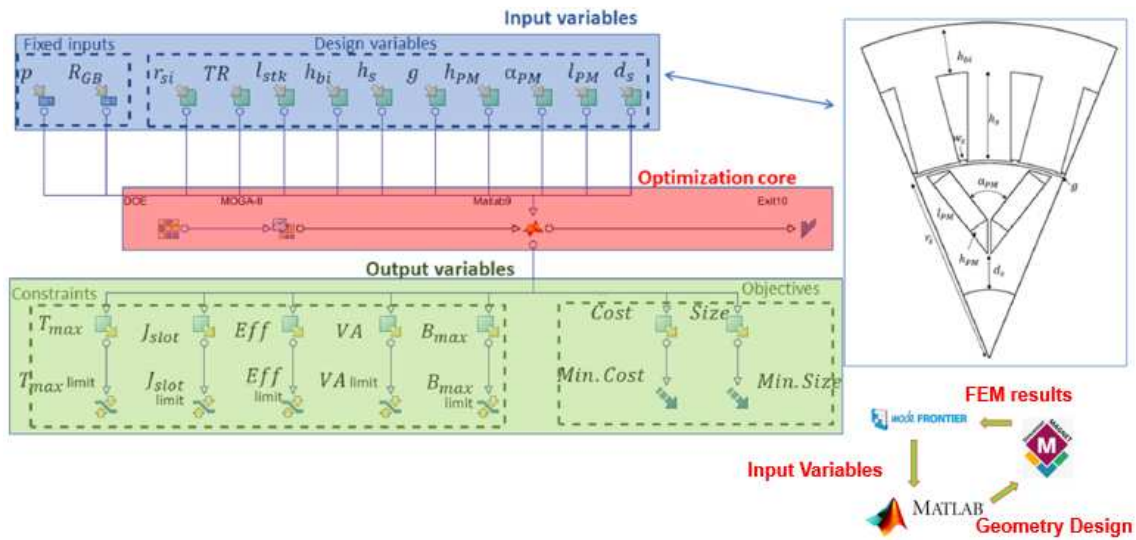


Fig. 3.1. Tool Chain for Design Optimization.

The sizing tool developed is based on a commercial optimization software, modeFrontier [55], where the optimization problem is defined. Fig. 3.2 shows the diagram taken from modeFrontier workspace. The diagram can be divided into three parts: input variables, optimization core and output constraints/objectives. The design variables represent all the machine geometrical parameters considered in the optimization problem. These are the inputs of the Matlab design environment located together with the Design of Experiment (DOE) and MOGA-II blocks in the optimization core. The DOE creates the initial population, based on a pseudo-random sequence defined by the user (typically set to around 300), while in MOGA-II the optimization routine is selected. The Matlab calculator script receives the inputs from modeFrontier and computes the outputs. At first, the cost, efficiency and size of the different machine active parts can be readily obtained knowing the material properties and the geometrical parameters. The cost of the different materials has been calculated assuming a unit cost of 10 \$/kg for the lamination, 15 \$/kg for the winding and 150 \$/kg for the PM. Then, the geometrical parameters are used to draw one machine pole in the FE software MagNet where the boundary conditions are imposed. Indeed, exploiting the geometrical symmetries of the machine only one pole can be considered for the analysis markedly reducing the computation time.

First of all, a preliminary trade-off study has been completed, considering the following machine topologies: interior Permanent Magnet (IPM), Surface Mounted Permanent Magnet (SMPM), Synchronous Reluctance (SynRel) and Permanent Magnet assisted SynRel (PMaSynRel) machines. After the optimization process, the PMaSynRel option with three barriers has been selected as the best candidate among the others in terms of wide flux-weakening capability, high torque density, efficiency and compactness. For each topologies different pole pair and slot per pole per phase has been considered, PMaSynRel motor with 4 poles assure the best performance, in this work two different slots per pole per phase (q) configuration: 2 and 4. The machine geometry is presented in Fig. 3.2 and the main geometrical parameters are reported in Table 3.1. In Fig.3.3 the machine performance in term of torque and mechanical power are reported, the machine has been a bit oversized to have a safety margin when it will be prototyped and to assure the performance requested.

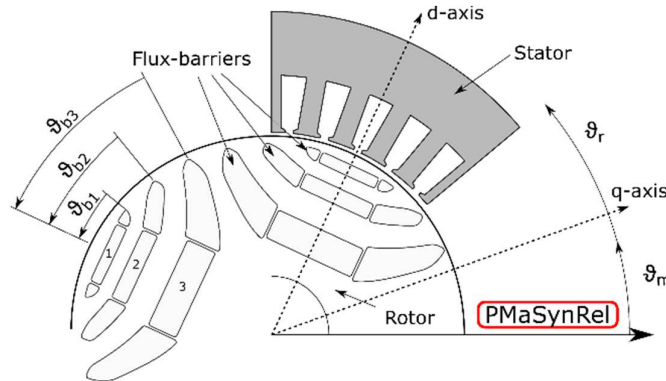
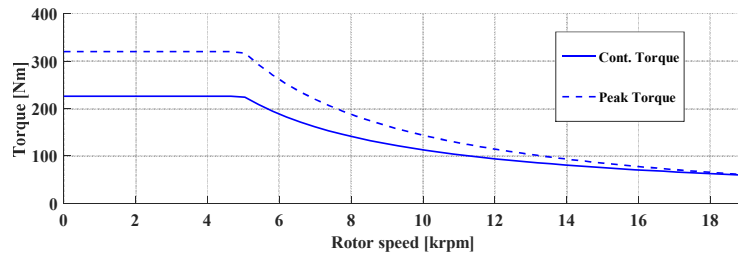


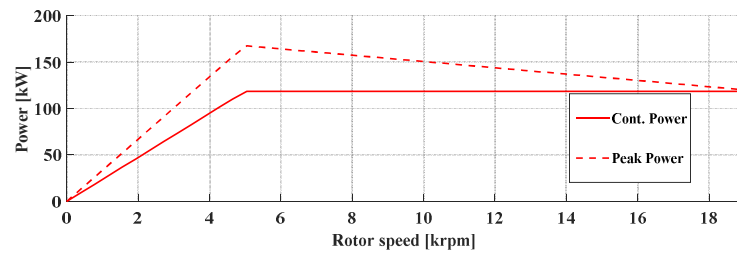
Fig. 3.2. Permanent Magnet assisted SynRel motor sketch.

TABLE 3.1. MOTOR GEOMETRICAL PARAMETERS

Name	Description
ϑ_{b1}	Flux barrier angle 1
ϑ_{b2}	Flux barrier angle 2
ϑ_{b3}	Flux barrier angle 3
W_{so}	Slot opening width
h_s	Slot height
W_{pmi}	Flux Permanent Magnetmagnet width
h_{pmi}	Permanent MagnetFlux magnet height



a)



b)

Fig. 2.3: Machine performance characteristic: a) speed- torque; b) speed-power.

3.2 Conclusion and Technical Considerations

In this chapter a tool has been presented to design an optimized electrical machine for a given technical specifications. The tool is flexible and aim to obtain the best solution with a reduced computational effort. The modeFrontier tool set the input parameter needed to the Matlab script to design the machine models in MagNet which runs the simulations providing the results necessary to the modeFrontier to set the next loop input parameter. Once set up the tool chain a huge number of machine topologies is possible to realize simply changing the input parameters.

As per equation 3.1, keeping the volume constant it is possible to increase the power density thank to the parameters B_g, A and ω_{mech} . The last one is possible to increase thanks to the significant development in power electronics switching devices and

magnetic materials, capable of withstanding greater mechanical stresses without compromising the iron losses [56]. The use of high switching frequency devices cause overvoltage in the winding, which could damage the slot and wiring insulation.

The magnetic load could be increase by the use of rare earth magnets, such as NdFeB, and core material able to operate in high flux density operative point. The industrial core materials can operate typically up to 1.8T, pricy materials, such us cobalt-iron, can operate up to 2.2 T. The current density could be increased adopting some strategies at winding design stage, as per Fig. 3.4, each carmaker has the own idea about the best winding topology.

	Jaguar I-Pace	Tesla 3	Chevy Bolt	BMW i3	Nissan Leaf	Toyota Prius IV	BMW 225xe	Audi A3 e-tron	Chevy Volt Gen 1	Toyota Prius III
Market introduction	2019	2017	2016	2013	2010	2017	2016	2014	2010	2010
Vehicle Type	BEV	BEV	BEV	BEV	BEV	Hybrid	Hybrid	Hybrid	Hybrid	Hybrid
Peak Power / (kW)	147	202	150	127	80	53	100	75	110	60
Peak Torque / (Nm)	348	416	360	250	280	163	180	330	390	207
Max Speed / (rpm)	13000	18100	8810	11400	10400	17000	14000	6000	9000	13500
No Poles	8	6	8	12	8	8	8	16	12	8
No Slots	48	54	72	72	48	48	48	24	72	48
Max. motor frequency / (Hz)	867	905	587	1140	693	1133	933	800	900	900
Skewing	Rotor skew	Rotor V-skew	No skew	Rotor lin.-skew	No skew	No skew	Stator skew	Rotor lin.-skew	Rotor V-skew	No skew
Winding type	Hairpin	Distributed	Hairpin	Distributed	Distributed	Hairpin	Distributed	Concentrated	Hairpin	Distributed

Fig 3.4. Traction Machines Overview in Automotive Industry [57].

Being this parameter crucial in term of power density and efficiency, hairpin winding and random distributed winding has been adopted for the research studies presented in this thesis. Motorette with both winding topologies has been built for experimental validations, within random winding trapezoidal slots has been designed instead the rectangular slots for the hairpin winding. Both kind of motorette has the same stack length value, the inner and outer stator radius is a bit different from random winding and hairpin winding. The second one allow higher copper fill factor inside the slot, a smaller stator permit the same performance of the random one. In addition, it has been necessary to do some variations from the optimized model in order to reduce costs and manufacturing efforts without losing the focus on the physical phenomena. The motorette material is M270-35A (EN10106) and to make easier to insert the copper inside the slot an open slot was adopted.

Chapter 4

Analysis on Random Winding

Nowadays, transport electrification is one of the most viable solutions to reduce CO₂ emissions and meet fuel economy requirements. Governments and automotive industries are pushing their research programs to realize hybrid and pure electric powertrains for both automotive and aerospace, and in general for all transport applications. For these applications became more and more important to maximize the power electrical machine power density. To achieve this goal it is necessary to increase the operative frequency as much as possible, the maximum limit is defined by the losses such as iron and copper losses in particular. The US Department of Energy (DOE) has recently announced technical targets for light duty electric vehicles with a goal to reach a power density target of 33 kW/L for a 100 kW traction drive system by 2025 [58]. The research is pushing a lot of effort to predict and reduce the high frequency losses especially to the copper losses considering that the iron losses need expensive material to be reduced.

Due to the aspects above discuss become very important to describe for a better understanding the high frequency losses phenomena in order to look for some strategy to reduce them. So far, numeric (Finite Element) and analytic approaches are commonly used to predict the losses, which are widely presented in literature, though only a few of them are also validated experimentally. Dowell [59] evaluated the variation with the frequency of the winding resistance and leakage inductance for single layer, multilayer and sectionalized windings. Ferreira [60] presented a model to calculate AC resistance taking into account skin and proximity effects in windings. Based on the Dowell's model, Wojda and Kazimierczuk [61] performed an optimization for solid-round-wire winding AC resistance.

Liwschitz-Garik [62] discussed the ratios of AC/DC resistance and inductance for other complex bar shapes. Reatti and Kazimierczuk [63] reviewed several analytical expressions

for the high-frequency winding resistance of inductors and compared the theoretical predictions against experimental results. Based on the subdomain models, the eddy current losses in windings of electric machines were calculated [64], [65]. In [66] proposes an analytical method for calculating the AC losses of arbitrarily arranged and connected conductors.

All previous models have been developed under the condition of perfect transposition of the wires across the axial length; hence, the circulating current phenomena are not evaluated. To the best knowledge of the authors, there are no methods capable to take into account all the individual contributions of the AC losses considering the real strands' positions.

In [67] A combination of finite element analysis (FEA) and experimental measurement has been employed to evaluate the components that contribute to the overall winding power loss. The work presented on [68] studies impact of the number of stator winding parallel strands on the additional AC losses distribution in the slot where this winding is located.

In [69] a FEA was been done to evaluate the impact of the parallel wires' placement.

In [70] a strand level Finite Element (FE) model has been generated to take into account all the contributing elements of the AC losses. It is demonstrated that Finite Element Analysis (FEA) gives very accurate results compared with experimental results if the position of each strands is controlled. A former is manufactured using 3D printing to fix exactly the position of the individual strands in an identical fashion to the ones considered in the FE analysis.

The analytical approaches for AC loss calculation are much faster when compared to FEA. On the other hand, they are accurate only under certain hypothesis, which are usually very far from the reality. In addition, the analytical approaches usually consider some geometry simplifications which are not always representative of a real case. For example, in the 1D models, the strand is assumed to be regularly positioned along layers through the tangential direction, whilst in the 2D models the strand is assumed to be regularly positioned along layers in the radial and tangential directions. FEA is very accurate in

predicting AC losses when considering a specific model that represents exactly the real wires' distribution.

In mass production usually the number of winding manufactured is very high. For random winding only a semiautomatic solution is possible; this means that all configurations present strand positions which are unique for each machine manufactured. The estimation of the losses in a winding, based on FEA, which takes into account only a specific wire distribution, could be affected by other errors, especially for high frequency application where the AC losses are significantly dependant on the frequency.

Thus, this design approach could lead to an overestimation or underestimation of the losses, considering that the even an automated (or semi-automated) manufacturing process cannot guarantee the same positioning of the wires for all the batches of machines produced. Furthermore, variations in AC losses will also affect the performance of the cooling systems, and a resultant hotspot is likely to lead to insulation failures.

FEA and analytical methods highlight an important drawback on the importance of predicting the strands' position which can significantly impact the accuracy of the result.

Furthermore in variable speed drives the mission profile that the electrical machine needs to deliver is possible only through the power electronic control. The latter introduces additional harmonics which can significantly increase the AC losses.

From the foregoing discussions, since it is impossible to predict the strands position in the slot, which are randomly displaced, and since their position can significantly affect the AC losses - especially at higher frequencies - the conventional (FEA and analytical) methods are not robust enough.

Therefore, to overcome the aforementioned issue, this work proposes an Experimental Statistic Method (ESM) which evaluates the probability to have a certain amount of losses. The ESM provides the parameters required to describe the probability density of the AC losses for a certain geometry and a certain winding configuration, which becomes useful in designing the winding especially for series production where the process is semiautomatic and the strands position changes every time.

4.1. Methods Adopted for AC Losses Evaluation

Generally the methods used to predict AC losses are mainly the analytical and FE. The analytical methods are the most challenging to implement in order to describe complex phenomena as the high frequency losses. In order to simplify a bit the real scenario some hypothesis are needed to introduce. The assumption mainly used in the literature is to assume that only the radial component of the magnetic field produce effects and the value of the tangential component could be assumed negligible compared to the radial one. This assumption is dependant with the slot geometry, as much higher is the ratio given by the slot high over the slot width as much true could be considered this assumption. In Fig.4.1 it is shown the magnetic field obtained by finite element simulations with three different slots geometry aiming to highlight how the magnetic field lines path change with the slot geometry. In the slot present in Fig 4.1 a) where the slot high/width ratio is equal to 1.8, to assume negligible the magnet flux tangential component could lead to an high error of the models.

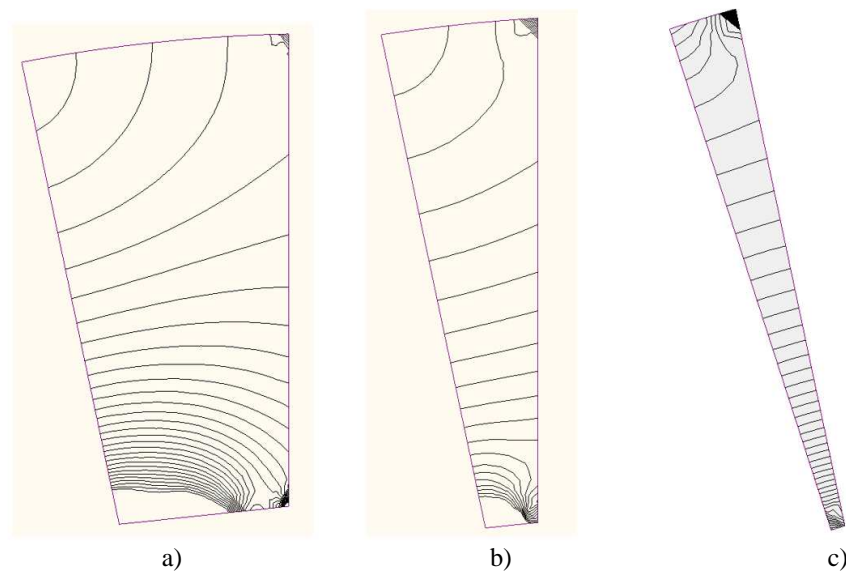


Fig. 4.1: Magnetic field path: a) ratio high/width equal to 1.8, b) ratio high/width equal to 3.8, c) ratio high/width equal to 7.2.

4.1.1. Analytical Method.

In the analytical model for the sake of the simplicity a monodimensional one has been considered. The total losses in high frequency are given as a contributions of four different terms as explained in eq.4.1:

$$P_{AC}(f) = P_{DC} + P_{skin}(f) + P_{prox}(f) + P_{circ}(f) \quad (4.1)$$

Where P_{DC} represent the DC losses, $P_{skin}(f)$ describe the skin effect, $P_{prox}(f)$ take into account the proximity losses and $P_{circ}(f)$ take into account the circulating current losses. It is possible to analytically calculate the DC losses accurately by knowledge of the winding DC resistance:

$$R_{DC} = \frac{n_{turns} \rho_{cu} l_{stk}}{Area_{cu}} \quad (4.2)$$

Where n_{turns} is number of turns, ρ_{cu} is the copper resistivity, l_{stk} is the stack length, while $Area_{cu}$ is the copper cross section.

The DC losses can be reduced by increasing the slot fill factor. Without significant loss in accuracy, P_{skin} and P_{prox} can be neglected in the end winding [71]. It is possible to express the other elements of (4.1) with a dimensionless AC loss factor K_{AC}

$$P_{AC} = K_{AC}(f) * P_{DC} \quad (4.3)$$

K_{AC} is a function of η which define the ratio between the conductor diameter D and the skin depth δ .

$$\eta = \frac{D}{\delta}; \delta = \sqrt{\frac{1}{\pi * \sigma * f * \mu_0}} \quad (4.4)$$

Where σ is the copper conductivity and μ_0 is the void permeability.

The analytic models are generally limited by the hypothesis adopted. Often they are not fully satisfy in the realty but they are necessary to reduce the complexity of the models otherwise it could became very difficult to manage. In this case, the aim of the model is

to have a feeling about how the phenomena behave with the frequency without losing too much in accuracy.

The authors in [72] considered the following assumptions:

- 1) Permeability of iron core is infinite;
- 2) End effects are neglected;
- 3) Magnetic field lines are horizontal across the slots;
- 4) Sinusoidal current is applied to conductors;
- 5) Conductors are positioned in floors with height equal to the diameter of conductors D as shown in Fig.4.2.

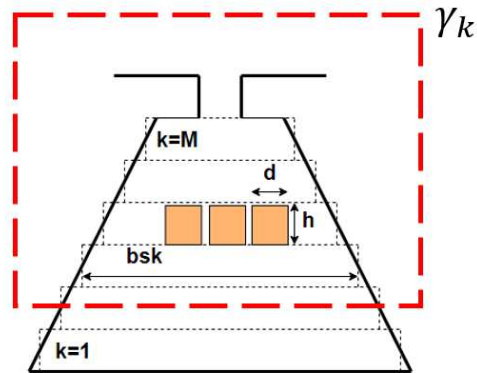


Fig. 4.2. Sketch of one slot: discretized domain.

Being the circuit current feed, with current sinusoidal alternating with the time, thanks to the linear material the electric field intensity E , current density J , magnetic field intensity H and magnetic flux density B are sinusoidal alternating with time. Phasors expressions could be used as following:

$$\check{E} = E_0 e^{i\varphi_0} \quad (4.5)$$

$$\check{J} = J_0 e^{i\varphi_0} \quad (4.6)$$

$$\check{H} = H_0 e^{i\varphi_0} \quad (4.7)$$

$$\check{B} = B_0 e^{i\varphi_0} \quad (4.8)$$

Applied the Ampere law (eq.4.9) to the red circuit k in Fig.4.2 we obtain the eq. 4.10

$$\nabla \times B = \mu J \quad (4.9)$$

Where $B = \mu H$

$$H b_{sk} = \int_{y_{k-1}}^{y_k} -J_k b_{ck} dr + I_{0k} \quad (4.10)$$

The total width of the conductors in the k-th layer is

$$b_{ck} = d n_k \quad (4.11)$$

Where d is the width of each conductor, and n_k is the number of conductors in the k-th layer.

I_{0k} is the total current below the k-th layer as per eq.4.12

$$I_{0k} = \sum_0^{k-1} i_o n_k \quad (4.12)$$

Taking the derivative to (4.10) we obtain :

$$\frac{\delta H}{\delta r} = \frac{-j b_{ck}}{b_{sk}} \quad (4.13)$$

Applying the Faraday's law (4.14) to the circuit k in Fig. 4.2.

$$\nabla \times E = -\frac{\delta B}{\delta t} \quad (4.14)$$

Where $J = \sigma E$;

Eq.(4.14) becomes :

$$\frac{\delta J}{\delta r} = -\mu \sigma \frac{\delta H}{\delta t} = -j \omega \mu \sigma H \quad (4.15)$$

Taking again the derivative to (4.13) and substituting in (4.15) we obtain:

$$\frac{\delta^2 H}{\delta r^2} - \frac{j \omega \mu b_{ck}}{b_{sk}} H = p^2 H \quad (4.16)$$

The general solution of (4.16) is given by

$$H = C_1 e^{-pr} + C_2 e^{pr} \quad (4.17)$$

Where

$$p = \frac{1+j}{\delta} \quad (4.18)$$

$$\delta = \sqrt{\frac{b_{sk}^2}{b_{ck} \omega \mu \sigma}} - \text{skin depth} \quad (4.19)$$

C_1, C_2 are given by the boundary conditions below;

$$H = \frac{I_{ok}}{b_{sk}} ; r = 0 \quad (4.20)$$

$$H = \frac{I_{ok} + I_o n_k}{b_{sk}} ; r = h \quad (4.21)$$

The current density in the kth layer is:

$$J_k = - \frac{I_k p \cosh(pr) - I_{k-1} p \cosh(p(h-r))}{w_{sk} \sinh(ph)} ; r \in [0, h] \quad (4.22)$$

Through Ohm's law we obtain the losses in the kth layer

$$P_k = \iiint_0^{vol} \frac{J_k^2}{\sigma} dv = lck w_{ck} \int_0^h \frac{J_k^2}{\sigma} dr ; r \in [0, h] \quad (4.23)$$

3.1.2. Finite Element Model

To evaluate the AC losses with more accuracy is often used a numerical method such as finite element analysis. In this study 2D models and the simulations have been performed thorough MagNet from Mentor Graphics. Being our goal to describe the phenomena that occur inside the slot a detailed approach is needed; all conductors are modelled singularly as a coil in order to achieve a strand level analysis as per Fig.4.3.

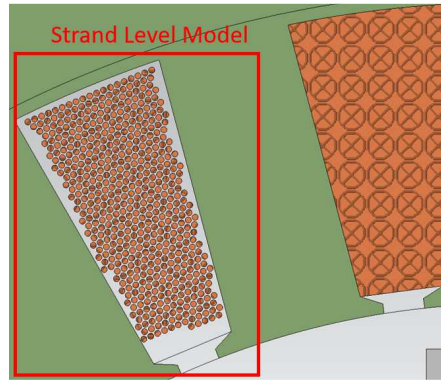


Fig. 4.3. Detailed Model.

The results of this analysis is very dependent of the mesh size. To have a good accuracy with an acceptable computational effort, the strategy to intensify the mesh elements on the region mainly interested by the phenomena under analysis has been adopted. In addition to catch the field variation inside each conductors dozens of elements are needed.

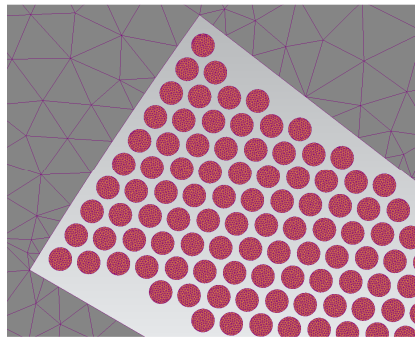


Fig. 4.4. Strand Mesh Definition.

The stator core is made using silicon iron (SiFe) laminations of grade M270-35A. The coil's material is copper with a conductivity of 5.77×10^7 [S/m]. Two different stators featuring trapezoidal slots and with 2 and 4 slots per pole per phase (q) respectively, are considered in this work. Usually to allow an higher current several parallel path are used in the winding. In each slot are present different turns and each turns it is made by different parallel path, the number of strands in parallel are technically called "strands in a hand" or "bounle". The turns are placed randomly inside the slot, in this study we analyse to extreme scenario where the turns are placed vertically (VT) or horizontally (HZ) to have a feeling also about this variable dependent from the manufacturing process.

Fig. 4.5 shows in detail the FE models where each bundle is highlighted with a different color. In Fig. 4.3 (a) and (b), where the slot per pole per phase number is ' q ' = 2 (q_2), the turns are distributed vertically (VT) in (a) and horizontally (HZ) in (b), respectively. The turns, all in series, are numbered from 1 to 16. On the other hand, in Fig. 4.3 (c) and (d), for $q = 4$, the turns are numbered from 1 to 8, with (c) and (d) corresponding again to vertical (VT) and horizontal (HZ) distributions, respectively.

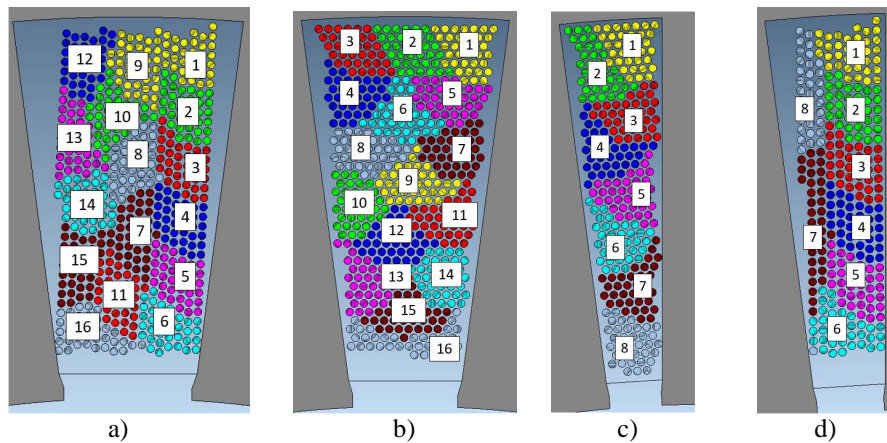


Fig. 4.5. Finite Element Models: a) q_2 _VT, b) q_2 _HZ, c) q_4 _VT, d) q_4 _HZ.

Since the AC losses significantly depend on the leakage flux in the slot [71], it is possible to neglect the rotor and the other phases contributes without losing to much in accuracy according to the [73] where a model reduction analysis has been evaluated. The model presented could be easily adapted to all winding configurations being at strand level. After these considerations, only one slot was modelled at the stranded level in order to reduce the computational time. The AC losses are then given by the modelled slot multiplied by the number of slots per phase. To reduce the computational time and in order to have an accurate estimation, two different circuits are realized as shown in Fig.4.6 (c) and (d). The first circuit, which is more time consuming, considers all the strands in the slot and each conductor is defined as "solid" in order to consider the uneven distribution of the current. The second circuit considers that the rest of the slots are defined as "stranded", where the current distribution is considered even, this circuit is necessary to create the flux density

distribution on the yoke close to the reality in order to avoid wrong estimation for the iron losses. Using the MagNet software is not possible to make one single circuit because is not able to run the simulation when "strand model" conductors and "solid model" conductors are in series in the same circuit, two different circuit are necessary. This methodology presents the advantage of a lower computational time, while it estimates the copper losses and reproduces the flux density distribution in the slot accurately. In case a short pitch or a double layer winding is present, we need to pay attention and assign correctly the relative currents to each conductors, as much higher is the complexity of the configuration as much higher is the computational and modelling effort to pay.

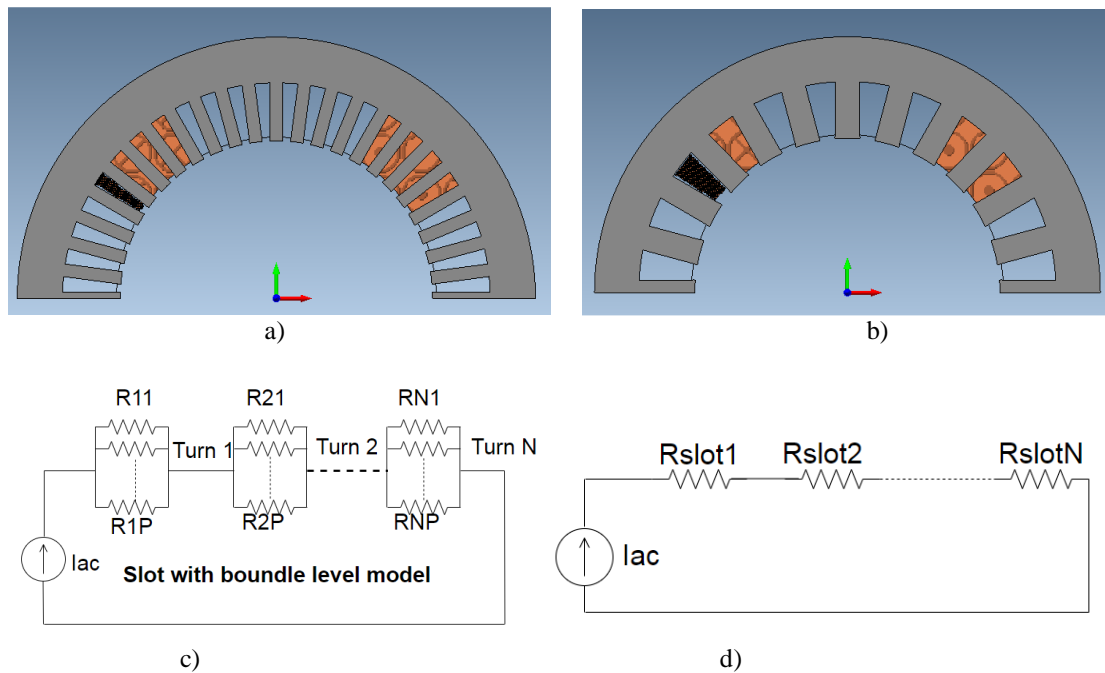


Fig. 4.6. Finite Element Models: a) motore_q4, b) motore_q2, c) circuit of detailed slot, d) circuit of non detailed slots.

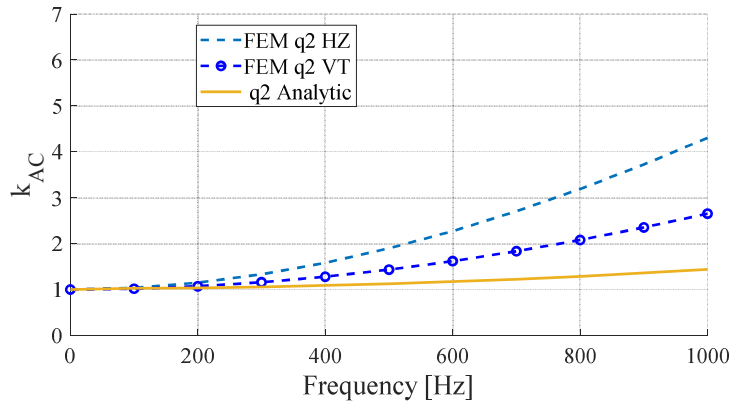
4.1.3. Results

A comparison between the analytical model used to predict the losses of a single slot and the finite element model considering the losses only of circuit in Fig. 4.6. c) has been done. In the FEA, the circuit, shown in Fig.4.7, is energized with a sinusoidal current with RMS values of 7 A and 14 A. For each current value, the frequency is varied from 0Hz to 1000

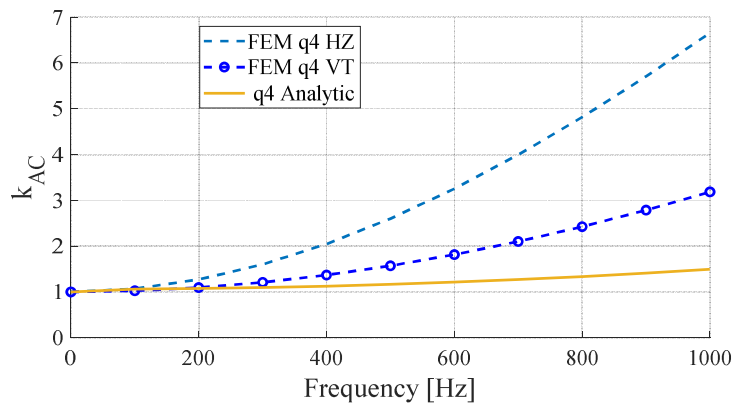
Hz, in steps of 100Hz. The results confirm that K_{AC} is independent from the current magnitude as expected being a linear problem.

In Fig. 4.9 the current distribution and the flux density map are shown. The two slots in both Fig. 4.9 a) and b) show that one slot is representing all individual strands, while the adjacent slot is without strands.

In Fig. 4.8, K_{AC} as obtained from FE and analytical methods is shown as a function of the frequency. It is clear that there is a mismatch between the analytical results and the FE ones, especially for frequencies above 200 Hz. This difference is because the analytical model considers a 1D field and it is not able to capture the circulating current contribution which occur in each parallel wire of a turn. The FEA considers a 2D field and thus it is able to capture also the circulating current effect as shown in Fig.4.9. It is important to highlight to the reader that the analysis done to the stators with $q=4$ and $q=2$ aim to prove that the models already described and the method presented below is valid for all topologies. It is a quite intuitive that for a given inner and outer radius stator the K_{AC} could be lower with higher slot per pole per phase number reducing the slot width value. For easy of comparative reference, in Fig. 4.7, the error between FE and analytical prediction is shown. In addition, as the frequency increases, the FE analysis shows that the influence of the positions on the AC losses increases as well.



a)



b)

Fig. 4.7. Analytical Vs FEA results: a) Stator with $q=2$, b) Stator with $q=4$.

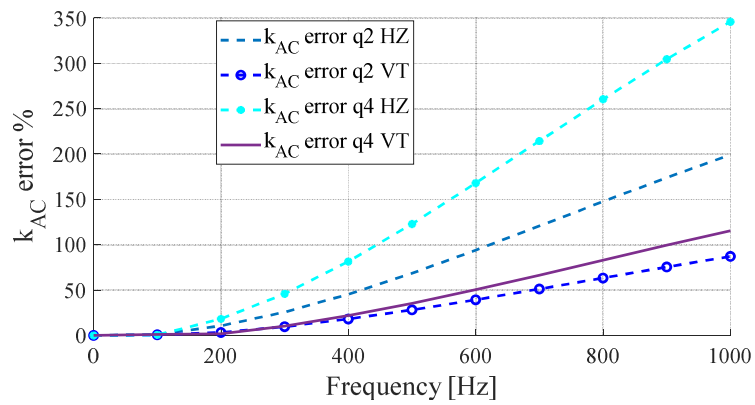


Fig. 4.8. K_{AC} error between analytical method and FE models.

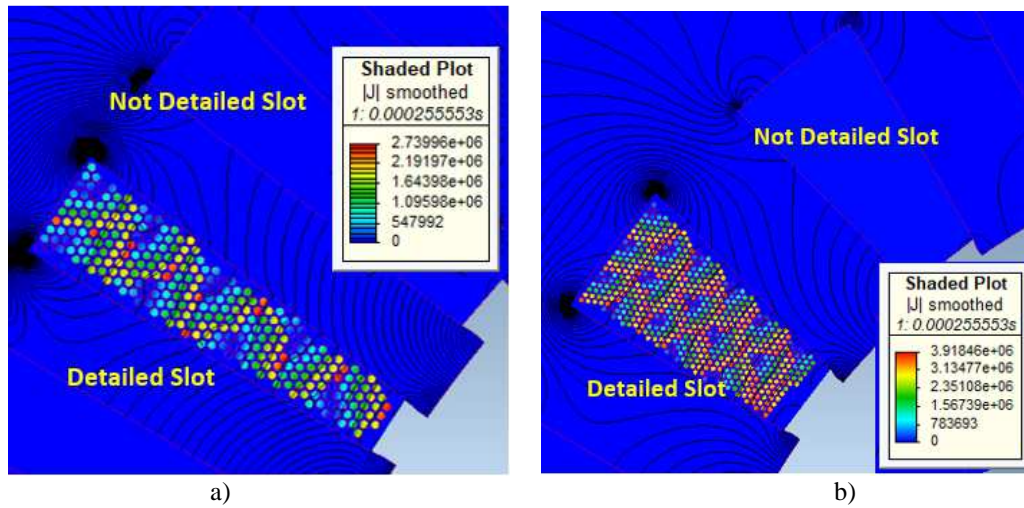


Fig. 4.9. Current density distribution: a) Stator_q4, b) Stator_q2.

The positions of each strands influence the own impedance of them being different the linked flux. These cause different strands impedance values with different currents. In Annex 1 the time harmonic simulations of the case presented in Fig. 4.5 c) has been shown. There are collected in a table the current magnitude and phase value for each strand (numbered from 1 to 35) of the same bundle, when two different frequencies have been applied, 100Hz and 1000Hz. In the second case the magnitude and phase between two strands could be very different, the current through the conductors named std_1 and std_35 have around 200 degree phase shift between each other's, this lead to circulating currents between parallel strands with a considerable copper losses increasing.

4.2. Proposed Method for Losses Evaluation

4.2.1. Theory of Statistics

As demonstrated in the previous section, the AC losses are dependent on the strands' position. It is impossible to predict without any error the strands' position. The error in predicting the strands' position can be considered as a random variable, and in such case a statistical approach is needed.

Each error obtained in predicting the AC losses during a measurement can be called an observation. A large set of 'N' observations represent the population, while a small set of 'n'-observations represent a sample. The probability distribution describes the probability to have the event x_i of the population. Different types of probability distribution are present.

The central limit theorem says that, under conditions almost always satisfied in the real world of experimentation, the distribution of a linear function of errors will tend to a normal distribution as the number of its components becomes large. In [74], it is stated that at least thirty events are required in order to have an approximation to a normal distribution.

The function of the normal distribution eq.(4.24) is fully described by two parameters : mean μ described in eq.(4.25), called also the mathematical expectation of x_i and the standard deviation in eq.(4.26) which define the spread of the distribution. These two parameters are important to provide information also for the other kind of probability distribution present in literature. Fig. 4.10. shows the normal distribution for different values of standard deviations.

$$f(x) = \frac{1}{\sigma \sqrt{2\pi}} e^{-\frac{(x-\mu)^2}{2\sigma^2}} \quad (4.24)$$

where

$$\mu = \frac{1}{N} \sum_i^N x_i \quad (4.25)$$

$$\sigma = \sqrt{\sigma^2} = \sqrt{\frac{\sum_i^N (x_i - \mu)^2}{N}} \quad (4.26)$$

The range $\mu \pm \sigma$ has the 68% of the probability to include an event x_i , while for the range $\mu \pm 2\sigma$ the corresponding probability is 95%. The greater the range the higher is the probability that it includes an event x_i . The normally distributed quantity 'x' is often best expressed in terms of a standardized normal deviation as per eq. (4.27). Using the values reported in [74] it is possible to obtain the probability of the event x_1 .

$$z_i = \frac{(x_1 - \mu)}{\sigma} \quad (4.27)$$

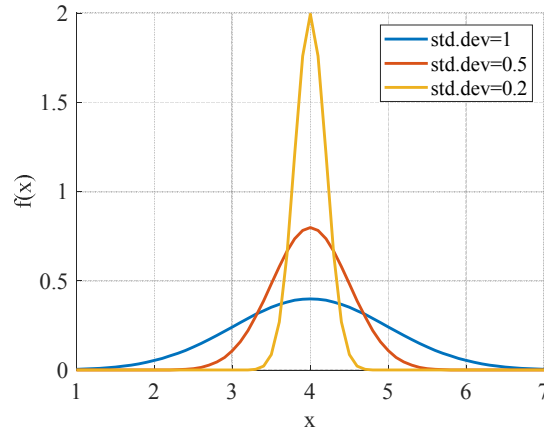


Fig. 4.10. Normal Distribution Example with $\mu = 4$ and $\sigma = 1, 0.5, 0.2$.

4.2.2. Description of the Experimental Statistical Method (ESM)

Since it is impossible to predict the position of each strand in a random winding, an ESM is proposed to address this issue. AC losses are highly dependent on the strands' positions, which can have a number of different combinations. This method aims to identify the parameters needed to define the Probability distribution of AC losses for a certain winding configuration. Using the same amount of copper in the winding in order to maintain the same length, material properties and DC electrical resistance, the motorettes which are a section of the stator as shown in Fig.4.11. are physically wound for thirty times in order to have thirty events of x_i .

For each configuration the AC losses are evaluated for two different RMS current values (7 A, 14 A) and in a frequency range from 100 Hz to 1000 Hz. Mean and standard deviations are calculated for each frequency.

4.3. Case Study

The machine designed was thought for an traction application described in chapter 3, with peak power equal to 160 kW and 19krpm as maximum speed. To reduce the manufacturing costs of the hardware needed to validate the concept proposed before, some considerations has been token into account. According to [70] it is sufficient to wind motorettes instead the full stator for a good approximation of the AC losses, in this study

the meaning of the motorette is to proof the validity of the method proposed with a reduced cost. In addition, it is needed to highlight that to estimate the real total losses in the machine it is necessary to consider all series coils of the total phase and in addition the circulating currents depend from the uneven distribution due to the total per strand and phase inductances of all the parallel strands of the complete phase.

Two motorettes with trapezoidal slots are prototyped, with 2 and 4 slot per pole per phase are shown in Fig.4.12. The motorettes are half of the full stator and only one single phase has been wound rrepresenting half of the total phase in the full motor as per Fig.4.12. Each motorette has been wound thirty times in order to create a population with thirty independent events according to paragraph 4.2.1. To obtain these events as much independent as much possible was asked to the technician to wind the motorette randomly without particular technics in order to avoid any correlations between each events. In Table 4.1 and 4.2 details about stator and windings respectively are provided.

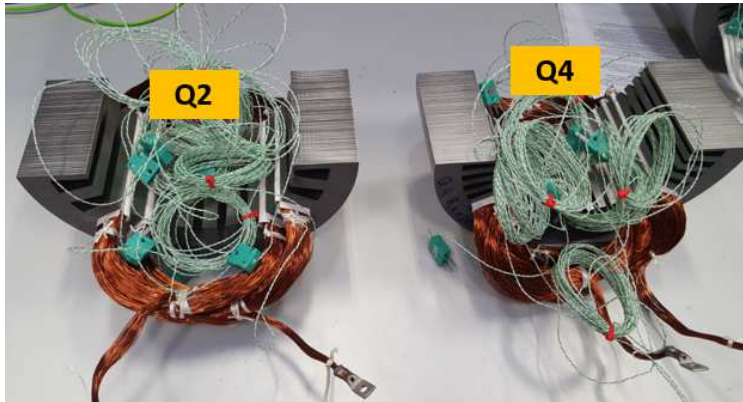


Fig. 4.11. Case study motorettes: with $q=2$ (left hand side) and $q=4$ (right hand side).

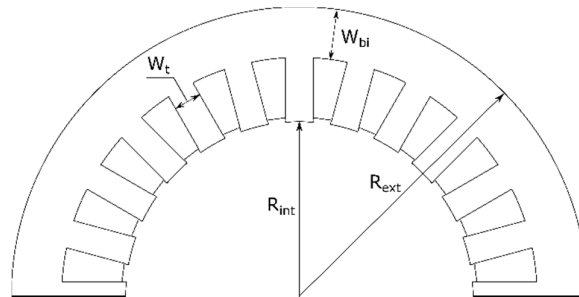


Fig. 4.12. Motorette parametric drawing.

TABLE 4.1. MOTORETTE GEOMETRICAL PARAMETERS .

PARAMETER	DESCRIPTION	VALUE(MM)	
		Q2	Q4
RINT	INNER STATOR RADIUS	65	65
REXT	EXTERNAL STATOR RADIUS	116.12	116.12
WBI	BACK-IRON HEIGHT	20.4	20.4
WT	TOOTH WIDTH	10	5

TABLE 4.2. WINDING DETAILS.

PARAMETER	VALUE	
	Q2	Q4
STRANDS IN HAND	32	32
TURNS PER PHASE	16	8
COPPER DIAMETER(MM)	0.56	0.56
SLOT FILLING FACTOR (%)	44	44

4.4. Experimental Characterization

4.4.1. Experimental Rig Setup

As mentioned in the introduction, two different experimental tests have been performed in this research. The first one aims to define the parameters (μ, σ) needed to have a description of the function distributions with the circuit energized with a pure sinusoidal current as shown in Fig.4.13. The second one aims to represent a scenario closest to the reality where the motors is always drove by an inverter in the applications. With this scope the losses are estimated when the motorettes are supplied by a PWM converter as shown in Fig. 4.14.

A. Set-up for circuit fed with Pure Sinusoidal Current

A variable frequency power supply (CHROMA 61511, Programmable AC source up to 1kHz) is used to supply the motorettes. The total power loss is measured by a precision power analyzer (PPA 5530), shown in Fig.4.13. The accuracy of the instrument declared in its catalogue is enough higher to guarantee an reliable value. All the measurements are taken at the same winding temperature (20°C) to have the same resistivity value. The winding temperatures, during the tests, are monitored in real time with six K-type thermocouples placed in different positions inside the slot, in the end-windings and connected to a PICO

TC-08 data logger. A cooling fan is used to cool down the motorettes to have a stable temperature value and make the process faster.

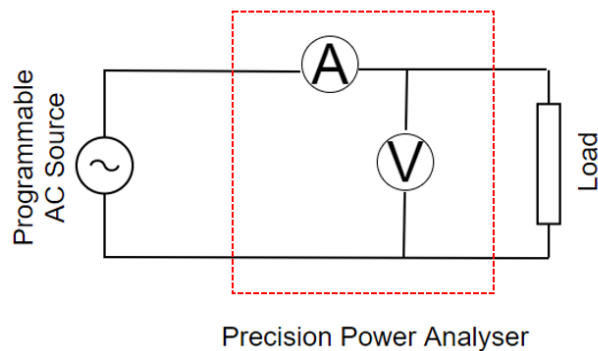
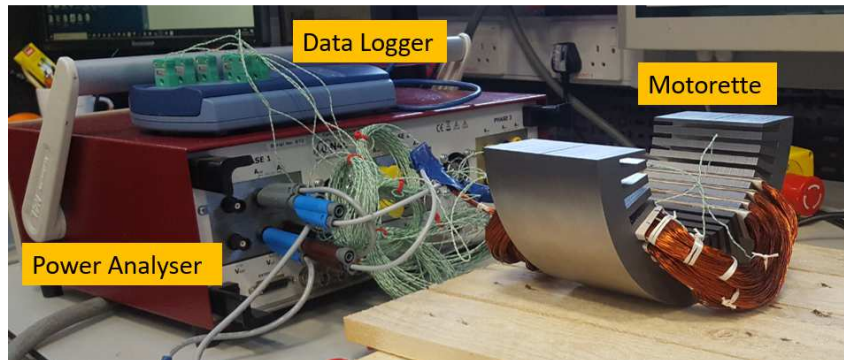


Fig. 4.13. Pure sine wave experimental set up and schematic layout.

B. Set-up for circuit fed with Inverter

In this case, the motorettes are supplied by a full bridge converter. In order to quantify the harmonics contribution, an oscilloscope is used.

The DC/AC inverter shown in Fig. 4.14 is controlled by a custom control platform built around the Microzed board based on the Zynq SoC (System on Chip) from Xilinx.

Sampling and switching frequencies are synchronized. The inverter is a custom DC/AC converter based on Silicon Carbide power modules (CAS120M12BM2) from Wolfspeed, a CREE company. The maximum switching frequency allowed by the custom gate drivers is 40kHz. Cooling system is air forced through the heatsink. Also here a cooling fan is used to cool down the motorettes and all the measurements has been kept at the same temperatures

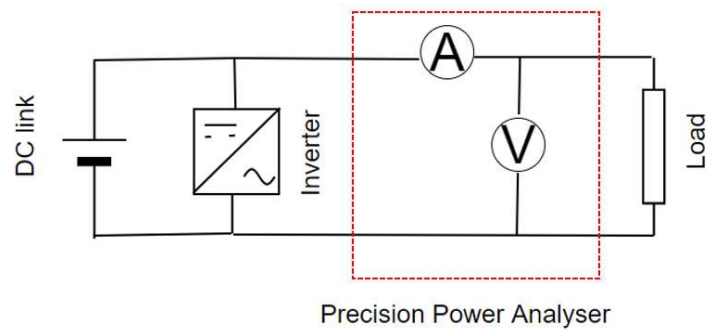
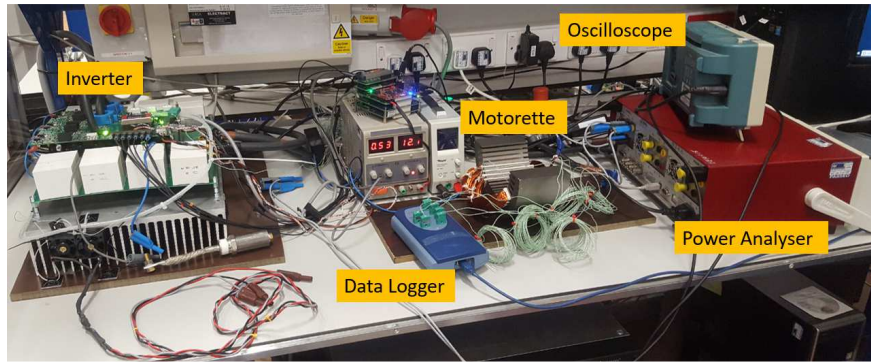


Fig. 4.14. PWM experimental setup and schematic layout.

4.4.2. Iron loss estimation via Finite Element

During the tests, the value measured represent the total losses due to the contribute of the iron and the copper. Experimentally it is impossible to separate these contribute and identify separately the copper losses contribute and the iron losses contribute. Therefore, an iron loss estimation is needed, in this work them has been evaluated via finite element and the results obtained has multiplied for a factor equal to 1.5 to take into account also the increasing due to the manufacturing process being the software not able to consider its. The iron losses were calculated at the same operative frequencies used to do the tests below described.

For sinusoidal excitation, the iron loss generated in the laminated core stack are calculated by the finite element software using the Steinmetz equation in each element of the meshed region and then averaged over the entire volume:

$$P = K_h f^\alpha B^\beta + K_e (sfB)^2 \quad (4.28)$$

Table 4.3 lists the material coefficients used for the iron loss predictions, which were derived from curve fitting of (4.28) from the material data provided by manufacturer for M270-35A with lamination thickness (s) equal to 0.35mm.

TABLE 4.3. MATERIAL COEFFICIENT FOR 0.35 MM SILICON IRON LAMINATION (20C).

PARAMETER	VALUE
A	1.207
B	1.771
K_h	0.009
K_e	3.244E-05

4.5. Experimental Validation of the ESM

In this section, the results obtained with the two different setups are shown. The aim is to define the parameters useful to describe the distribution which are needed to predict the AC losses for this case study. In addition, the losses of the winding supplied with the PWM controlled inverter are experimentally evaluated for different switching frequencies to have a sensibility also about the dependence of the losses from harmonics and switching frequencies as well.

4.5.1. Motorette fed with Pure Sinusoidal Current

Thanks to the equations (4.25) and (4.26) it is possible to calculate the mean (μ) and standard deviation (σ), where x_i is the K_{AC} of each measurement, while N is the total number of measurements, which in this case is equal to 30. For the sake of the clarity, the motorettes has been wound 30 times, each time, the losses for a frequency range from 0 Hz to 1000 Hz stepped 100Hz has been taken keeping the temperature constant. For each frequency step 30 values were available, from these the iron losses estimated via finite element has been subtracted in order to have only the copper losses for a given frequency. At the end these 30 values were the ones useful to calculate the mean and the standard deviation. The P_{DC} for both motorette is measured with a precision power meter

for 7 amps and 14 amps. The motorette with $q=2$ has $P_{DC} = 2.55W$ and $P_{DC} = 10.21W$ respectively for 7amps and 14amps, instead the motorette with $q=4$ has $P_{DC} = 2.46W$ and $P_{DC} = 9.86W$. In Table 4.4 there are these values obtained for the two motorette configurations at different frequencies. From the same table, the variance of K_{AC} increases with the frequency, it means that the range of the possible losses value increase as well. This confirms that the higher the frequency, the greater is the dependence of the losses on the position of the conductors. Fig. 4.15 and Fig.4.16 show the losses evaluated with the three methods at 1000 Hz, for 2 and 4 slots per pole per phase. With the red line is given an approximation of the distribution of to the histogram diagram which represent the experimental results with the KAC value in the x-axis and in the y-axis there are the frequency of measures with KAC in a defined range.

The analytical model shown a difference with respect to the experimental results, as expected, being unable to describe all the loss contributions. This method can lead to a wrong design of the cooling system.

In a production environment, with a considerable number of motors, the most reliable value to consider is the mean (μ). Around 68% of the windings manufactured have a value inside the range $\mu \pm \sigma$. The FEM method provides results that are true only for some particular cases, with a low probability to be verified. For example, considering the model FEM_q4_HZ at 1000Hz, thanks to the eq.4.27, where x_i is the K_{AC} value of the model (equal to 6.655), while μ and σ are in the Table 4.4, it is possible to note that this event has the 0.0158% of probability to be verified.

The FEA can represent only a particular case that could be the worst one or the best one. Considering the models FEM_q4_HZ and FEM_q4_VT the first one has KAC more than double compared to the second one. These values can underestimate or overestimate the losses and can lead to an inappropriate design of the cooling system.

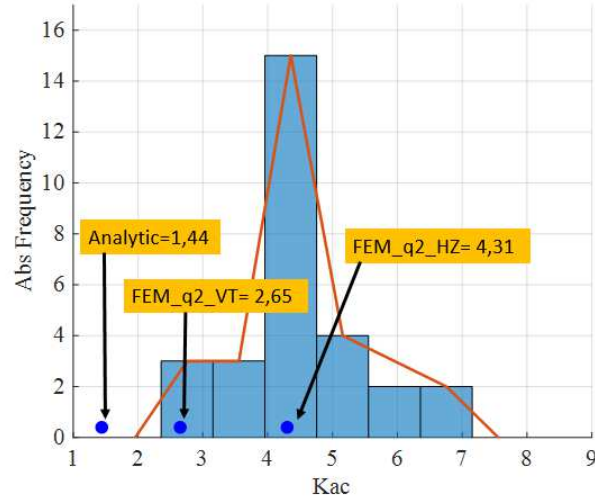


Fig. 4.15. Experimental Absolute Frequency of K_{AC} for motorette with $q=2$ at 1000Hz.

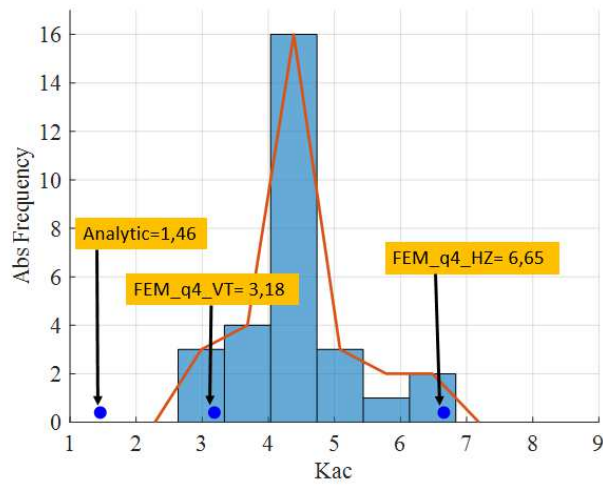


Fig. 4.16. Experimental Absolute Frequency of K_{AC} for motorette with $q=4$ at 1000Hz.

TABLE 4.4. μ AND σ VALUE OF K_{AC} PROBABILITY DISTRIBUTION.

Frequency (Hz)	μ		σ	
	Q2	Q4	Q2	Q4
100	1.30	1.20	0.14	0.10
200	1.81	1.36	0.41	0.16
300	2.23	1.64	0.54	0.31
400	2.61	1.96	0.61	0.39
500	2.93	2.26	0.71	0.48
600	3.30	2.59	0.85	0.56
700	3.71	2.95	0.90	0.64
800	4.00	3.38	1.06	0.86
900	4.29	3.78	1.21	0.96
1000	4.75	4.12	1.30	1.18

4.5.2.Motorette fed with Inverter

These tests are still more closer to the reality compared to the pure sine scenario because always the motors are driven by an inverter during an automotive application. For this tests only one single winding configuration has been evaluated, not 30 as in the previous test because out of the scope of these tests. Being the harmonics related to the switching frequency three different values has been evaluated: 10kHz, 20kHz and 40kHz (maximum switching frequency of the converter), these are typical values which we can find in the industry market.

Fig. 4.17 shows the waveforms of the three different currents feeding the circuit.

Fig. 4.18 and Fig.4.19 shows the increment of AC losses, represented by the loss factor coefficient K_{AC} , due to the PWM effect. Compared to the pure sinusoidal current, the total losses increase up to 35% when the fundamental is 1000 kHz as per Table 4.5 and Table 4.6, only three frequency steps are considered. It is worth to notice that in a full motor where the inductance is higher this increment due to the inverter is limited. The mean of Table 4.5 and 4.6 is to make the reader aware that the losses scenario is a quite different when an inverter is present and this should be considered at design stage.

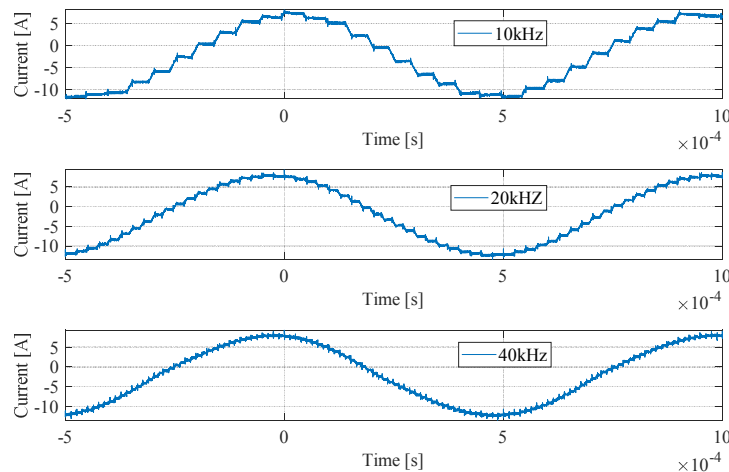


Fig. 4.17. Current waveforms for different switching frequencies: 10kHz, 20kHz, 40kHz.

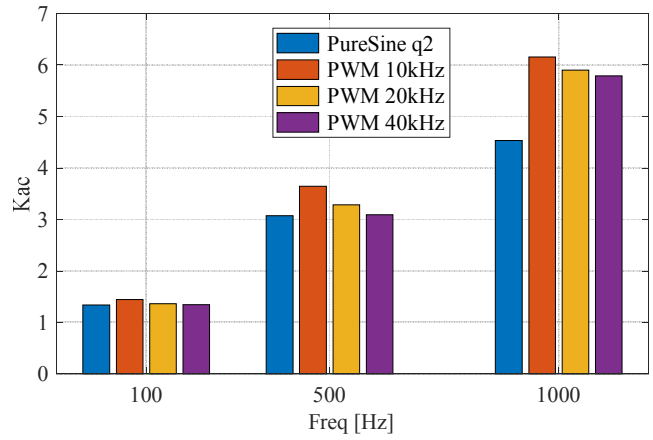


Fig. 4.18. Experimental K_{AC} obtained with pure sine and PWM for $q=2$.

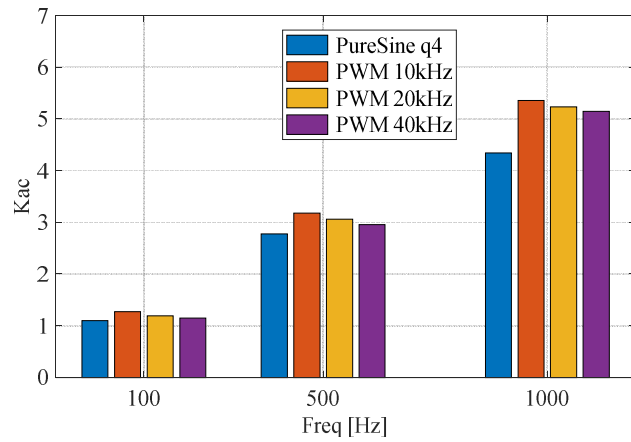


Fig. 4.19. Experimental K_{AC} obtained with pure sine and PWM for $q=4$.

TABLE 4.5 INCREASING OF LOSSES COMPARED WITH PURE SINE Q2.

Frequency (Hz)	PWM_10	PWM_20	PWM_40
100	2.45%	0.53%	0.19%
500	12.57%	4.66%	0.4%
1000	35.72%	30.17%	27.71%

TABLE 4.6 INCREASING OF LOSSES COMPARED WITH PURE SINE Q4.

Frequency (Hz)	PWM_10	PWM_20	PWM_40
100	3.98%	2.18%	1.14%
500	9.35%	6.53%	4.15%
1000	23.31%	20.44%	18.47%

4.6. Conclusion

In production lines where the machine design is the same for all batches, the strand position is not controllable by the manufacturing process, it means that all machines present windings with some differences in the strands distribution and different thermal behaviour will occur during the machine life because of the different copper losses.

In the literature the analytic and FE methods are used to predict losses but they are not able to predict the random position of the real winding, this methods have some limitations has explained and proved during this chapter and this limitation could lead the designer to underestimate or overestimate the copper losses providing wrong input information at cooling system design stage. The FE methods represent only some specific cases of the total possible in the realty, it is impossible to control how far could be the results of the FE models from the mathematical expectation. For future research investigations a tool able to create a huge number of combinations could be interesting to develop in order to

obtain the losses probability distribution with a limited effort in term of time, costs and facilities.

To face this limit, an Experimental Statistical Method (ESM), which is able to predict the AC losses in randomly distributed windings has been developed. The aim of the work is to determine the parameters needed to define the probability distribution. Once obtained this parameters it is possible to determine the losses with a certain probability that they happen in the realty. The ESM aim to give parameters to obtain reliable losses value for the winding configuration and the slot geometry selected at design stage.

Being the ESM very complex and expensive the easiest case study has been analysed to prove the validity of the method proposed.

The method could be extended also to the real three phase winding machine, of course the mean and standard deviations is supposed to be different being different the case study. Many correlations between geometry and results is possible to investigate with this method. For future research works, it could be interesting to evaluate the mean and standard deviations for different slot geometry keeping constant the slot height/width ratio, fill factor (influencing the number of possible combinations), strands in a hand and the number of turns. If the losses probability distribution is constant, the mean and standard deviations are valid for a group of machine geometry and not for only one single case.

The scope of this work during the thesis was to set the basis for future research activities of a method more reliable than the analytical and finite element methods.

Chapter 5

Strategies to Reduce AC Losses Hairpin Winding

To mitigate the AC losses phenomena, Litz wires are often used. However, they also have some disadvantages, such as complex shaping and impregnation, low fill factor and high manufacturing costs [75]. Hence, their use is only justified in very high frequency and no cost-sensitive applications. Therefore, most commonly, random-wound windings are employed. This winding typology represents a good trade-off between costs and performance. Also in this case the conductors can be subdivided in parallel strands, but their cross section is higher than those of a Litz wire. This kind of winding is a very competitive solution in automotive where a low number of turns is typically chosen to achieve low voltages and high currents [76].

This level of flexibility cannot be achieved when using bar-wound windings, more often named as hairpin winding [77]. Due to their pre-formed nature, the subdivision in strands cannot be flexibly applied, the number of turns is always even and the maximum number of conductors per slot is limited. The stress on insulation and conductive materials can be excessive when bending and twisting operations are not properly performed [78], [79]. Therefore, only a few configurations are feasible and can be manufactured [80], [81]. However, hairpin windings achieve a higher fill factor compared to the winding types mentioned above, thus obtaining higher current density and peak torque. In addition, in a series production context, a fully automated manufacturing process is possible, potentially reducing the associated costs [82]. Hence, this winding technology is currently seeing an ever-increasing interest for transport applications.

Nevertheless, the main bottleneck for the hairpin winding widespread is represented by the elevated AC losses at high frequency operation [83]. Current research efforts include new winding concepts and methodologies to overcome their high frequency challenges, as

well as advanced models for AC losses prediction. Contrarily to random windings, where the main error in modeling AC losses comes from the unknown strands position [84], in hairpin windings a more accurate AC losses estimation is possible thanks to the a-priori knowledge of the conductors' position.

A review of analytical models to calculate the AC losses for rectangular wire inside the slot is presented in [85].

A 2D analytical model able to calculate AC losses is presented in [86]. In [87], a comparison between random and hairpin windings is carried out always in terms of AC losses. In [88], innovative winding patterns that can significantly reduce AC losses are introduced, whereas the updated analytical models to predict AC losses in such new winding concepts are also proposed.

However, a sensitivity study on how the number of slots-per-pole-per-phase, the number of layers-per-slots and the slot fill factor impact the AC losses in hairpin windings is interesting to investigate. These parameters, when the outer stator radius is constant, have a direct impact on the slot geometry and on the bars' cross sections, which are thus also evaluated. In addition, a 1D analytical model is first described and then validated against finite-element (FE) evaluations, highlighting inaccuracies under some geometrical conditions at very high frequencies (>1 kHz). Therefore, the FE method is used for the sensitivity analysis performed in this work.

5.1. Models to predict high frequency copper losses

5.1.1. Domain definition

The use of a discretized domain allow the use of a monodimensional model which could be a good compromise between calculation effort and accuracy. The domain adopted suite very well with hairpin geometry inside the slot. Starting from the previous model proposed it is possible to make some considerations and modifying slightly it. Assuming that the slot geometry is rectangular as usually designed with hairpin winding, the slot domain can be discretized in k layers where each k hairpin legs are placed as shown in Fig.5.1, which represent an simplified scenario present in the slot within hairpin winding, cylindrical

coordinates has been assumed. The magnetic field produced by the current flowing in the conductors is considered parallel to their larger dimension W_{ck} , thus the field component parallel to the shorter conductors' dimension h_c is neglected.

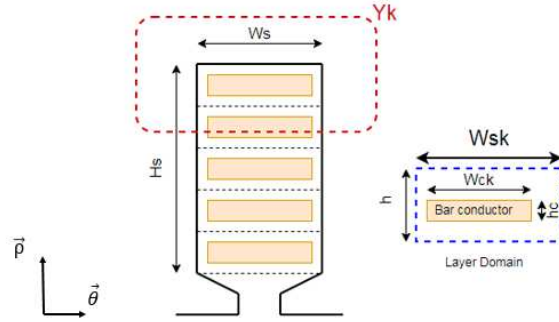


Fig. 5.1. Discretized domain.

5.1.2. Model Definition

This model is the one used in paragraph 4.1.1 adapted for the rectangular slots with rectangular cross section conductors. To simplify the problem without losing too much accuracy some hypothesis are needed, as following:

- 1) the ferromagnetic with infinite relative permeability,
- 2) saturation is neglected;
- 3) the end effects are neglected;
- 4) the magnetic field in the slot is constant along the tangential direction;
- 5) sinusoidal currents feed the conductors.

With these hypothesis a monodimensional model is possible to implement. Considering the red circuit Y_k it is possible to apply Ampere's law along it in order to obtain eq.5.1

$$H w_{sk} = \int_{y_{k-1}}^{y_k} -J_k w_{ck} dr + I_{k-1} \quad (5.1)$$

Where:

H is the magnetic field strength;

J_k is the current density in the k -th layer;

y_{k-1} and y_k are the $(k-1)$ -th and k -th layers position;

I_{k-1} is the total current linking the first $(k-1)$ layers.

Once defined I_z as the current flowing in the hairpin conductors, the current I_{k-1} through the eq. 5.2

$$I_{k-1} = \sum_0^{k-1} I_z \quad (5.2)$$

Starting from the eq.5.1 it is possible to obtain partial differential equation such as eq.5.3 and applying Faraday's law to the circuit in red the eq.5.4 is immediate.

$$\frac{\delta H}{\delta r} = \frac{-J_k w_{ck}}{w_{sk}} \quad (5.3)$$

$$\frac{\delta J}{\delta r} = -\mu \sigma \frac{\delta H}{\delta t} = -j \omega \mu \sigma H \quad (5.4)$$

The supply electric pulsation is represented by ω , while μ and σ are the magnetic permeability and the electric conductivity of the conductive material, respectively.

The combination of (5.3) and (5.4) results in the final expression in (5.5), whose general solution is provided in (5.6). Here, p is as defined in (5.7), where δ is the skin depth reported in (5.8).

$$\frac{\delta^2 H}{\delta r^2} - \frac{j \omega \mu w_{ck}}{w_{sk}} H = 0 \quad (5.5)$$

$$H = A_1 e^{-pr} + A_2 e^{pr} \quad (5.6)$$

$$p = \frac{1+j}{\delta} \quad (5.7)$$

$$\delta = \sqrt{\frac{w_{sk}^2}{w_{ck} \omega \mu \sigma}} \quad (5.8)$$

The constant terms A_1, A_2 are found through the boundary conditions (5.9) and (5.10), where h is the height of the considered layer.

$$H = \frac{I_{k-1}}{w_{sk}} ; r = 0 \quad (5.9)$$

$$H = \frac{I_k}{w_{sk}} ; r = h \quad (5.10)$$

The current density in the k-th layer is finally obtained as in (5.11), whereas the associated losses are determined as in (5.12).

$$J_k = - \frac{I_k p \cosh(p r) - I_{k-1} p \cosh(p h - p r)}{w_{sk} \sinh(p h)} ; r \in [0, h] \quad (5.11)$$

Thanks to the Ohm's law it is possible to have the losses value in each layer as in eq.5.12.

$$P_k = \iiint_0^{vol} \frac{J_k^2}{\sigma} dv = lck w_{ck} \int_0^h \frac{J_k^2}{\sigma} dr ; r \in [0, h] \quad (5.12)$$

5.1.3. Theoretical Case studies

The case under analysis is a stator designed for a traction application presented in chapter 3. Different stator topologies with different hairpin winding configurations have been considered. The stator yoke material is M270-35A SiFe lamination, whereas the hairpin material is pure copper. In this particular study, three different slot topologies are analysed with 2,3 and 4 slots per pole per phases q . To have a fair comparison between these cases, the same inner and outer stator diameter is considered. Ideally with the hairpin winding is possible to achieve a slot fill factor equal to 1, in first instance this value has been considered. In these conditions, varying q implies varying the width of the various hairpin legs. In addition, the sensitivity study involves changing the number of layers k from 2 to 8, obviously excluding the odd numbers. In this analysis the same magneto motive force is kept constant for all configurations, all conductors of each phase are connected in series and the current value has been choose to have the magneto motive force equal to 120 ampere turns (at peak condition the motor has been designed to have 2400 ampere turns as per chapter 3) the voltage constraints and motor performances are out of the scope of

this study which is to understand how some hairpin geometrical parameter could influence the copper losses once chosen the stator geometry and the hairpin winding configuration. A summary of the slot and conductors' dimensions is provided in Table 5.1 for all the envisioned combinations, the layer is the space filled by a single conductor, the definition 4 layer i.e. means that there are 4 conductors into the slot. In Fig.5.2 a sketch of the three stator angular sectors 2,3 and 4 number of slot per pole per phase is shown, where all three phases are modelled with solid conductors. For the sake of the simplicity in modelling, it was not considered the scenario where two different phases are placed in the same slot typical for the shorted pitch winding.

TABLE 5.1: SLOT AND CONDUCTOR GEOMETRICAL PARAMETERS

Description	Value(mm)		
	q=2	q=3	q=4
Slot height	24	24	24
Slot width	8.8	5.8	4.3
Copper height(8layer)	3	3	3
Copper width (8layer)	8.8	5.8	4.3
Copper height(6layer)	4	4	4
Copper width (6layer)	8.8	5.8	4.3
Copper height(4layer)	6	6	6
Copper height(4layer)	8.8	5.8	4.3
Copper height(2layer)	12	12	12
Copper width (2layer)	8.8	5.8	4.3

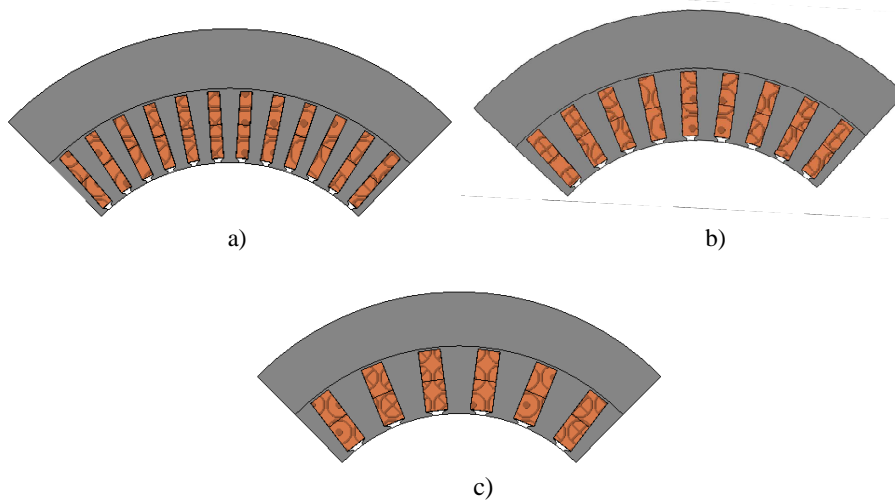


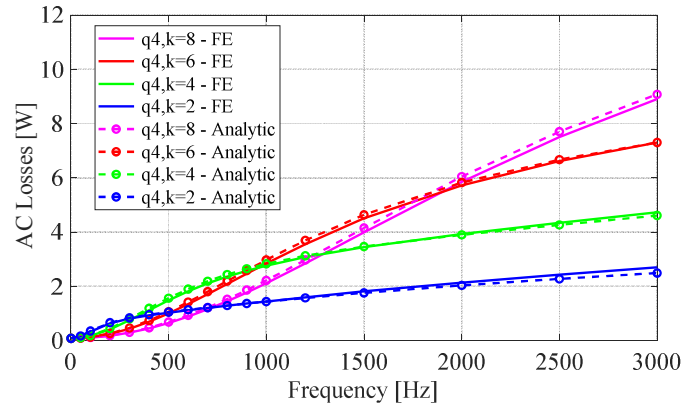
FIG.5.2. Stator angular sectors built and analyzed in the FE models for a) q=4; b) q=3; c) q=2.

5.1.4. Analytical vs FE Results

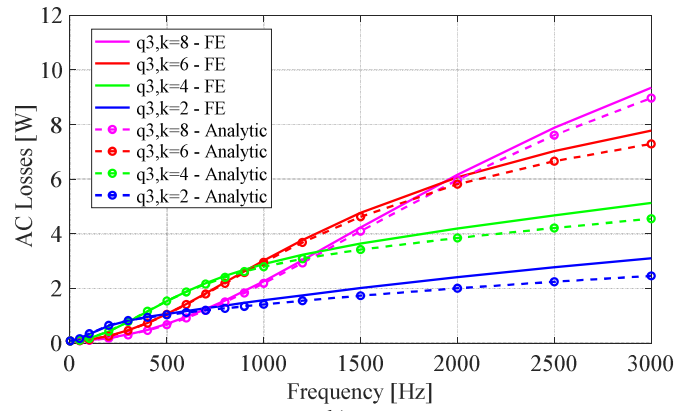
In this section we are going to validate the analytic model via FE in order to have a feeling about its limits and accuracy as well. The analysis is carried out at several frequency values, ranging from 0 Hz to 3 kHz for all the cases under analysis. It is reasonable to predict that as much higher is the ratio between slot width and slot height as much accurate is the monodimensional model being the scenario closer to the hypothesis. In Fig. 5.3 for the various combinations resulting from changing q and k , once the stator inner and outer radius are constant.

The case study with $q=4$ (Fig.5.3a) registers the best accuracy for the analytical model, with a maximum error of 7% obtained at 3 kHz and with $k=2$. It can be also noticed that the match is excellent up to 2.5 kHz for any k value. With $q=3$ (Fig. 5.3b) the discrepancies between the methods increase and become more and more evident above 1 kHz. The lowest accuracy is achieved for the stator with $q=2$ (Fig. 5.3c), with a 45% as a maximum error at 3 kHz and with $k=2$. An acceptable match is achieved below 500 Hz, while above such frequency value the analytical method is rather inaccurate. In general, it can be noticed that the lower the number of layers, the lower the accuracy of the 1D analytical model. Taking as example the case study $q=2$, the error at 3 kHz goes from 18% to 45% ranging from 8 to 2 layers.

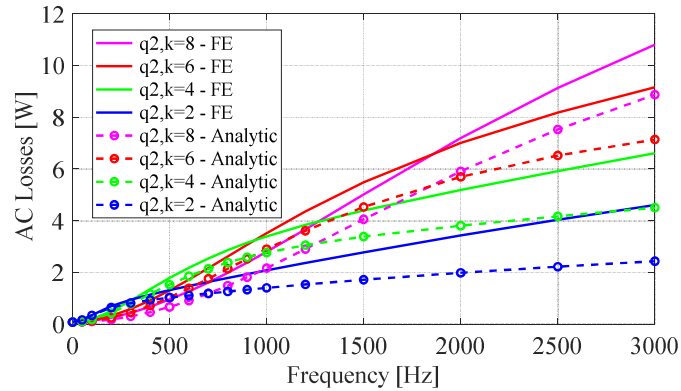
It can be concluded that, after a certain frequency range, the analytical model is not able to accurately predict the AC losses, due to the complexity of the phenomena. Under specific geometrical conditions, such as $q=2$ and/or $k=2$, the analytical prediction inaccuracy is even more emphasized. Therefore, for the sake of the sensitivity analysis discussed in this work, the FE model is used to extract useful design recommendations and guidelines that will be provided in the next section.



a)



b)



c)

FIG.5.3. Comparison between analytical and FE models used to evaluate the Stator Angular Sector AC losses: a) $q=4$; b) $q=3$; c) $q=2$.

5.2. Number of layer influence to the total AC losses

According to the analysis done in paragraph 5.4.1, once the stator outer and inner radius has been fixed, the copper losses, are affected by the design parameters such as: number of slots-per-pole-per-phase and the number of layers. At design stage, the stator is sized in order to satisfy the requirements needed to match the specifications. Once, defined the stator and the slot geometry the only degree of freedom to reduce the copper losses is the choice of the number of hairpin layers to insert in each slot. This parameter defines the bar height which influence the copper losses in the winding. Hairpin winding topology permit to have a perfect transposition [73] and to null the relative losses component due to the circulating current, but, the contribute due to the skin and proximity effect are still present and they are dependent to the bar cross-section and the frequency. For this reason, a particular attention has been paid to the number of layers. . In Table 5.2, 5.3 and 5.4, the influence of the number of layers on the total losses is evaluated for different q values, ranging from 0 Hz to 3 kHz. The minimum loss values are shown and underlined in red.

TABLE 5.2: BEST WINDING SOLUTION FOR STATOR WITH Q=4

<i>Frequency</i> (Hz)	<i>AC Losses [W]</i>			
	<i>2_layer</i>	<i>4_Layer</i>	<i>6_Layer</i>	<i>8_Layer</i>
100	0.332	0.172	0.124	<u>0.107</u>
500	1.028	1.485	1.000	<u>0.650</u>
1000	<u>1.443</u>	2.763	2.840	2.115
1500	<u>1.809</u>	3.444	4.500	3.984
2000	<u>2.135</u>	3.923	5.725	5.849
2500	<u>2.429</u>	4.337	6.617	7.505
3000	<u>2.700</u>	4.727	7.300	8.903

TABLE 5.3: BEST WINDING SOLUTION FOR STATOR WITH Q=3

<i>Frequency</i> (Hz)	<i>AC Losses [W]</i>			
	<i>2_layer</i>	<i>4_Layer</i>	<i>6_Layer</i>	<i>8_Layer</i>
100	0.336	0.175	0.128	<u>0.108</u>
500	1.073	1.542	1.069	<u>0.705</u>
1000	<u>1.570</u>	2.894	3.022	2.268
1500	<u>2.014</u>	3.646	4.773	4.228
2000	<u>2.411</u>	4.195	6.074	6.169
2500	<u>2.774</u>	4.678	7.035	7.890
3000	<u>3.111</u>	5.135	7.785	9.345

TABLE 5.4: BEST WINDING SOLUTION FOR STATOR WITH Q=2

Frequency (Hz)	AC Losses [W]			
	2_layer	4_Layer	6_Layer	8_Layer
100	0.353	0.193	0.144	0.127
500	1.311	1.786	1.308	0.955
1000	2.082	3.396	3.512	2.797
1500	2.780	4.393	5.483	5.008
2000	3.425	5.187	7.002	7.185
2500	4.031	5.912	8.183	9.132
3000	4.605	6.606	9.153	10.805

The tables above highlight that above a certain frequency value adopting the solution with less layers bring more benefits in term of losses. This statement is partly contradictory with what is usually found in literature, i.e., the losses can be reduced by decreasing the conductors' height. The reason behind this statement is that reducing the bar height give benefits in term of skin contribution until a certain frequency value. For example, if we consider the scenario with 2 and 8 layers, where the bar height is 12 and 3 mm respectively, according eq. 5.8, with the first value we limit the skin effect until 30 Hz instead with the second one until 488 Hz, up this value a thinner bar is needed. Starting from this consideration we note that above 488Hz the bar height does not give any contribute for the skin effect, in addition as per Fig.5.4 the proximity effect become predominant. Fig.5.5 demonstrate that in all conductors being in series flow the same current.

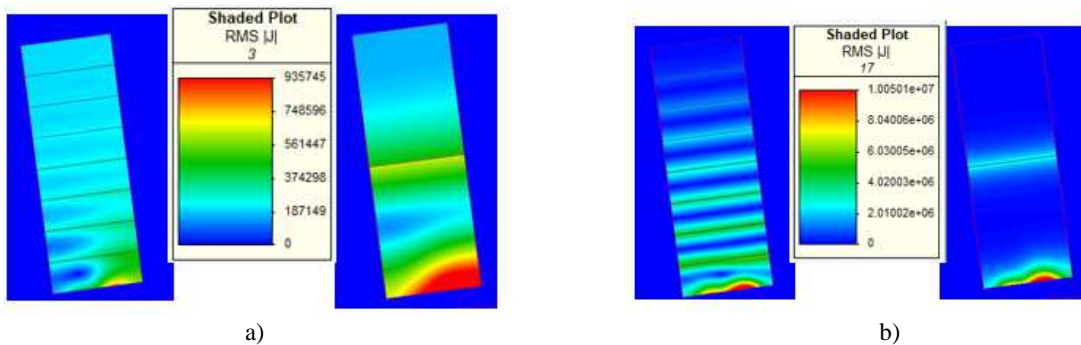
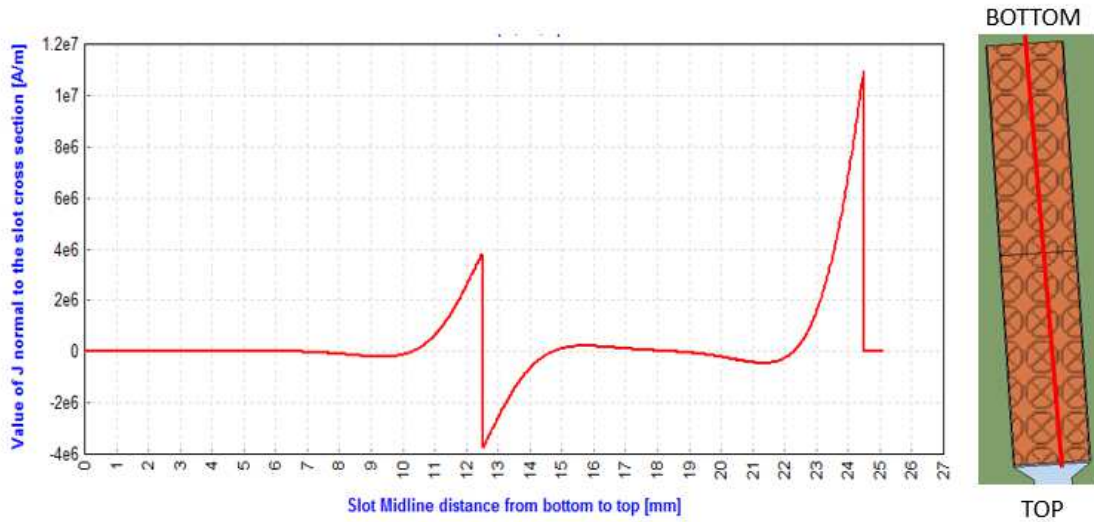
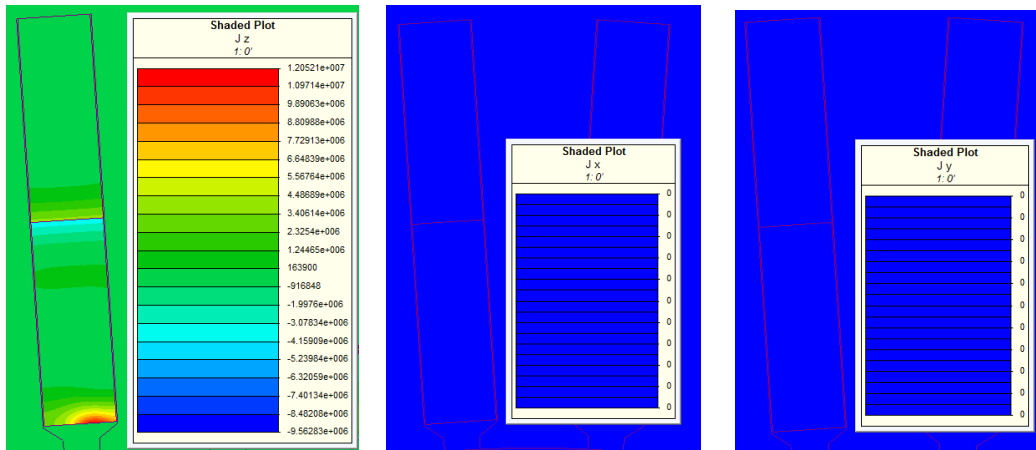


Fig. 5.4. Current density (A/m²) distribution for stators with q=2, k=8 and k=2 at a) 100 Hz and b) 3 kHz.



a)



b)

Fig. 5.5: a) Current density distribution (A/m²) in normal direction across the red line from the bottom until the top of the slot ; b) Current density distribution in the three directions

In Table 5.5 it is shown, for all winding configurations under analysis, the frequency value with the skin depth equal to the bar height. Therefore, this strategy of adopting a thinner bar is effective in terms of P_{skin} reduction up to a maximum frequency limit. Above this frequency limit, P_{prox} becomes the highest contributor to P_{AC} .

The analysis presented here suggests that the number of conductors within the slot, besides defining the voltage and magnetomotive force levels of the machine at hand, can

play an importance role in reducing the AC losses in hairpin windings. In light of this and of the results presented in Table 5.2, 5.3 and 5.4, depending on the operating frequency range, a suitable choice of the number of layers can improve the overall performance of electrical machines equipping hairpin conductors.

TABLE 5.5: RELATION BETWEEN SKIN DEPTH AND CONDUCTOR SIZE

WINDING CONFIGURATION	BAR HEIGHT(MM)	FREQUENCY WITH SKIN DEPTH EQUAL TO THE BAR HEIGHT (Hz)
2 LAYERS	12	30
4 LAYERS	6	122
6 LAYERS	4	274
8 LAYERS	3	488

5.3. Fill factor influence to the total AC losses

At design stage, the trend is to maximize the copper slot fill factor in order to reduce the DC losses and increase the current density. Operating in high frequency, it could be interesting analyze how the losses changes with the slot fill factor. In first instance, we can assume that adopting lower fill factor the current density constraint is still satisfied.

Two different solutions could be adopted:

- 1) When the voltage value is constrained by the application does not give much flexibility in the number of turns, the height of the bars can be reduced and the conductors are moved farer from the slot opening, as in its proximity the high frequency phenomena are more evident. This method is schematized in Fig. 5.6, where basically the fill factor is reduced from 1 to 0.5, always maintaining the same slot height. For simplicity, only the case with $q=4$ and $k=4$ is presented, as similar conclusions can be drawn for the cases where different values of q and k are considered.

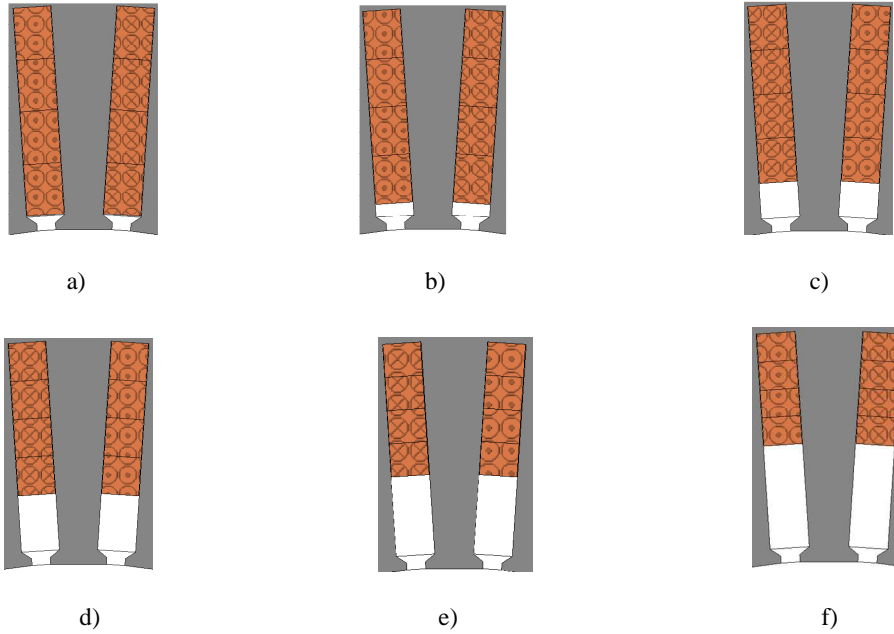


FIG.5.6. Stator with $q=4$ and $k=4$ with different slot fill factors: a) 1; b) 0.90; c) 0.8; d) 0.7; e) 0.6; f) 0.5.

2) When the voltage is not constrained by the application permit to reduce the number of turns, it is possible to think to remove the closest conductors to the slot opening, reducing also the slot fill factor to 0.5. This method is schematized in Fig.5.7, where 2 conductors are removed from the original case study, i.e., $k=4$.

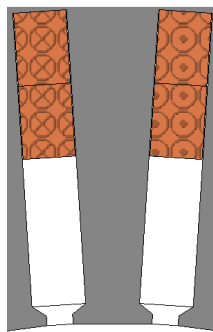


Fig. 5.7. Stator with $q=4$ and $k=2$ with same cross section of $k=4$ (originally with $k=4$ and 2 conductors closest to the slot opening zone removed).

For a fair comparison, the magnetomotive force is kept the same as the case with the slot fill factor is 1 and the copper losses has been evaluated reducing gradually the fill factor up to 0.5 with steps equal to 0.1 as shown in Fig.5.6. Only the case with $q=4$ and $k=4$ Is

considered, the same concept can be repeated to the other topologies being the idea behind the same. In Fig.5.8 it is shown the influence of the slot fill factor to the copper losses, the copper losses are referred to the model simulated which is a portion of the entire model as per Fig. 5.2 supplied with a 120 ampere per turns .

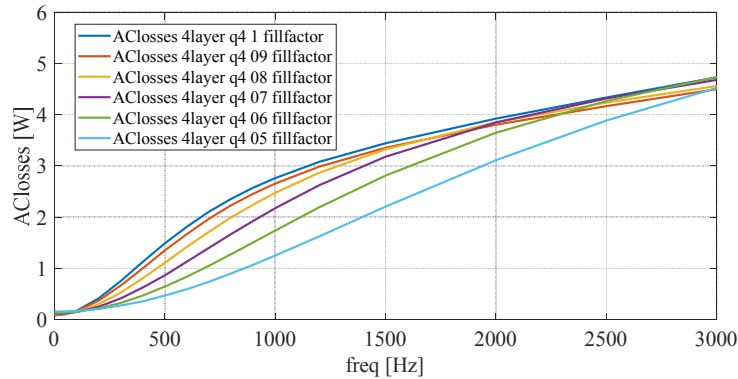


Fig. 5.8 AC losses for the case study with q=4 and k=4, with variable slot fill factors.

The losses reduction could be significant with this strategy. In Fig.5.9, the percentage loss reduction achieved using lower fill factor values than 1 is illustrated. Considering the best scenario, i.e. fill factor equal to 0.5, from 200 Hz to 1.3 kHz the loss reduction is always larger than 40%, and reaches $\approx 70\%$ at ≈ 500 Hz.

In Fig.5.10, it is shown how the removal of the closest conductors to the slot opening could be an effective strategy to reduce AC losses. While this interesting result can be used as a design guideline in hairpin windings, the negative effects of such technique on the torque capability need to be also considered.

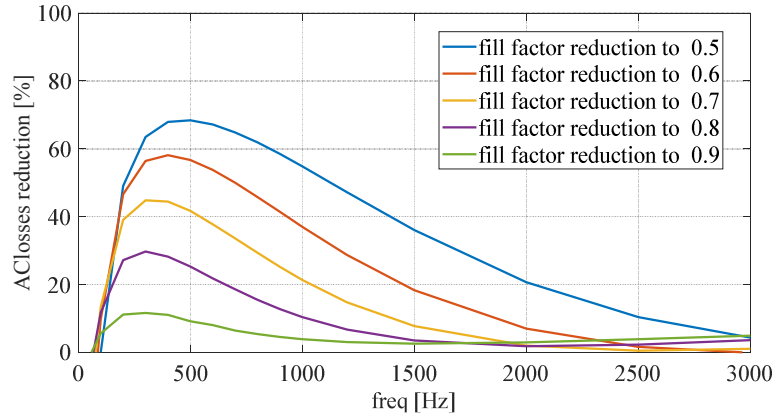


Fig. 5.9. Percentage loss reduction with respect to the case with fill factor equal to 1.

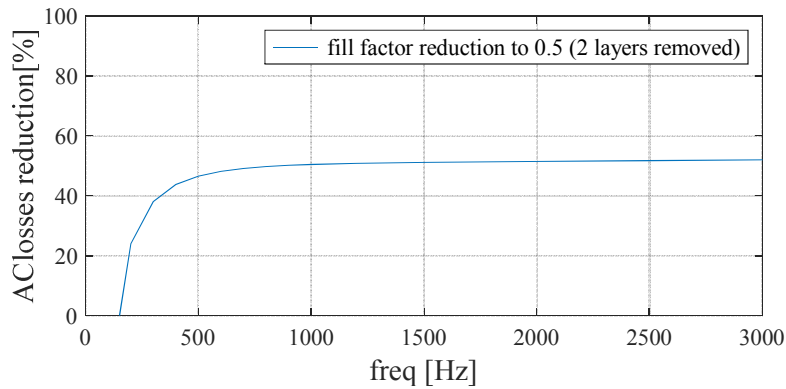


Fig. 5.10. Percentage loss reduction achieved by removing the closest conductors to the slot opening.

5.4. Conclusion

The focus of this chapter was to provide an analytical model useful to describe the losses inside the hairpin winding during high frequency operative points. A monodimensional model was presented and implemented to validate it via FE. However, under specific geometrical and operating conditions (i.e., with low number of slots-per-pole-per-phase and with very high operating frequencies), the model was deemed to be rather inaccurate (as opposed to a finite-element approach) for investigating the AC losses' sensitivity to some design parameters, which is the main objective of this work. It is important to make clear that in this study was not be considered the effect of the mentioned parameters to the power capability, especially to the torque. Further investigations are needed to do in future works.

In particular, taking as case study a stator designed for an automotive application, the variation of losses against the following design parameters was analysed:

- 1) The number of slots-per-pole-per-phase q , which in turn results in a modification of the conductors' width. The findings showed that a too low q value produces higher losses, although in general its variation does not lead to significant benefits.
- 2) The number of layers-per-slot k , which in turn results in a modification of the conductors' height. Although the findings showed that increasing k can lead to a significant AC loss reduction up to a certain frequency range, i.e., ≈ 500 Hz, a lower number of layers can be a very effective means to reduce losses at high frequency values due to the reduction of the contribution brought from the proximity effect.
- 3) The fill factor, which in turn means either reducing the number of conductors within the slot or decreasing their height. Both strategies showed a significant effectiveness. However, the fill factor reduction should be carefully evaluated against the torque capabilities of the machine.

Chapter 6

Proposed Hairpin Topology to Improve Performance at High Frequency

In the last few years, the focus of several researches has been on ways to model, estimate and reduce AC losses in hairpins. In [89], guidelines on how to make suitable connections for reduced losses have been provided, along with a 1D model for the evaluation of copper losses. In [90], a 2D analytical model has been proposed and validated via finite element analysis (FEA). Methods such as removing the closest conductor to the slot opening or reducing the conductors' height while increasing the number of conductors have been proposed to reduce AC losses [91]. However, the first solution reduces the fill factor since part of the slot is left empty [92], whereas the second option increases the manufacturing complexity [89]. Asymmetric windings consisting of series-connected conductors featuring different cross-sections have been studied via FEA in [93]. Here, promising results have been achieved, but an experimental validation is missing. In addition, the method increases the DC resistance of the asymmetric conductors and may represent a limit to the maximum obtainable current density.

Another interesting technique to reduce AC losses in hairpin windings comes from the "strand" concept typical of random windings, where the conductor is divided in several parallel-connected sub-conductors (strands). In hairpins, this method cannot be applied as flexibly as in random windings. The number of parallel-connected elements should be kept low to avoid unfeasible solutions or excessive complications of the bending and welding processes [94]. Although the concept of parallel conductors has been widely implemented in large power machines equipped with pre-formed winding [95], to the of the authors' knowledge the parallel-connected concept in hairpin windings has been

proposed in [96], but the analysis only focused on the 2D aspects (i.e. end-windings effects are neglected) and no experimental validation was provided.

This work fills these gaps by including the 3D effects in both analytical and FE models and, most importantly, by experimentally validating the segmented hairpin concept. In particular, concerning the modelling aspects, a simplified 2D FE model is proposed for the analysis of the end regions, yet taking into account the phenomena potentially occurring at high frequencies. Regarding the experimental validation, a segmented hairpin winding is implemented onto purposely-built motorettes. Four motorettes are prototyped and tested, each of them equipped with different winding arrangements for comparative analyses. Besides proving the benefits of the proposed technique in terms of loss reduction, the experimental results are used to demonstrate that the segmented hairpin winding can compete against random windings even at high frequency operations. This is done by comparing these results to those obtained in [96] on motorettes equipped with round wire random windings.

6.1. Introduction to the Proposed Concept

In this work a stator designed for a traction machine, presented in chapter 3, with 160 kW peak power and 19 krpm maximum speed is took as reference. For this application the permanent magnet synchronous reluctance has been selected as the most suitable machine topology. To increase the torque density a 3 rotor barriers per pole, as shown in Fig 6.1, and the geometrical parameters are provided in Table 6.1.

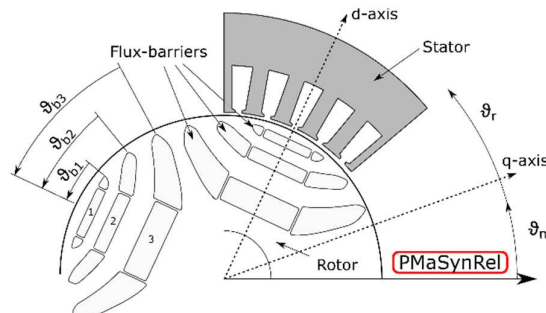


Fig. 6.11. Permanent Magnet assisted SynRel motor sketch.

TABLE 6.1: MOTOR GEOMETRICAL PARAMETERS

Name	Description
ϑ_{b1}	Flux barrier angle 1
ϑ_{b2}	Flux barrier angle 2
ϑ_{b3}	Flux barrier angle 3
W_{so}	Slot opening width
h_s	Slot height
W_{pmi}	Permanent Magnet width
h_{pmi}	Permanent Magnet height

Two different stators has been considered with two different numbers of slots-per-pole-per-phase q are envisioned (i.e. $q=2$ and $q=4$), while fixing stator inner and outer diameters and different number of conductors per slot. It has been associated the name layer k the space occupied by a single conductor. The following layouts are considered: 1) $q=2$ and $k=4$; 2) $q=4$ and $k=8$; 3) $q=4$ and $k=4$ 4) $q=4$ and $k=6$. In Table 6.2 and Table 6.3 the stator and conductors' dimensions are given respectively. In Annex 2 the winding connections for each layout, via finite element has been calculate the circulating current to be sure that it is equal to zero for the 4 layout presented.

TABLE 6.2: MOTORETTE GEOMETRICAL PARAMETERS

Description	Value(mm)	
	$q=2$	$q=4$
Stator Inner Radius	70	
Stator Outer Radius	111	
Stack length	92	
Slot width	9.1	4.4
Slot height	23	20

TABLE 6.3: BAR CROSS SECTION PARAMETERS

Description	Value(mm)	
	width	height
Layout 1): $q=2, k=4$	8.2	4.3
Layout 2): $q=4, k=8$	4	1.75
Layout 3): $q=4, k=4$	4	3.5
Layout 4): $q=4, k=4$ ($k=4$ segmented)	4	1.75

The layout 4) represent the proposed hairpin concept called "segmented hairpin". It consist in splitting some of the conductors in two or more layers. This topology is electrically identical to the 3), with the same equivalent conductors is series. This concept can be extended to any hairpin winding configuration (i.e. different number of layers or different parallel paths), and does not impact the equivalent number of turns per phase but only splits one or more conductors in two or more smaller parallel-connected conductors, with the aim of reducing the AC copper losses. In Fig.6.2 is explained the proposed concept, in Fig.6.2a the conventional solution corresponding to option 3) is modified by segmenting the two closest conductors to the slot opening in two sub-layers having identical cross sections. This modified layout is named "proposed solution" in Fig. 6.2a and corresponds to the aforementioned option 4), where the number of conductors is series per slot is four. For this reason, this layout can be labelled with "k=4 segmented", as seen in Table 6.3. Thanks to Table 6.3 we can note that both solutions have the same fill factor, the segmented layers result placed nearer to the slot opening zone because the physical gap needed between the layers. The electrical connections of the segmented hairpin winding are shown in Fig.6.2b, where each of the last two conductors (namely 3 and 4) are subdivided in two sub-layers (3.1 and 3.2, and 4.1 and 4.2), whereas in Fig.6.2c the connections typical of a standard hairpin layout are illustrated to highlight the major differences.

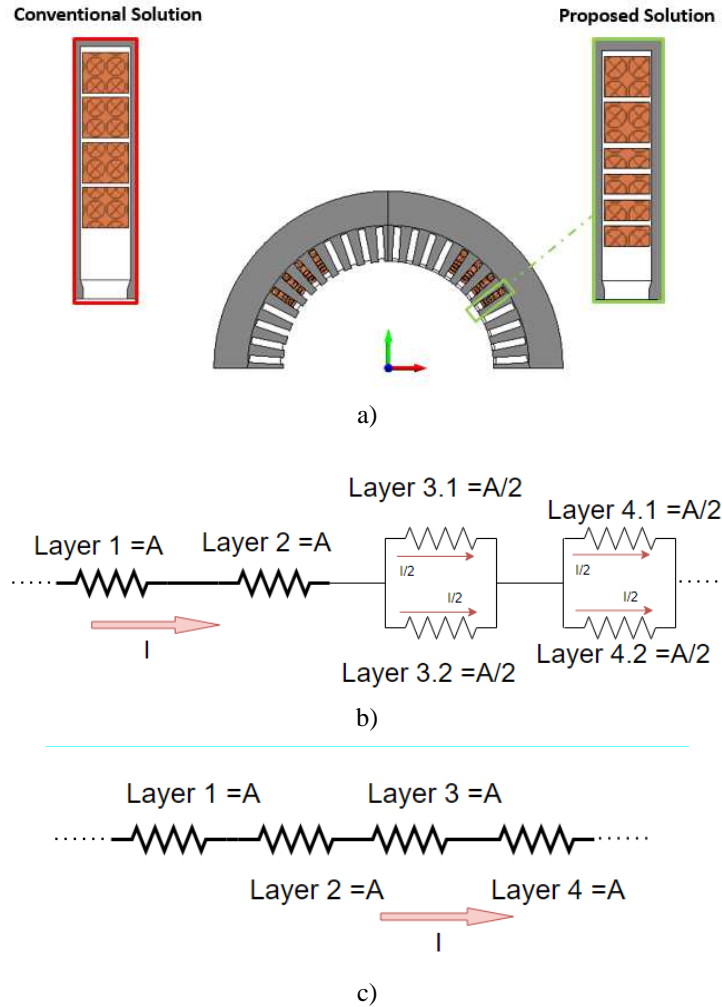


Fig. 6.2. a) the proposed segmented hairpin concept and b) circuitual schematic; c) conventional hairpin circuitual schematic

6.1.1. Manufacturing aspect of the Hairpin Topology

The concept proposed is limited by the manufacturing process. In theory each hairpin leg can be splitted in two subconductors connected in parallel. This way to proceed increase the manufacturing process and costs, the segmentation is needed to limit based to the best trade off in term of benefits and costs. Each layer segmented bring additional complexity because the welding points increase and being the number of layers higher a particular attention is needed to pay to the transposition to avoid circulating current.

The slot opening zone is the most critical in term of losses, in this work the choice to split only the last layer has been done to have the best trade of between losses reduction and manufacturing impact.

The hairpin winding is becoming more and more used in mass production thanks to its process that could be fully automated. The actual manufacturing process limit the the number of conductors possible to insert into the slot. This limitation is due to the constraints related to the hairpins' width-to-height ratio during the bending process because of the tooling used to bend and twist them. Thanks to the technology progress in hairpin manufacturing lines, the segmented hairpin winding will not have a significant impact on the manufacturing process and cost. During the AUTO-MEA [97], a Clean Sky 2 project a novel methodology has been realized to deliver innovative and flexible coil fabrication system, which can provide programmable 3D formed coil shapes suitable for high frequency operation, effective coil insertion and automated welding strategies to form a complete winding system for aerospace and automotive wound components. The technology proposed is able to make the segmented hairpin with a full automated process, this has not been discussed in this thesis because out of scope.

6.2. Analytical Calculation

To exploit the benefits of the proposed methodology vs. conventional ones, a 1D analytical model for AC loss estimation is developed and described in this section.

AC losses are those occurring above the frequency level where the current is no longer uniformly distributed within the conductors. These losses are mostly due to skin and proximity effects, assuming that circulating currents are zeroed by a suitable transposition. Usually, the AC losses P_{AC} are quantified through the product of DC losses and a non-dimensional factor K_{AC} , which is defined in (6.1). The DC loss P_{DC} is found through the simple relationship reported in (6.2), where l_c and A_c are respectively the conductor length and its cross section, while σ is the electric conductivity of the material. When skin and proximity effects occur, the cross section where the current flows is a fraction of A_c , thus

the equivalent resistance (namely the AC resistance) increases and AC losses are consequently enhanced by the factor K_{AC} .

$$K_{AC} = \frac{P_{AC}}{P_{DC}} \quad (6.1)$$

$$P_{DC} = R_{DC} I^2 = \frac{l_c}{\sigma A_c} I^2 \quad (6.2)$$

These high-frequency phenomena can be significant especially in the slot region, but they may have some influence also in the end-winding regions. Hence, for the slot region the model already presented in Chapter 5 has been adopted and for the end-winding region a dedicated model has been developed to predict the high frequency copper losses.

6.2.1. End Winding Region Model Simplification

In the end-winding region, the model described above cannot be directly used since the ferromagnetic material surrounding the conductors is no longer present and the geometry of the end-windings is rather complex. However, since the end-windings are basically surrounded by air, the leakage magnetic field magnitude is much lower than the slot region as mentioned in [98]. According also with [38] introduced in paragraph 2.6, it becomes then reasonable to neglect the proximity effect [99], meaning that the only contribution to AC losses is due to the skin effect. As a first approximation, the skin effect can be considered invariant along the direction of the conductor length, thus leading to tackle the loss determination problem as a 1D one also in the end-winding region. Equation (6.3) is then used for determining the skin effect resistance R_{skin} [100], which depends on the parameter ξ the expression of which is provided in (6.4).

$$R_{skin} = \frac{R_{DC}}{2} \xi \frac{\sinh(\xi) + \sin(\xi)}{\cosh(\xi) - \cos(\xi)} \quad (6.3)$$

$$\xi = \frac{\sqrt{\pi}}{2} \frac{1}{\delta} \sqrt{\frac{W_{ck} h_c}{\pi}} \quad (6.4)$$

6.3. Finite Element Model

As per the analytical approach, FE models of both slot and end-winding regions are developed to evaluate the AC losses using MagNet® from Simcenter. For both regions, the solution mesh is defined according to a detailed sensitivity analysis aimed at finding the best trade-off between accuracy and computational effort. Time harmonic simulations are used for the sake of resolution speed and consistency with the sinusoidal supply assumption. According to the [101] only the stator model is needed to reduce the computational effort without losing accuracy in estimating the AC losses, being the latter mainly dependant on the slot flux leakage [96].

6.3.1. Slot Region Model

Contrarily to the analytical approach, for the slot region the FE models consist of 2 poles being analyzed for any of the 4 configurations introduced in 6.1. Only one phase and only the stator is modelled, as shown in Fig. 6.3 for one of the considered layouts, i.e. the case with $q=2$ and $k=4$.

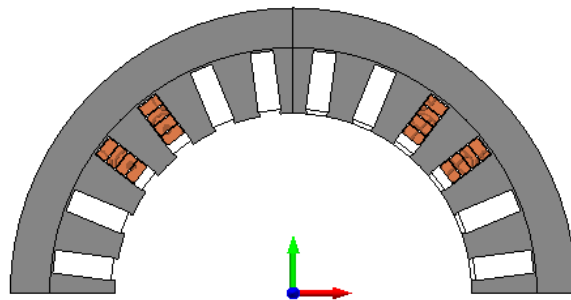


Fig. 6.3. FE slot region model for the case study with $q=2$ and $k=4$.

6.3.2. Hypothesis for the End Winding Region Model

The estimation of AC losses in hairpin windings including the end-windings is an inherently 3D problem. Also, the end regions of hairpin windings are rather complex and only a 3D

analysis would be fully accurate. However, a 3D model would be very consuming in terms of both modeling and simulation times. To enable a 2D analysis, first of all the proximity effect is neglected and only the skin effect is taken into account, consistently to the analytical approach discussed in 6.2, as a consequence also the proximity effect coming from the conductors of the other two phases has been neglected as per hypothesis. To simplistically evaluate the influence of the end-winding geometries, two conductors with different shapes are considered, as reported in Fig. 6.4. The two conductors have identical cross sections and lengths, but the first one is obtained through axial extrusion (see Fig.6.4a), whereas the second one is extruded angularly (see Fig.6.4b). Apart from the major bends typical of hairpin windings, the conductor shown in Fig.6.4b reproduces a shape close approximation to the ones that can really be found in this region. This conductor is modelled through a 3D FEA, whereas the one shown in Fig.6.4a is studied as a 2D problem. The FE evaluations for both conductors' shapes are carried out at 1000 Hz to enhance the high frequency effects. The comparison is shown in Table 6.3 and highlights a 1.5% mismatch between the results in terms of losses. In Table 6.3, the number of mesh elements and the solution times are also reported to emphasize and justify the use of the 2D models for the analysis of the end-winding regions.

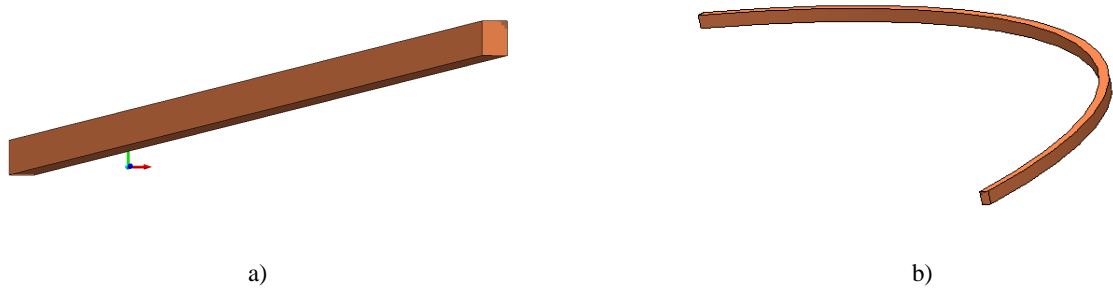


Fig.6.4. End Winding Region Models: a) Axially-extruded conductor (2D analysis) and b) Angularly-extruded conductor (3D analysis).

TABLE 6.4: COMPARISON AC LOSSES AT 1KHZ BETWEEN 2D AND 3D END WINDING MODELS

Model	Losses [mW]	Mesh Elements (units)	Computational Time (sec)
2D	5.15	226	6
3D	5.23	711358	67

Considering the above and passing to the analysis of the study cases at hand, it is worth mentioning that a full 3D CAD model is usually available for a hairpin winding design ready to be manufactured. Hence, it would be straightforward to determine cross sections and lengths of all conductors to use in the simplified 2D FE models. However, since motorettes are manually built to prove the concepts proposed in this thesis, a full 3D CAD model is not available. Therefore, to estimate the total end-winding length, it means the contribute of both sides, for the FE evaluations, first the overall DC resistance $R_{DC_{measured}}$ is measured with an impedance analyzer and then, knowing the winding characteristics in the slot region, it becomes possible to extract the 2D resistance $R_{DC_{2D}}$ and the end-winding resistance and length R_{end} and L_{end} . To such purposes, (6.5) and (6.6) are used, where σ_{cu} is the copper conductivity and A_{cu} is the conductor cross section

$$R_{end\ winding} = (R_{DC_{measured}} - R_{DC_{2D}}) \quad (6.5)$$

$$L_{end\ winding} = R_{end\ winding} \sigma_{cu} A_{cu} \quad (6.6)$$

In Table 6.5, the end-winding lengths of each side, assuming that both sides have the same length, calculated in this way are reported for each investigated case study. Finally, using such lengths, as previously assumed, it is possible to consider the conductor in the end winding zone not bended, that area can be modelled as per Fig.6.5. to estimate the AC losses in the end-winding region of each considered winding layout.

TABLE 6.5: CONDUCTOR END WINDING SIDE LENGTH

Winding Layout	End Winding Length [mm]
$q=2$ and $k=4$	285
$q=4$ and $k=4$	231
$q=4$ and $k=4$ Segmented	172
$q=4$ and $k=8$	144

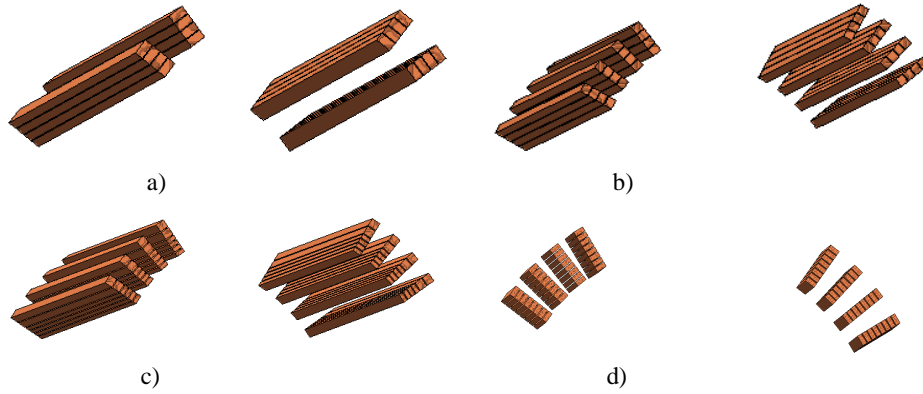


Fig. 6.5. End winding region model: a) $q=2$ and $k=4$; b) $q=4$ and $k=4$; c) $q=4$ and $k=4$ segmented; d) $q=4$ and $k=8$.

6.4. Comparison between Analytical and FE Results

In this section the results obtained with the analytical and FE models described above are presented and compared. These results aim to highlight the accuracy of the analytical model and the importance of including the end-winding effects in the evaluation of the overall AC losses even if some hypothesis has been introduced. The four layout (FE models) under analysis are fully explained in Annex 2.

6.4.1. Slot Region Model: Analytical vs FE results

The results obtained from the developed slot region analytical and FE models are compared in Fig.6.6, which shows the trend of the parameter K_{AC} (defined in (6.1)) vs. frequency. The analysis is carried out for a frequency range up to 1200 Hz for a better understanding of the losses behaviour of the studied topologies and for potential applications at higher speeds and/or frequencies. For the sake of clarity, the results relative to the four study cases have been split in Figures 6.6a and 6.6b. The match is very positive for all the conventional winding schemes, with a maximum error lower than 3% over the whole frequency range analyzed. Regarding the segmented layout, the error becomes $\approx 50\%$ at 1200 Hz (see Fig. 6.7b), since the analytical developed model does not take into account the updated boundary conditions resulting from such an unconventional arrangement [94]. On the other hand, both the analytical and FE results prove the

perceived benefits of the segmented layout, with a significant loss reduction achieved compared to the conventional $q=4, k=4$ configuration.

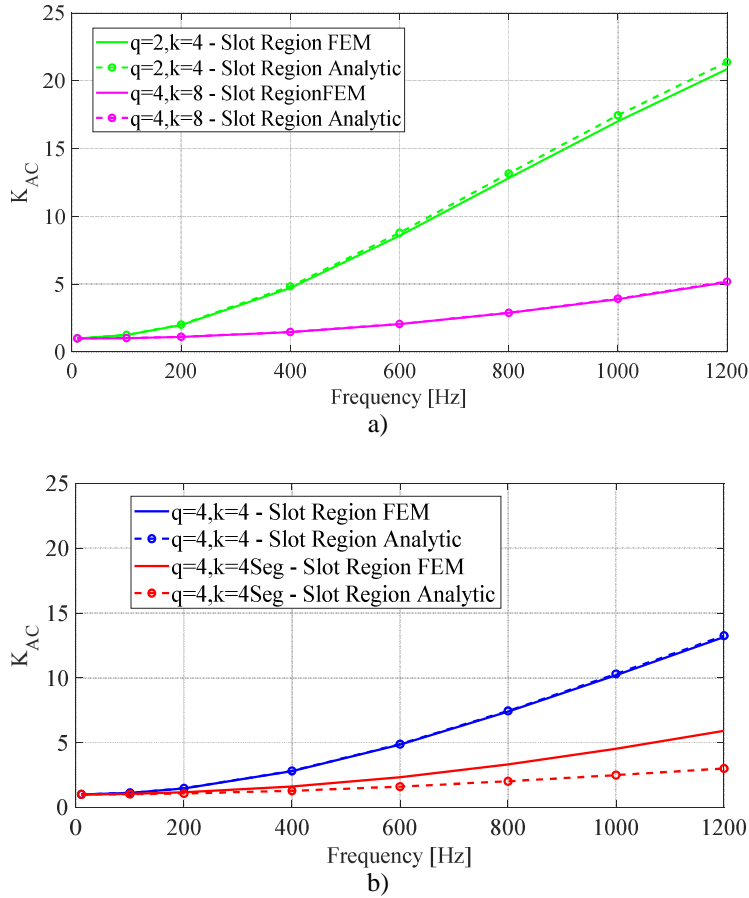


Fig.6.6. Slot region models: analytical vs. FE results -a) $q=2, k=4$ and $q=4, k=8$; b) $q=4, k=4$ and $q=4, k=4$ segmented.

Before introducing the results of the complete models, it is useful for the readers to give a feeling about the influence of the end winding regions. The Fig. 6.7 compare the FE results of the slot region and the complete model. Considering only the slot region without the contribute of the end winding the error could be high, in particular we have to note that the end winding region thanks to the hypothesis done, proximity effect neglected, reduce the K_{ac} factor of the total winding, this because the direct current losses in this region become predominant to the skin effect.

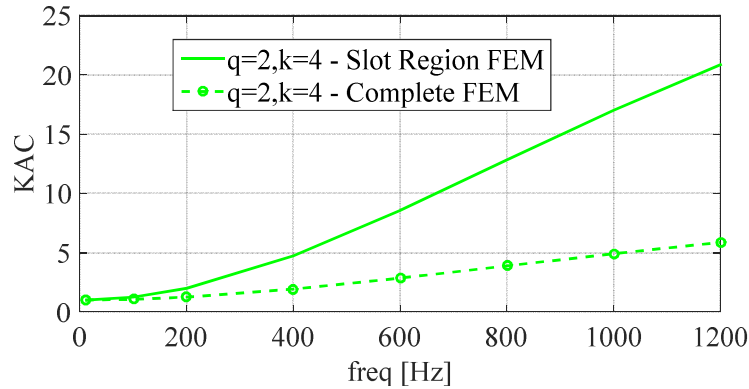


Fig.6.7. Comparison between results obtained with the slot region model and complete model for $q=2,k=4$.

6.4.2. Complete Analytical Model vs. Complete FE Model

To evaluate the effects of the end winding regions on AC losses, the FE results shown in the previous section (labelled as "Slot Region FEM") are compared against the complete FE model (labelled as "Complete FEM"), which includes both the contributions from the slot and end winding regions. The discrepancies can be very high, thus proving the need of an accurate end winding region model. The last comparison of this sensitivity study is carried out between analytical and FE models, when both include the overall effects (slot and end-winding regions) into account. The results are reported in Fig.6.8, where the segmented hairpin is not reported as the discrepancy would be excessive due to the reasons given in Section V.A. It can be noticed that the analytical model is not as accurate as in the slot region. For the study cases $q=4$ with $k=4$, $q=4$ with $k=8$ and $q=2$ with $k=4$ the maximum errors are 28%, 15% and 17%, respectively.

Despite these discrepancies, it is worth underlying again the need of including the 3D effects also in the analytical model. In fact, this is faster than the FE evaluations and this can lead designers and researchers to prefer the analytical approach in some specific cases (e.g. when long optimization processes are used), yet accepting the inherent limitations and inaccuracies.

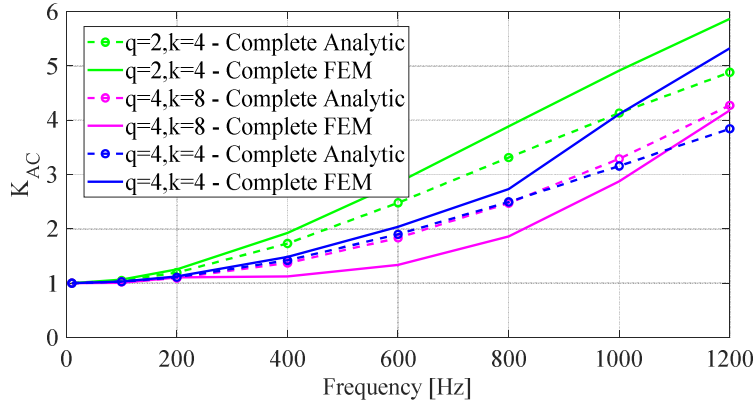


Fig.6.8. Complete analytical model vs. complete FE model: comparison of results relative to the investigated conventional arrangements.

6.6. Experimental Validation of the Proposed Concept

Aiming at demonstrating the proposed segmented concept as a means to reduce AC losses in hairpin windings, as well as to prove the methodologies presented in the previous section, four motorettes (i.e. stator portions corresponding to one pole pair) are built according to the dimensions provided in Tables 6.2 and 6.3. As mentioned in Section IV.B, these motorettes are manually wound for the sake of simplicity, i.e. to minimize costs, resulting in oversized end-windings. The motorettes are shown in Fig.6.9 and are representative of the four study cases investigated in this work. The motorette does not take into account about the rotor and other phases contributes, generally, according also with the work done in [102] the ac losses are due mainly to the slot leakage flux and the other contributes have a secondary weight. It is expected that the trends have been confirmed also with the full motor. Therefore, one of these implements the segmented hairpin winding concept, i.e. the one labelled as “q=4, k=4 Seg” in Fig.6.9. For the sake of consistency with the sinusoidal supply assumptions used in both analytical and FE evaluations, the signal feeding the motorettes is first produced by a SiC Voltage Pulse generator with 60 kHz switching frequency and, then, filtered by a low pass LC filter with

a cutoff frequency at 2 *kHz* to obtain an output signal as close as possible to a pure sinusoidal waveform, the CHROMA 61511 was not available in the laboratory.

The power loss is measured by a precision power analyzer (PPA 5530) and an oscilloscope is used to double check the losses value and the signal waveforms. All measurements are taken at the same temperature (20°C). and the winding temperatures are monitored with a thermal camera during testing. The whole test setup is shown in Fig.6.10a, whereas the relevant circuitual schematic is illustrated in Fig.6.10b. The experimental test has been performed at the UniMoRe laboratory.

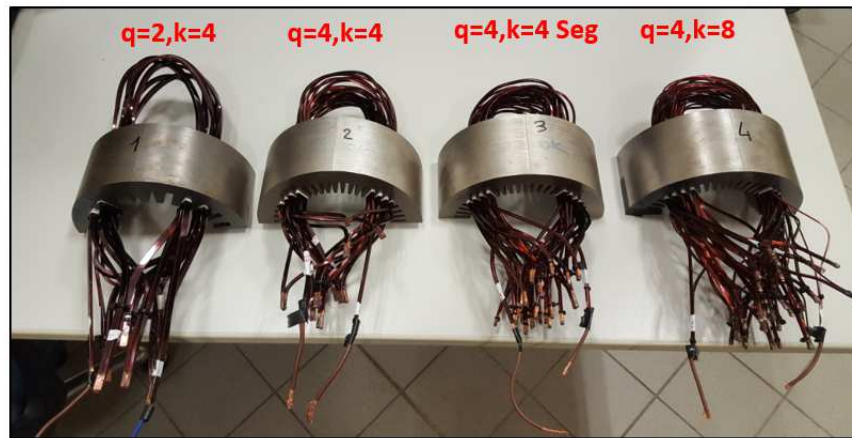
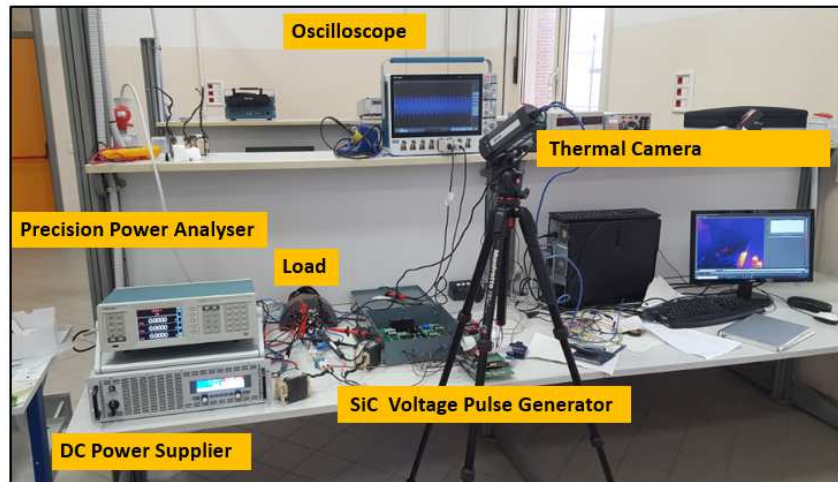
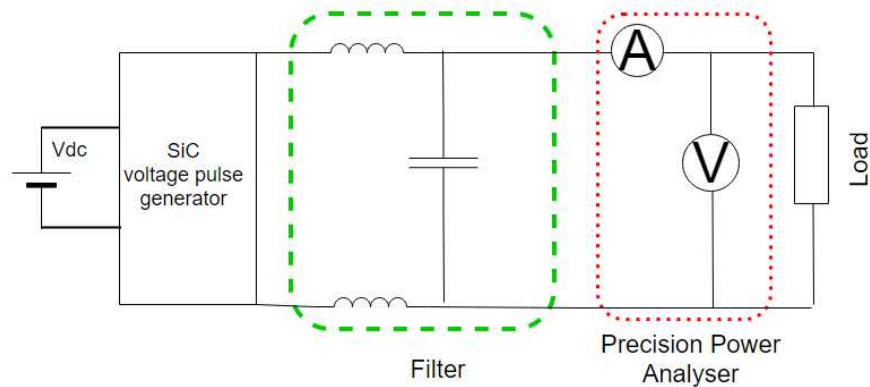


Fig.6.9. Built motorettes.



a)



b)

Fig. 6.10. Experimental layout : a) Experimental setup and b) corresponding circuitual schematic.

The experimental tests are performed ranging from 0 Hz to 1200 Hz and the relevant results are compared in terms of K_{AC} against the complete FE simulation results. This comparative exercise is reported in Fig.6.11, where an excellent match between FE and experimental results is achieved in the whole frequency range considered. The maximum error is less than 15% and this could be justified by the additional resistance introduced by the welded connections.

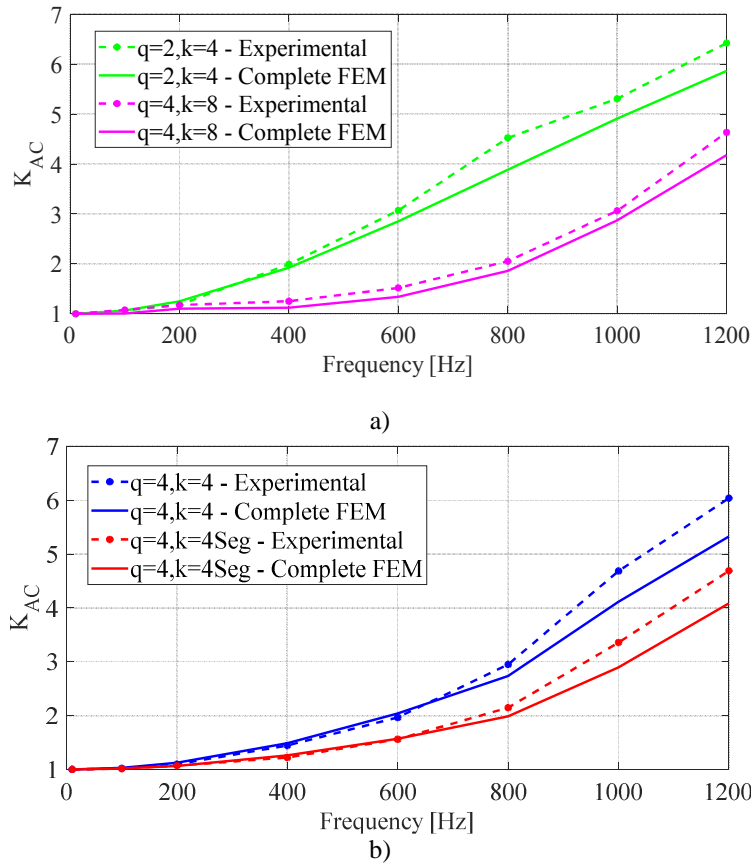


Fig. 6.11. Comparison between FE and experimental results: a) $q=2, k=4$ and $q=4, k=8$; b) $q=4, k=4$ and $q=4, k=4$ segmented.

Apart from the match accuracy between FE and experimental results, the main achievement here is the proof of the effectiveness of the segmented hairpin concept. Compared to the conventional $q=4, k=4$ layout, its modified segmented version, i.e. $q=4, k=4$ segmented, achieves an experimental loss reduction by more than 20% starting from 600 Hz, with a peak reduction of 28% registered at 1000 Hz. It is worth mentioning that, as done for the analytical and FE evaluations, the same magneto-motive force is used to feed the hairpin layouts to make the comparison fully fair.

Having proven the effectiveness of the proposed technique, the last step is to demonstrate that the segmented hairpin windings can compete against random windings envisioned for the same application. This is the focus of the next section.

6.7. Experimental Comparison Between Hairpin and Random

For the same application (see Section II), motorettes with trapezoidal slots hosting a random winding with round conductors are built and tested in order to identify the trend of the parameter K_{AC} vs. frequency. The full analysis and experimental campaign are detailed in [98], where different winding topologies were proposed with the goal of achieving an optimal solution for reduced copper losses. The built motorettes within random winding has been shown in Chapter 4

In [98], it was found that the AC losses are significantly dependent on the position of the various strands, especially for high frequency operating points. Hence, in this work, where the results have to be compared against those relative to the hairpin motorettes, the trend of K_{AC} is plotted considering a mean value μ_{ESM} and a standard deviation σ_{ESM} found out leveraging on the experimental statistical method [98].

Fig. 6.12 shows the experimental comparison between hairpin and random windings in terms of K_{AC} vs. frequency, up to 1 kHz. For the random winding, the minimum and maximum K_{AC} values that give the 66% probability of having a value inside the range $\mu_{ESM} \pm \sigma_{ESM}$ are considered. It can be noticed that the hairpin solutions perform better than the random ones in the low frequency range. This is due to the higher slot fill factor and the ensuing lower DC resistance. Most importantly, Fig.6.12 highlights that the 2 hairpin solutions $q=4, k=8$ and $q=4, k=4$ segmented achieve lower losses than the 66% of the possible solutions that can happen with random windings up to ≈ 900 Hz. These results, besides proving that some hairpin layouts (including the proposed segmented one) can present lower losses than random windings even at high frequency operations, also demonstrate that the segmented layout presents similar performance to the 8-layer hairpin configuration, albeit with a reduced number of layers per slot, thus potentially leading to a simplification of the manufacturing process.

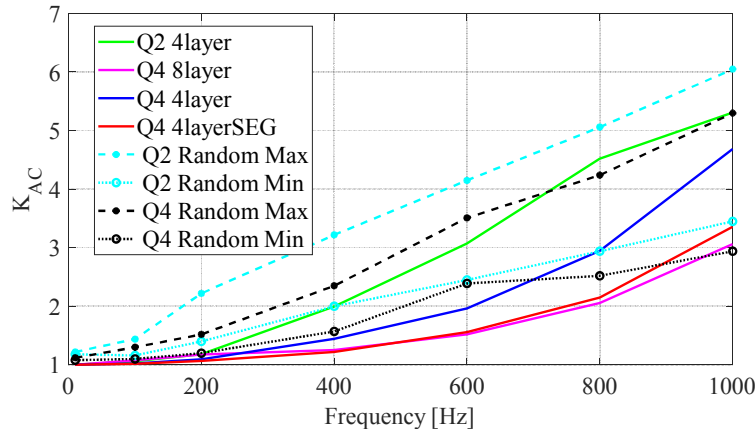


Fig. 6.12. Experimental results: random vs. hairpin windings.

6.8. Conclusion

In this work, an improved hairpin winding topology was proposed to reduce ohmic losses at high frequency operations. This concept, named as segmented hairpin, consists of splitting one or more slot conductors in two or more sub-conductors, similarly to the “strand” concept usually implemented in random windings. In this paper, it was decided to split two conductors in two sub-conductors, as this was deemed to be the optimal solution in terms of loss reduction and minimization of the manufacturing complexities.

The losses produced at various frequency operations within the proposed segmented hairpin winding were assessed against conventional hairpin and random solutions. Analytical and finite element models were used to such purposes, taking into account both slot and end-winding regions. A simplified 2D finite element model was implemented to predict losses in the end-windings, thus avoiding the need of building an accurate but very computationally-expensive 3D model. The relevant findings proved that the AC end-winding losses can be significant in some cases, whereas they are regularly overlooked in previous literature.

In terms of loss reduction, promising analytical and finite element results were obtained for the proposed segmented concept. These perceived benefits were then validated by building and testing stator motorettes featuring various winding arrangements. Compared to conventional hairpin layouts, the segmented hairpin solution achieved a loss reduction

always higher than 20% starting from ≈ 600 Hz, reaching a peak reduction of 28% at 1 kHz, thus proving its potential. In chapter, 5 we achieved an higher loss reduction but was not demonstrated because out of the scope of the research activity that the topologies considered were suitable to achieve the machine targets. The winding configuration considered take into account also the machine performances to achieve.

Finally, a comparison between random and hairpin windings designed for the same traction application was performed. Both conventional and segmented hairpin layouts provided lower losses than random windings at low frequency, as expected. Additionally and importantly, the proposed segmented hairpin solution achieved loss values similar to random windings up to 900 Hz, thus proving its competitiveness for a broader range of operational frequencies.

Chapter 7

Modelling of Voltage Distribution within rectangular wire

This chapter discusses the modelling approach adopted for the estimation of the voltage distribution within rectangular wire windings of electrical machines. The physical phenomena and the major contributors to the occurrence of the uneven voltage distribution are first described. Then, the equivalent circuit used to predict the voltage distribution is presented in detail. The circuital parameters employed in the equivalent circuit are estimated via finite element electrostatic and electromagnetic analyses. Finally, a numerical tool is used to solve the differential equations describing the equivalent circuit above mentioned. Simulation results with a sensitivity analysis is presented. The model before introduced is adapted also for the particular case with hairpin winding and finally motorette with this winding configuration has been experimentally tested with the aim to validate the model accuracy.

7.1 Background

The voltages to which power apparatus terminals are subjected can be broadly classified as normal or steady state and abnormal or transient [103][104][105][106][107]. Most of the time, power apparatus operates under steady-state voltage, i.e. the voltage is within +10% of nominal, and the frequency is within 1% of rated. All other voltage excitations may be seen as transients, which may arise from short-circuits, switching operations, lightning discharges, and from almost any change in the operating conditions of the system. There are exceptions, for instance, electrical machines fed through PWM voltage source converters, since these produce steep voltage pulses which are applied repeatedly to motor terminals [108]. The inverters may produce voltages with very short rise times, which in presence of long cables may cause strong winding insulation stresses and eventually lead to motor failures.

Standards classify the transient voltages that power equipment experiences into four groups, referred respectively to as low frequency, slow front (or switching), fast front and very fast front transients [109]

- 1) Low-frequency transients are oscillatory voltages (from power frequency to a few kHz), weakly damped and of relatively long duration (i.e., seconds, or even minutes).
- 2) Slow front transients refer to the class of excitation caused by switching operations, fault initiation, or remote lightning strokes. They can be oscillatory (within a frequency range between power frequency and 20 kHz) or unidirectional (with a front time between 0.02 and 5 ms), highly damped, and of short-duration (i.e., in the order of milliseconds).
- 3) Fast front transients are normally aperiodic waves, generally associated to lightning surges with a front time between 0.1 and 20 μ s
- 4) The term very fast front transient is used to refer surges usually encountered in gas insulated substations with rise times in the range of 50 to 100 ns and frequencies from 0.5 to 30 MHz, although there are other switching transients with frequencies within this range.

The capability of a winding to withstand transient voltages depends on the specific surge voltage shape, the winding geometry, the insulation material, the voltage-time withstand characteristic and the past history of the winding [103][104][105][106][107]. The voltage stresses within windings need to be determined to design winding insulation suitable for all kinds of over-voltages. Transients cause overvoltage at machine terminals [110] and uneven voltage distribution within machine windings [111]. The result is increased local thermal and electrical stress on the insulation system and additional losses. Thermal and electrical stresses cause an accelerated degradation of the insulation and its electrical properties [112]. Stator insulation failure is one of the main reasons for machine breakdowns [113]. The introduction of next generation power converters, utilizing wide bandgap (WBG) transistors based on Silicon carbide (SiC) or Gallium Nitride (GaN) further increase the electrical stress.

The accurate prediction of the response of coils and windings to fast or very fast front voltage surges is a complex problem and is generally addressed by building detailed models. The earliest attempts were made in 1910s, but until 1960s these efforts were of limited success due to computational limitations [114]. This changed with the application of digital computers and the development of efficient computational algorithms. In this context, several modelling approaches have been proposed and applied to study the behaviour of coils and windings [115][116][117].

7.2 Problem description

Under steady-state voltage conditions the voltage distribution in a winding is linear and the interturn voltages are low. Under steep-fronted transient voltage conditions the voltage distribution is non-linear and the interturn voltages can be very high. Consequently, the interturn insulation of the winding has to be designed to withstand the stresses caused by high frequency transient voltages and for this purpose the interturn voltages need to be evaluated.

During high frequency transients, windings appear to the system in which they operate as frequency-dependent impedances. To evaluate the surge voltage response of a component winding it is therefore necessary to develop an equivalent circuit, whose response can be obtained by the usual methods of network analysis or using a computer. While for system studies it is sufficient to model the component as a black box model, when the internal transient response is required, a much more detailed model in which all regions of critical dielectric stress are identified needs to be used. Internal transient response is a result of the distributed electrostatic and electromagnetic characteristics of the windings. The transient waves propagate into the winding with a certain velocity, the winding has a certain wave transit time, and the wavefront of the transient can be regarded as being distributed along a length of the winding. For a steep-fronted voltage surge, most of the wave front will reside across the first few turns, which can be overstressed. The wave front slopes off and the amplitude is attenuated as the wave penetrates along the winding. For all practical winding structures, this phenomenon is relatively complex and can only be

investigated by constructing a detailed model and carrying out a numerical solution for the transient response and frequency characteristics in the regions of concern. An accurate model may consider each turn of the winding represented by capacitances, inductances and resistances [103][104][105][106]. Winding capacitances play a crucial role in establishing the initial voltage distribution along the winding when a steep-fronted voltage is suddenly applied. Under these conditions, displacement currents can flow in the winding capacitance, but they cannot flow in the winding itself because of its inductance.

7.3 Modelling approach

The machine winding consists of a chain of series-connected coils that are distributed around the machine stator. Under steep-fronted transient conditions, the effective self-inductance of a coil differs considerably from the 50 Hz value; initially, the self-inductance arises from flux that is confined mainly to paths outside the high-permeability iron core by eddy currents that are set up in the core by the incident surge. The reluctance of the flux paths changes as the flux penetrates into the core. For calculation purposes it may be necessary to consider the self-inductance as a time-varying parameter. Similar considerations apply to the mutual coupling between coils. However, due to the limited extent of flux penetration into the core, the flux linkage from one coil to a coil in a neighbouring slot is very small, so the mutual coupling between coils under surge voltage conditions is also very small. The capacitance between coils is very low because each coil is embedded in a slot which acts as a grounded boundary. The intercoil capacitance is usually limited to that in the line-end coil and is very small too. However, due to the fact that the coil is embedded in the slot, the coil-to-ground is significant [118][119].

7.3.1 Principles for modelling

Considering all the above, the following assumptions can be made when deriving the equivalent circuit of a machine winding:

- The behaviour of the core iron is like that of a grounded sheath and the slot iron boundary may be replaced by a grounded sheath, which is impenetrable to high frequency waves.

- The series inductance and resistance of the coils are frequency dependent due to the eddy currents in the core and to the skin effect in conductors.
- The two opposite overhang parts of the stator core are considered uncoupled because eddy-currents in the core provide effective shielding at high frequencies.
- Overhang and slot parts are also uncoupled because of the eddy current in the core.
- The two parts of the coil at the coil entry are uncoupled since they are nearly perpendicular to each other over most of their length and are further shielded from each other by eddy currents in adjacent coils.
- Insulation between the lamination permits magnetic coupling to the coils inside adjacent slots. However, the two slot parts of the coil are not coupled because of the eddy current in the neighbouring coils.
- Coupling between adjacent coils of different layers in the same slot is a lower effect than the close coupling between adjacent turns.
- The capacitive couplings between coils of one phase winding, and between coils of different phase windings, are very small and are usually neglected.
- The capacitance between turns in a coil and between the coil and the core are important and should be taken into account. The dielectric losses must be also represented.
- Only TEM propagation mode is considered, so the theory of multiconductor transmission lines can thus be applied to the slot sections [119].
- The basic unit in the equivalent circuit for the winding is a coil. A stator coil occupies two distinct regions of the machine (see Fig. 7.12): 1) the slot region, in which the active coil sides are placed inside the slots in the magnetic core structure and 2) the overhang region, in which the end turns are positioned in air. The two slot regions are electromagnetically remote, as are the two end-winding regions.
- A uniform untransposed multiconductor transmission line model, composed of a number of conductors equal to that of the coil turns, is considered for each region.

- The multiconductor lines have different electrical characteristics in each region. As a result, the coil has a series of five transmission lines with discontinuities at the junctions between the lines. The five interconnections constitute five discontinuities for wave transits: four discontinuities are due to the iron/air interfaces and the fifth due to interruption of an end-winding section by the coil terminals.
- The time duration for the study can be limited to that corresponding to the period of time of propagation of the surge voltage through these coils.
- The effect of adding more coils to the model on the voltage distribution in the line end coil diminishes as the number of coils increased.
- The number of coils needed in a winding to enable the line end coil voltage distribution to be predicted accurately increases as the number of turns per coil is reduced.

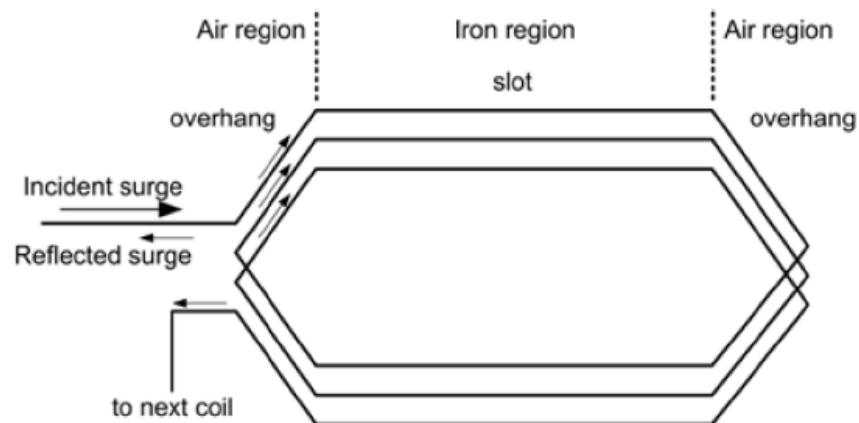


Fig. 7.12. full representation of a machine coil and its subdivision

When a surge impinges on the line-end coil of a machine winding, as shown in Fig. 7.12, it breaks up into transmitted surges moving away from the overhang region and a reflected surge travelling back into the surge source network. The transmitted surges propagate along the overhang section until they reach the slot entry, where they encounter a change in surge impedance. This change causes further reflections and refractions. Each turn of

the coil may be modelled as a single conductor transmission line coupled to its neighbour turns.

7.3.2 Lumped-parameter model

Fig. 7.13 shows the cross section of a machine slot, with the winding active sides and the relevant equivalent circuit parameters highlighted. An accurate representation of the winding for determining interturn voltage distribution should be based on a multiconductor transmission line with uniformly distributed and frequency-dependent parameters. Nevertheless, a distributed-parameter winding model may be very time consuming and for many practical cases this detailed model can be reduced by lumping series elements within an active side of a single turn and shunt elements between active sides of different turns.

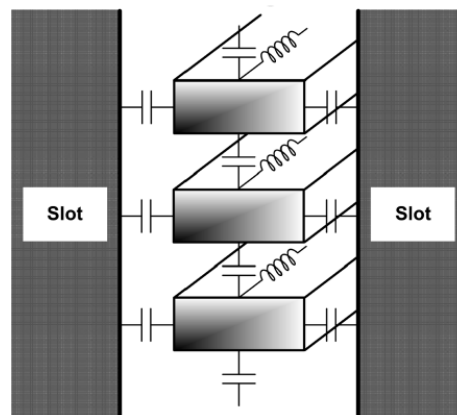


Fig. 7.13. Cross section of a machine slot, with active sides and relevant circuit parameters highlighted.

Therefore, the active side of a single turn can be represented by series resistances (i.e. $R_{i,i}$) and inductances (i.e. $L_{i,i}$) with mutual inductances between turns (i.e. $L_{i,j}$), and parallel (i.e. $C_{i,g}$) and series (i.e. $C_{i,j}$) capacitances arranged as in Fig. 7.14. Resistances in parallel to these capacitances should be also included in such a network to model the dielectric losses accurately. Representing accurately the loss mechanism can require a rather complicated model, which should also address the frequency-dependent characteristic of the losses. However, when conventional impulse (as opposed to oscillatory) waves are applied, the peak voltage normally occurs on the first major oscillation and the error

incurred by not modelling the winding loss is rather small. For these reasons, this study is carried out without including the loss model.

Proper choice of the segment length for lumped-parameter modelling is fundamental. Analysis of fast front transients (in the order of hundreds of kHz) using one segment per coil of the winding can be sufficient, whereas very fast front transients (in the order of MHz) might require

considering one segment per turn. Therefore, even a lumped-parameter circuit can be very large and computationally expensive. The size of the sections in these representations should be small enough to assume that the current flowing through a section is constant.

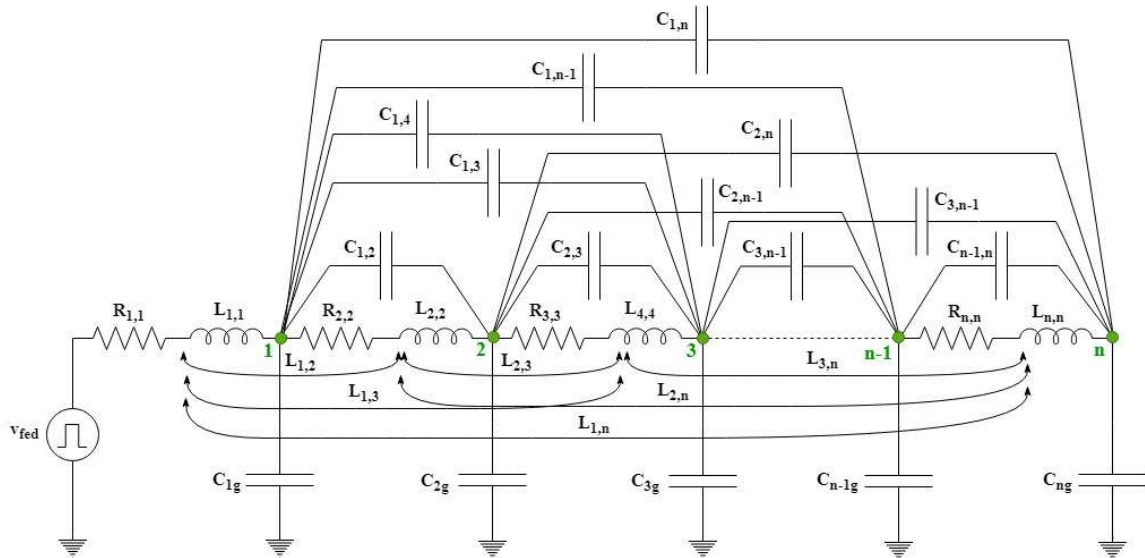


Fig. 7.14. Equivalent lumped-parameter circuit.

As mentioned , the complete coil model should be represented by five sections corresponding to the different parts shown in Fig. 7.12 and the equivalent circuit of any of those sections would be as that reported in Fig. 7.14 [120]. However, at this stage of the work, all of the 3D effects have been neglected and therefore the whole model coincides with that shown in Fig. 7.14. Additional reduction of the network may not yield useful results for transient voltage investigations. The circuit on Fig. 7.3 is used to predict the voltage distribution in the slot, the dynamic of the circuit is influenced also from the rest of the winding. In this analysis an additional resistance, inductance and capacitance is added to the n-node in order to lumped the rest of the circuit and to consider the effect

given by all the winding. Being the phenomena described very fast and the transitory of the wave finish in the first turns, the parameters of the rest of the circuit are considered at the swiching frequency. The lumped capacitance is consider equal to 1 Farad.

7.3.3 Equations for the lumped-parameters model

It is clear that any electrical circuit software can be used to solve the network of Fig. 7.14, however this would be manageable only when the number of nodes is limited and, most importantly, it would not be flexible since a different network should be built everytime the number of nodes (i.e. the number of conductors in the slot) needs to be modified. Hence, the lumped-parameter model, with either constant or frequency-dependent parameters, should be solved using any numerical tool, irrespectively of its number of elements and nodes. While the implementation of the model will be described later on in this report, this section is dedicated to obtain the state-variable formulation which can be used to approximate the behaviour of a machine winding in high frequency transients.

Considering that only the input voltage v_{fed} is known, at any node i of the network made of n nodes, the Kirchoff's current law can be applied thus obtaining (7.1). In (7.1), i_i and i_{i+1} indicate the currents entering the nodes i and $i+1$ respectively, v_i is the voltage across C_{gi} and v_k that across all of the C_{ik} comprised in the circuit, with $k \neq i$ and ranging from 1 to n).

$$i_i - i_{i+1} - C_{ig} \frac{dv_i}{dt} - \sum_{\substack{k=1 \\ k \neq i}}^n C_{i,k} \frac{d(v_i - v_k)}{dt} = 0 \quad (7.1)$$

Always referring to the circuit of Fig. 7.14, the Kirchoff's voltage law can be applied to any loop including 2 adjacent node-to-ground capacitances, i.e. $C_{i,g}$ and $C_{i+1,g}$, and the series parameters $R_{i,i}$ and $L_{i,i}$. The expression (7.2) is thus obtained and provided below.

$$v_{i-1} - v_i - R_{i,i} i_i - L_{i,i} \frac{di_i}{dt} - \sum_{\substack{k=1 \\ k \neq i}}^n L_{i,k} \frac{di_k}{dt} = 0 \quad (7.2)$$

The Kirchoff's voltage law needs to be used also to the additional loop including v_{fed} , $R_{i,i}$, $L_{i,I}$ and C_{1g} , thus resulting in the equation shown in (7.3).

$$v_{fed} - v_1 - R_{1,1}i_1 - L_{1,1}\frac{di_1}{dt} - \sum_{k=2}^n L_{1,k}\frac{di_k}{dt} = 0 \quad (7.3)$$

From (7.1)-(7.3), it can be noticed that the system state variables are the currents entering in each node the voltages across the node-to-ground capacitances of the network. To tidily group the state variables in two independent vectors, equations (7.1) and (7.2) can be firstly elaborated as in (7.4) and (7.5), respectively. In order to include (7.3) in this representation and in particular within (7.5), one can assume that when $i=1$, then $v_{i-1} = v_{fed}$.

$$i_i - i_{i+1} = \left(C_{ig} + \sum_{\substack{k=1 \\ k \neq i}}^n C_{i,k} \right) \frac{dv_i}{dt} - \sum_{\substack{k=1 \\ k \neq i}}^n C_{i,k} \frac{dv_k}{dt} \quad (7.4)$$

$$v_{i-1} - v_i = R_{i,i}i_i + L_{i,i}\frac{di_i}{dt} + \sum_{\substack{k=1 \\ k \neq i}}^n L_{i,k}\frac{di_k}{dt} \quad (7.5)$$

The above expressions can be fully exploited as shown in (7.6) and (7.7). In (7.6), $(v_1 \ v_2 \ \dots \ v_n)^T$ is just the vector \bar{v} comprising the state variables "voltages", whose derivative with respect to time is multiplied by a matrix of capacitances which will be named \mathbf{C}_{sw} afterwards. In (7.7), $(i_1 \ i_2 \ \dots \ i_n)^T$ is the vector \bar{i} including the state variables "currents", which is multiplied by a diagonal matrix (which will be referred to as \mathbf{R} afterwards) whose elements are the series resistances of the equivalent circuit, whereas its derivative with respect to time is multiplied by a matrix containing self- (on the main diagonal) and mutual-inductances (which will be named \mathbf{L} from now onward).

$$\begin{pmatrix} i_1 - i_2 \\ i_2 - i_3 \\ i_3 - i_4 \\ \vdots \\ i_{n-1} - i_n \end{pmatrix} = \begin{pmatrix} C_{1g} + \sum_{\substack{k=1 \\ k \neq 1}}^n C_{1,k} & -C_{1,2} & -C_{1,3} & \dots & -C_{1,n} \\ -C_{2,1} & C_{2g} + \sum_{\substack{k=1 \\ k \neq 2}}^n C_{2,k} & -C_{2,3} & \dots & -C_{2,n} \\ -C_{3,1} & -C_{3,2} & \ddots & \ddots & \vdots \\ \vdots & \vdots & \ddots & \ddots & -C_{n-1,n} \\ -C_{n,1} & -C_{n,2} & \dots & -C_{n,n-1} & C_{ng} + \sum_{\substack{k=1 \\ k \neq n}}^n C_{n,k} \end{pmatrix} \frac{d}{dt} \begin{pmatrix} v_1 \\ v_2 \\ v_3 \\ \vdots \\ v_n \end{pmatrix} \quad (7.6)$$

$$\begin{pmatrix} v_{fed} - v_1 \\ v_1 - v_2 \\ v_2 - v_3 \\ \vdots \\ v_{n-1} - v_n \end{pmatrix} = \begin{pmatrix} R_{1,1} & 0 & 0 & \dots & 0 \\ 0 & R_{2,2} & 0 & \dots & 0 \\ 0 & 0 & \ddots & \ddots & \vdots \\ \vdots & \vdots & \ddots & \ddots & 0 \\ 0 & 0 & \dots & 0 & R_{n,n} \end{pmatrix} \begin{pmatrix} i_1 \\ i_2 \\ i_3 \\ \vdots \\ i_n \end{pmatrix} + \begin{pmatrix} L_{1,1} & L_{1,2} & L_{1,3} & \dots & L_{1,n} \\ L_{2,1} & L_{2,2} & L_{2,3} & \dots & L_{2,n} \\ L_{3,1} & L_{3,2} & L_{3,3} & \ddots & \vdots \\ \vdots & \vdots & \ddots & \ddots & L_{n-1,n} \\ L_{n,1} & L_{n,2} & \dots & L_{n,n-1} & L_{n,n} \end{pmatrix} \frac{d}{dt} \begin{pmatrix} i_1 \\ i_2 \\ i_3 \\ \vdots \\ i_n \end{pmatrix} \quad (7.7)$$

By introducing the new matrix \mathbf{D} defined as in (7.8) and the new vector $\overline{v_{fed}} = (v_{fed} \ 0 \ \dots \ 0)^T$, (7.6) and (7.7) can be compacted in the forms provided in (7.10) and (7.9), respectively.

$$\mathbf{D} = \begin{pmatrix} -1 & 0 & 0 & \dots & 0 \\ 1 & -1 & 0 & \dots & 0 \\ 0 & 1 & \ddots & \ddots & \vdots \\ \vdots & \vdots & \ddots & \ddots & 0 \\ 0 & 0 & \dots & 1 & -1 \end{pmatrix} \quad (7.8)$$

$$-\mathbf{D}^T \bar{i} = \mathbf{C}_{sw} \frac{d\bar{v}}{dt} \quad (7.9)$$

$$\overline{v_{fed}} + \mathbf{D} \bar{v} = \mathbf{R} \bar{i} + \mathbf{L} \frac{d\bar{i}}{dt} \quad (7.10)$$

Finally, (7.9) and (7.10) can be written in the state form as shown in (7.11) and (7.12). These final expressions can now be easily implemented in any software aimed at analysing dynamic systems.

$$\frac{d\bar{v}}{dt} = \mathbf{C}_{sw}^{-1} (-\mathbf{D}^T \bar{i}) \quad (7.11)$$

$$\frac{d\bar{i}}{dt} = \mathbf{L}^{-1} (\overline{v_{fed}} + \mathbf{D} \bar{v} - \mathbf{R} \bar{i}) \quad (7.12)$$

Matlab Simulink is used for such purposes and its representation is illustrated in Fig. 7.15, where the equations (7.11) and (7.12) are implemented using the elementary blocks embedded within the software. The state variables are determined through the integrator blocks "1/s", as seen in the Figure 7.4.

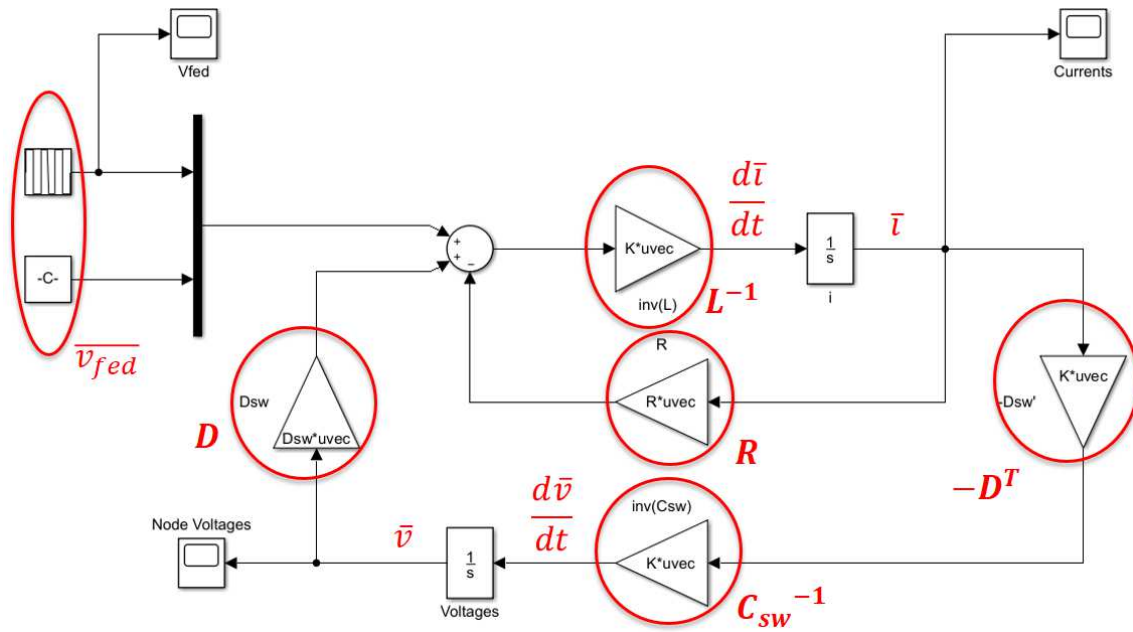


Fig. 7.15. Model implementation in Matlab Simulink.

Whilst the model shown in Fig. 7.15 represents the final stage to determine the solution of the lumped-parameters equivalent circuit reported in Fig. 7.14, it obviously necessitates the information relative to the values of all of the elements included in the matrices \mathbf{R} , \mathbf{L} and \mathbf{C}_{sw} , which are still unknown at this stage. To accurately calculate these circuitual parameters and thus to populate the above mentioned matrices, 2D finite element (FE) models of one machine slot are built. Their detailed description is provided in the next section.

7.3.4 2D Circuitual parameters determination

Given the complexity associated to an eventual analytical determination of the resistances, inductances and capacitances of the lumped-parameters circuit under investigation, a FE analysis is chosen as means to have an accurate estimation of the parameters. Considering all the assumptions and hypotheses described above in sections 7.3.1 and 7.3.2, only one

slot is modelled and the 3D effects are neglected at this stage. The FE software used for these purposes are produced by Mentor Infolytica, which include a number of simulation tools. Among these, the electric field simulation software ElecNet is used to find the capacitances, whereas the low-frequency electromagnetics simulation software MagNet is employed for resistances and inductances. Apart from some differences inherently related to the nature of the problems, most of the pre-processing and solving features (such as creation of the geometry, assignment of materials, meshing and simulation parameters, types of solvers, etc.) are common to both software. To make the models as flexible as possible and to allow for an easy modification of the most relevant aspects of the models whenever required, ElecNet's and MagNet's scripting technologies are used to communicate with Matlab, where a list of design parameters is first defined. These include

1) Slot dimensions

- Axial length of the slot model
- Slot width and height
- Tooth width
- Yoke height
- Slot opening width and height
- Corner fittings

2) Coil features

- Number of winding layers
- Number of turns per coil
- Number of conductors in parallel within a turn
- Conductor diameter

3) Insulation properties

- Thickness of the gap between iron parts and slot liner
- External slot liner width, height and corner fittings
- Thickness of the gap between external and internal slot liners
- Internal slot liner width, height and corner fittings
- Enamel thickness

After having defined the above geometrical dimensions for the model, for a given problem, also the material assignment is common to both ElecNet and MagNet. These simulation tools have several material libraries in which a number of "model materials" of different type are available. However, an illimited number of "user materials" can be held and thus

purposely built. Therefore, the materials which need to be used for the FE analyses can be assigned for the following model parts:

- Slot
- Conductors
- Enamel
- Slot liners
- Gap between slot and external liner
- Gap between external and internal liners
- Gaps between conductors

Besides the above components, for both the electric field and electromagnetic simulations, an airbox made of air needs to be built to limit the domain of analysis and thus the computational times.

Considering all the above and launching the geometry creation and material assignment tasks from Matlab, the outcome of both ElecNet and MagNet is as illustrated in Fig. 7.16, where the slot (in light grey), the external and internal liners (in yellow), the conductors (in light orange) and the enamel around them (in dark orange) are observed.

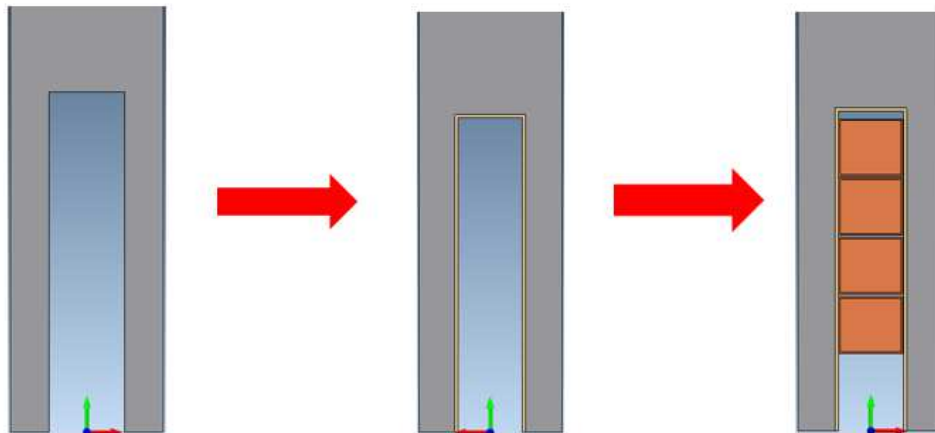


Fig. 7.16. Creation of the slot geometry and materials assignment.

Although many other properties are similar for ElecNet and MagNet, the next steps towards the final objective, i.e. to determine the parameters to be used in the assumed equivalent circuit, are provided separately for the capacitances (through ElecNet) and resistances and inductances (through MagNet). First, the modelling properties associated to the capacitances determination is described.

7.3.4.1 Capacitances determination via electric field simulation software

The next step after having built the geometry and assigned the materials consists of imposing the boundary conditions to the model. As mentioned above, an outer boundary (airbox) needs to be defined to limit the domain of analysis: this is done following the general rule that the areas where the electric field is perceived to be weak do not need to be modelled in great detail. To such outer airbox, a “flux tangential” boundary condition is applied by default, meaning that the normal component of the electric field is constrained to zero and the flux is made to flow tangentially alongside the boundary. In addition, according to the considerations carried out in section 7.3, the slot acts as a grounded boundary at high frequencies. In ElecNet, the “ground” boundary condition is available and thus this is applied to the modelled slot, which now represents an electrically grounded conductor, where the electric potential is constrained to zero. As a result, the electric field is made normal to the boundary. For the sake of clarity, a 3D dynamic view of the slot model is reported in Fig. 7.17, where the outer boundary and the grounded slot can be seen.

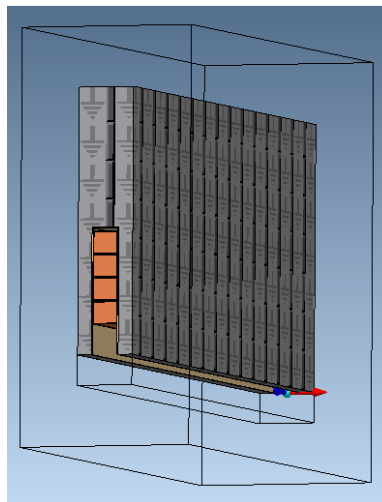


Fig. 7.17. Dynamic view of the slot model.

To specify the voltage over a component, the latter has to be changed to an electrode. All the conductors built within the model are thus changes to electrodes. Finally, before selecting the most suitable solver and then running the simulation, the mesh needs to be defined. First of all, it is worth mentioning that electrodes are not meshed, as there is no

need to calculate the potential or the electric field inside it. The grounded slot is considered as an electrode with 0 V, meaning that also this component is not meshed. All the rest of the components are meshed in such a way to achieve high accuracy in the main areas of interest. Hence, focus is given to the components within the slot, i.e. all the insulations, whereas a less dense mesh is used for the areas surrounding the slot. To do so, the tools available in ElecNet, such as the maximum (finite) element edge size, are used. Fig. 7.18 shows the solution mesh obtained after a suitable refinement aimed at maximising the accuracy while also keeping the computational times under acceptable limits.

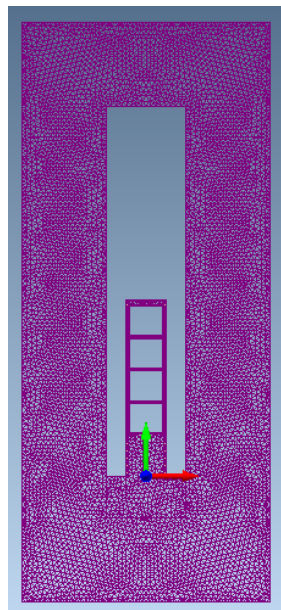


Fig. 7.18. Solution mesh of the FE model in ElecNet.

With the definition of the mesh, the model is fully defined and is ready for the solution. ElecNet solves Maxwell's equations to find the electric field within the model. Before solving, however, a number of simulation parameters can be opportunely set. While the convergence method cannot be freely chosen since the only one available for 2D problems is the Newton-Raphson method, the polynomial order, the Newton tolerance, the conjugate gradient tolerance and the maximum number of iterations can be suitably selected by the user. The details of such choices are not given here, but it is worth mentioning that their values are the outcome of a trade-off study aimed at maximising the accuracy while limiting the computational effort.

Several types of solvers are available within ElecNet. Among them, the fastest and most appropriate one for the purposes of such project is the “time-harmonic” solutions. ElecNet's time-harmonic solver finds the time-harmonic electric fields produced by specified AC voltages. The conducting materials can be isotropic or anisotropic. The electric materials can be linear and isotropic or anisotropic. The time-harmonic analysis is analysed at one specified frequency. Sources and fields are represented by complex phasors.

To determine the capacitances of the equivalent circuit under study (see Fig. 7.14), a first evaluation is carried out by imposing a voltage equal to 10 V to any i of the conductors (electrodes), keeping at 0 V all the other $n-1$ ones. In this way, after the solution is ready, the self-capacitance (i.e. the capacitance C_{ig} node-to-ground) and the mutual-capacitances between the i^{th} electrode and all of the other $n-1$ ones (i.e. the turn-to-turn capacitances $C_{i,k}$, with $k=1,\dots,n$ and $k\neq i$) are calculated through phasorial analysis. It is clear that for obtaining all the capacitances of the equivalent circuit, a number of simulations n equal to the considered number of turns (electrodes) need to be performed. It is worth mentioning that, after completing this set of FE evaluations, the determined capacitances have to be first stored and then manipulated in Matlab in such a way to obtain the matrix \mathbf{C}_{sw} (see (7.6), (7.9) and (7.11)) necessary for the numerical resolution (see Fig. 7.15) of the lumped-parameters circuit assumed in Fig. 7.14.

7.3.4.2 Resistances and inductances determination via electromagnetic simulation software

Keeping in mind that all the steps relative to the geometry creation and the material assignment described in the previous sections are also valid for the electromagnetic FE analysis within MagNet (refer to Fig. 7.16), in this section, all the rest of the modelling passages necessary to finally calculate the circuital resistances and inductances is detailed. As per the electric field analysis, an outer airbox is defined to limit the domain of analysis and the same general rules apply for defining its dimensions. Also, in MagNet a “flux tangential” boundary condition is applied by default to such airbox, meaning that the normal component of the magnetic flux density is constrained to zero and the flux is made

to flow tangentially alongside the boundary. No additional boundary conditions are needed for the sake of this investigation.

Each modelled conductor needs to be defined as a coil comprising 1 turn in MagNet. These n coils are all modelled as "solid". A solid coil, as opposed to "stranded", is a solid piece of conductor, in which the current is free to flow according to Maxwell's equations. This allows to accurately take into account the potential non-uniform current distribution occurring at high frequencies, thus guaranteeing the correct estimation of the resistances.

When the operating frequency is such that the current distribution is uniform within the conductors, these are treated as stranded (as they are in reality) even though they are modelled as solid. On the other hand, modelling the conductors as stranded may lead to inaccurate results when the operating frequencies are such that the current distribution is not uniform within the conductors.

As well as for the electric field simulation analysis, a suitable solution mesh is defined according to the same rationale aimed to achieve high accuracy and low computational times. The tools used in ElecNet for refining the mesh are also available in MagNet. In this case, the main areas of interest also involve the conductors (coils). This concept can be seen in the solution mesh reported in Fig. 7.19 for completeness.

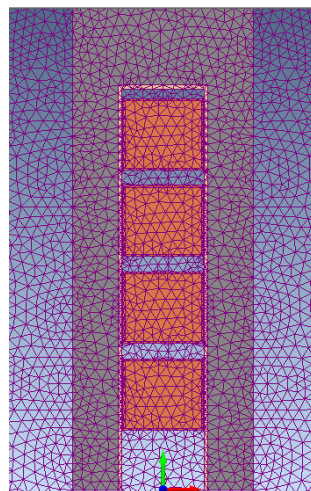


Fig. 7.19. Solution mesh of the FE model in MagNet.

With the definition of the mesh, the model is fully defined and is ready for the solution. MagNet solves Maxwell's equations to find the magnetic field within the model. Before

solving, the simulation parameters are opportunely selected and the same rules as for the electric field analysis are applied here.

Time-harmonic solutions are employed also for the FE evaluations in MagNet. MagNet's time-harmonic solver finds the time-harmonic magnetic field in and around current-carrying conductors, in the presence of materials that can be conducting, magnetic or both. The conducting materials can be isotropic or anisotropic. The magnetic materials can be linear and isotropic or anisotropic. Time-harmonic analyses are carried out at one specified frequency. Sources and fields are represented by complex phasors.

Theoretically, time-harmonic analysis is only possible when all the materials in the problem are linear. If they are non-linear, sinusoidally-varying sources will not give rise to sinusoidally-varying fields, and time-harmonic analysis is not possible. However, MagNet's time-harmonic 2D solvers are actually quasi non-linear solvers, taking into account the approximate material non-linearities by trying to find the operation point on a non-linear B-H curve, using its first few data points.

To determine the resistances and the inductances of the equivalent circuit under study (see Fig. 7.14), a first evaluation is carried out by imposing a current equal to 1 A to any i of the conductors (coils), keeping at 0 A all the other $n-1$ ones. In this way, after the solution is ready, the coil resistance (i.e. the series resistance $R_{i,i}$), the self-inductance (i.e. the series inductance $L_{i,i}$) and the mutual-inductances between the i^{th} coil and all of the other $n-1$ ones (i.e. the inductances $L_{i,k}$, with $k=1,\dots,n$ and $k\neq i$) are calculated through phasorial analysis. It is clear that a number of simulations n equal to the considered number of turns (coils) need to be performed to obtain all the resistances and inductances of the equivalent circuit. It is worth mentioning that, after completing this set of FE evaluations, the determined circuital parameters have to be first stored and then manipulated in Matlab in such a way to obtain the matrices \mathbf{R} and \mathbf{L} (see (7.7), (7.10) and (7.12)) necessary for the numerical resolution (see Fig. 7.15) of the lumped-parameters circuit assumed in Fig. 7.14.

7.3.4.3 Further remarks

In the previous sections, the FE-based methodologies implemented for the circuital parameters determination have been discussed. Before detailing the specific tools used for the capacitances (section 7.3.4.1) and for resistances and inductances (section 7.3.4.2), the design parameters which initialise the problem under investigation have been listed down. Thanks to the FE software's scripting technologies, the whole process can be fully automated in Matlab, which thus sequentially launches ElecNet and Magnet for the FE analysis. Therefore, starting from those design parameters, the geometry is first created, then the materials are assigned, the boundary conditions and electrodes/coils are defined, the mesh is produced and finally the solution is achieved. The simulation results are then imported via scripting in Matlab for the post-processing, which is aimed at calculating the circuital parameters and storing them in the form necessary to solve the equivalent circuit. Considering the above, it can be easily inferred that the model is highly flexible, just due to the scripting features which allow to modify the design parameters depending on the specific problem under investigation. To visually demonstrate the claimed model flexibility, two different case studies are shown below in Fig. 7.20, where all the possible geometrical variations permitted by the implemented tool are highlighted. The slot size and the number of harpin per slot is changed.

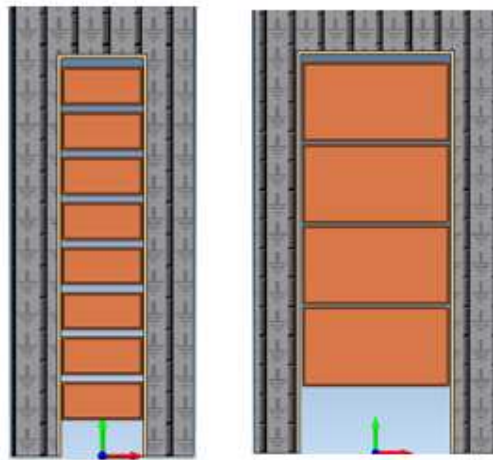


Fig. 7.20. Two case studies showing the model flexibility in terms of geometrical dimensions.

In conclusion, it is also worth mentioning the solving speed of both (ElecNet and MagNet) FE models deriving from having chosen the time-harmonic solver. ElecNet's computational time is less than 1s per capacitance, while for Magnet this time is a few seconds. The overall computational time thus depends on the number n of turns per slot, which corresponds to the dimension of the system of differential equations envisioned in (7.11) and (7.12).

7.3.5 Summary

In Section 7.3, the modelling approach adopted for studying the voltage distribution within windings when these are excited by steep-fronted transient voltages was described. First, the modelling principles were detailed (see Section 7.3.1) and the assumptions which led to the definition of a lumped-parameters equivalent circuit (see Section 7.3.2 and Fig. 7.14) were highlighted. The differential equations relevant to the assumed equivalent circuit (see Section 7.3.3) and their implementation into the system model built in Matlab Simulink (see Fig. 7.15) were presented in detail. Finally, the 2D FE models built and implemented for the estimation of the identified circuital parameters (i.e. turn resistances and inductances, turn-to-turn inductances, turn-to-stator capacitances and turn-to-turn capacitances) were characterised (see Section 7.3.4.1 and 7.3.4.2), pointing out their flexibility and speed of resolution (see Section 7.3.4.3).

The whole automated process is coded in Matlab and the relevant steps, ranging from the definition of the geometrical dimensions of the slot model to the solution of the dynamic system, are provided below:

- 1) The characteristic design parameters, such as slot dimensions, number of conductors per slot, slot and conductor insulation thicknesses and materials, are defined in Matlab.
- 2) Matlab opens ElecNet, where the slot model is built and a number of simulations are performed to determine the capacitances.
- 3) Matlab opens MagNet, where the slot model is built and a number of simulations are performed to determine resistances and inductances.

- 4) The calculated equivalent circuit parameters are elaborated in Matlab in such a way to obtain the matrices \mathbf{R} , \mathbf{L} and \mathbf{C}_{sw} needed for the system resolution.
- 5) The input parameters are defined for the voltage source V_{fed} .
- 6) Matlab opens Simulink, where the dynamic system model is built and the simulation is run, thus finding the state variables, i.e. 1) turn currents and 2) node voltages.
- 7) Matlab post processes the results by plotting the obtained state variables.

Fig. 7.21 qualitatively summarises these steps.

The results relative to the steps described in Points 5)-7) will be the focus of the next section.

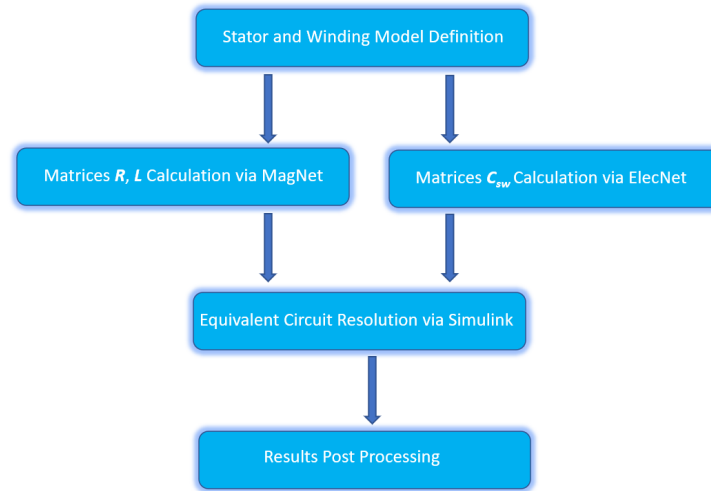


Fig. 7.21. Qualitative illustration of the automated procedure.

7.4 Modelling results

7.4.1 Reference systems

Before going into the details of the simulation results, it is worth recalling the case studies under analysis within this work. Based on a specific mission profile, three different solutions have been designed to achieve the target needed. The analysis illustrated in Fig. 7.10 have been done aiming to choose the configuration which assure the best performance in term of voltage stress. Two stator characterised by 24 slots (i.e. the number of slots per pole per phase q is equal to 4) and one stator with 12 slots (i.e. the

number of slots per pole per phase q is equal to 2) have been considered. Three different rectangular wire winding configurations have been investigated:

- a 4 layers per slot layout for the stator with 12 slots,
- a 4 layers per slot layout for one of the two stators having 24 slots, and
- an 8 layers per slot layout with two parallel paths for the last stator with 24 slots.

To investigate the uneven voltage distribution within the armature winding of these motorettes potentially resulting from steep-fronted transient voltages generated by the power electronics converters feeding them, motorette frames aimed at replicating as much as possible the stator slot profile are considered. In Fig. 7.11 the three slot configurations analysed are shown.

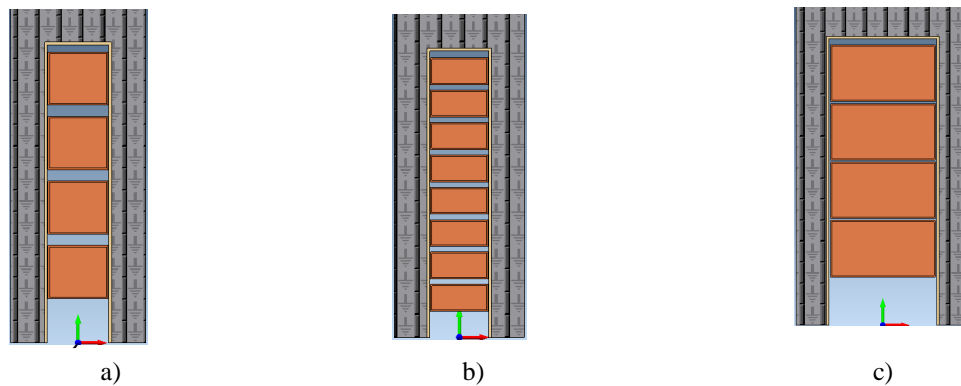


Fig. 7.11: sketch of the reference system slots: a) slot with $q=4$ and winding with 4 layers ; b) slot with $q=4$ and winding with 8 layers ; c) slot with $q=2$ and winding with 4 layers.

In Table 7.1, products and specifications of the items involved in the machine slot are listed. These will be used in the FE models for the parameters' estimation. The motorette material is M270-35A, while the other features correspond to those provided in 1, Table 7.2 and Table 7.3.

TABLE 7.1 : PRODUCTS AND SPECIFICATIONS OF THE SLOT ITEMS.

Item	Products	Thickness	Relative permittivity
Enamelled copper wire	Polyester C200 G2 IEC 60317-29	200 μm	2.5
Phase insulation	Kapton	200 μm	4.0
Cover slider	NKN	300 μm	3.0
Slot insulation	NKN	250 μm	3.0

TABLE 7.2: HAIRPIN DIMENSIONS.

Conductor Dimension	q4_4layers	q4_4layers	q4_4layers
Widht [mm]	4	4	8.2
Height [mm]	3.5	1.75	4.3

7.4.2 Simulation results

The modelling results are obtained by following the procedure detailed in Section 7.3.5. In the previous sections, the reference system design parameters have been introduced and adopted for the FE models with the aim of determining the circuital components.

Before dealing with the equivalent circuit solution results, a few observations are listed below regarding some general results on the values of the circuital parameters, calculated for supply frequencies equal to 10 kHz:

- 1) the turn-to-ground capacitances C_{ig} are all in the order of few picoFarad in the whole range of considered frequencies;
- 2) the turn-to-ground capacitances of the conductors 1 and n , namely C_{1g} and C_{ng} , have very similar values in the whole range of frequencies considered, and these are 3-to-5 times bigger than those of the remaining conductors due their location in proximity of the slot bottom. For example, at 50Hz, $C_{1g}=C_{ng}=4.6\text{pF}$, while the remaining capacitances are around 1.5pF;
- 3) The turn-to-turn capacitances between two adjacent conductors, e.g. $C_{1,n}$, $C_{1,2}$, $C_{2,3}$ and so on, are of the same order of magnitude of the various C_{ig} and 1-to-4 orders

- of magnitude bigger than all of the remaining turn-to-turn capacitances $C_{j,k}$, in the whole range of frequencies considered;
- 4) For a given frequency, the values of the resistances $R_{i,i}$ are rather similar for all of the conductors, while for a given conductor they vary from 0.06Ω to 100Ω ranging from 10 kHz to 18 MHz.
 - 5) The turn self- and mutual-inductances are all in the order of few tens of nanoHenry in the whole range of considered frequencies. For example, at 10 kHz, $L_{1,1} = 0.31 \mu\text{H}$, while $L_{1,2} = 0.28 \mu\text{H}$.

The next step towards the dynamic system resolution is to define the steep-fronted transient voltage v_{fed} , which represents the input of the model implemented in Simulink (see Fig. 7.15). To do so, a bipolar supply from the converter is hypothesised, meaning that v_{fed} is an AC periodic waveform with period T equal to the inverse of the supply frequency f_{PWM} , peak-to-peak value equal to the DC-link voltage V_{DC} and null mean value. v_{fed} is implemented in Matlab in such a way to modify its amplitude, frequency, dv/dt and duty cycle k_{DC} whenever required. As an example, the case when 1) amplitude is 200 V (i.e. $V_{DC} = 400 \text{ V}$), 2) frequency is 10kHz, 3) dv/dt is 20 kV/ μs and 4) duty cycle is 0.5 is reported in Fig. 7.12.

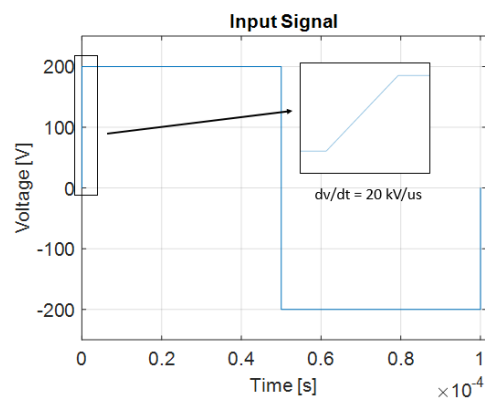


Fig. 7.12. Input voltage waveform from the converter output at $f_{PWM} = 10\text{kHz}$, $V_{DC} = 400\text{V}$, $dv/dt = 20\text{Kv}/\mu\text{s}$ and $k_{DC} = 0.5$.

The definition of v_{fed} is the last step before running the system simulation in Simulink and thus solving the considered equivalent circuit. The solver "ode23s" is used for the simulations [121]. Considering only one phase, the matrices of the circuit parameters

are slightly “corrected” considering that the motorettes actually consists of 8 slots for $q=4$ and 4 slots for $q=2$, whereas a 1 slot FE model is adopted for their estimation. No further fitting has been performed. Therefore, using the input voltage (replicated a number of times in relation to the simulation stop time) plotted in Fig. 7.12, the state variables are finally obtained.

7.4.3 Sensitivity analysis

The observations carried out in the previous section are valid in general for the sake of the voltage distribution estimation. However, more detailed results are presented in this section taking into account the variation of some relevant parameters of the supply voltage v_{red} and their influence on the voltage distribution. Since preliminary investigations on random windings have led to the conclusion that duty cycle and supply frequency have negligible effects on the phenomena under investigation, these parameters are kept constant at 0.5 and 10 kHz respectively, while varying DC-link voltage and dv/dt as described below:

- the DC-link voltage V_{DC} , considering 4 values: 400 V, 550 V, 700 V and 800 V;
- the dv/dt considering 5 values: 3 kV/ μ s, 7 kV/ μ s, 11 kV/ μ s, 15 kV/ μ s and 20 kV/ μ s.

7.4.3.1 dv/dt and DC-link voltage

In [119], the key indicator chosen for the sensitivity study, i.e. the first-to-last turn voltage, has been shown to be poorly dependent on both the duty cycle and the supply frequency. On the other hand, a relatively high sensitivity to the DC-link voltage and the dv/dt has been proven. To visualise how the input voltage vary according to its characteristic parameters, two examples of v_{red} with 1) $dv/dt=3$ kV/ μ s and $V_{DC}=800$ V and 2) $dv/dt=20$ kV/ μ s and $V_{DC}=400$ V are given in

Fig. , with a in-zoom on the first quarter of the input voltage. In order to take into account, the potential impact that different winding techniques may have on the voltage distribution, two different layouts have been considered. The first one, namely TYPE A, considers the winding starting from the bottom of the slot, whereas the second case,

namely TYPE B, considers the first layer at the top of the slot (close to the slot opening). In Fig.7.14 both these methods are shown and each layer is properly numbered. These investigations have been performed for all the three motorettes described above.

Then, the 3D plots of Fig. and Figure 7.16 report the turn-to-turn voltage between the first and second turn ($v_{1,2}$) in % vs. dv/dt (y-axis) and V_{DC} (x-axis), at $k_{DC}=0.5$ and $f_{PWM}=10$ kHz for all of the three models under analysis, with the TYPE A and TYPE B respectively.

In these Figures, the dv/dt is confirmed to be the most influencing parameter, with the worst-case scenarios recorded at the highest dv/dt value assumed, i.e. 20 kV/ μ s). In addition, $v_{1,2}$ is strongly dependent on V_{DC} only when $V_{DC}=400$ V for the winding configurations with 4 layers. When the 8 layers case is studied, the $v_{1,2}$ is strongly dependent on V_{DC} for the whole range of voltage levels considered. Both configurations (TYPE A and TYPE B) give very similar results to each other. The reason of this is that each layer has a resistance value close to the other value, the same happens also with the capacitance and the inductance. For TYPE A, to the first layer is associate the element $R(1,1)$, $L(1,1)$, $C(1,1)$ of the matrix R-L-C, instead to the last layer the element $R(n,n)$, $L(n,n)$, $C(n,n)$. Instead, considering the TYPE B, its first layer is the last one of the TYPE A (as shown in Figure. 7.13). Being the values of element $R(1,1)$, $L(1,1)$, $C(1,1)$ very close to the elements $R(n,n)$, $L(n,n)$, $C(n,n)$ the response of the dynamic system described in section 7.3.3 is similar for both cases.

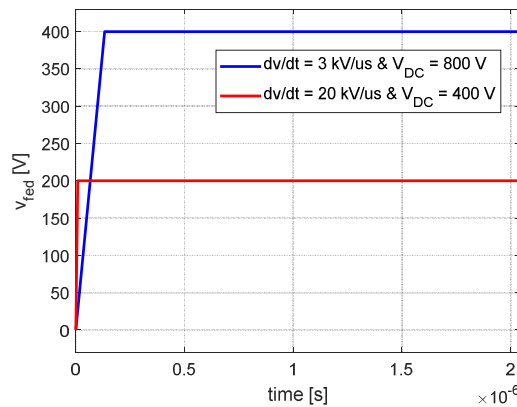


Fig. 7.13: comparison between input voltages at two different dv/dt and VDC, i.e. 1) $dv/dt=3$ kV/ μ s & VDC=800 V and 2) $dv/dt=20$ kV/ μ s & VDC=400 V.

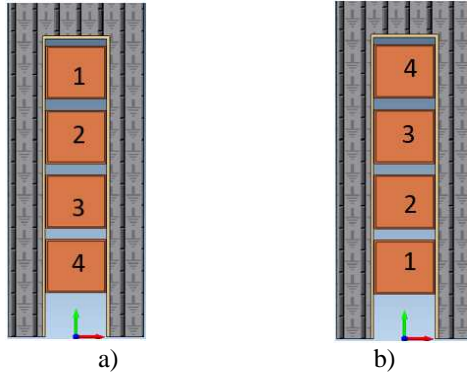


Fig. 7.14: Kind of winding considered: a) TYPE A; b) TYPE B.

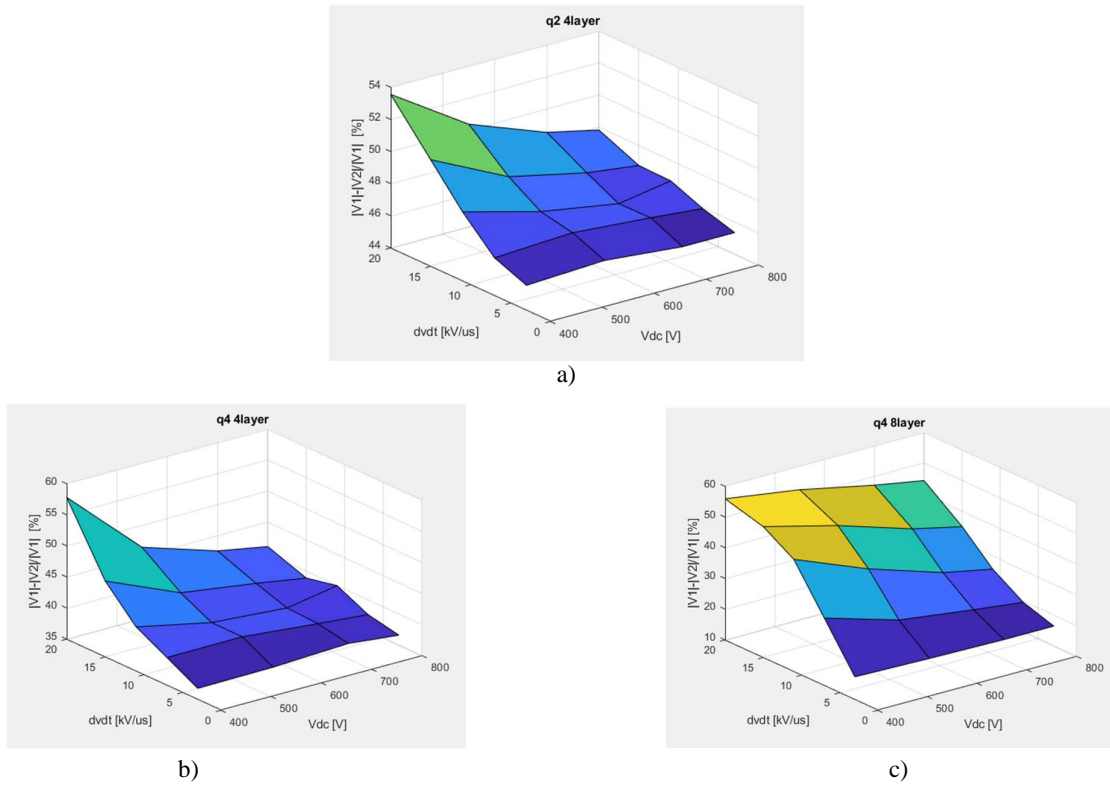
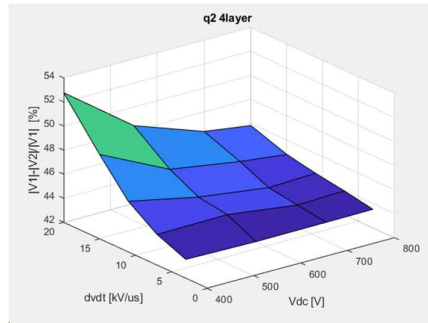
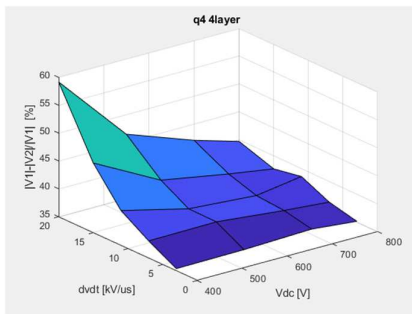


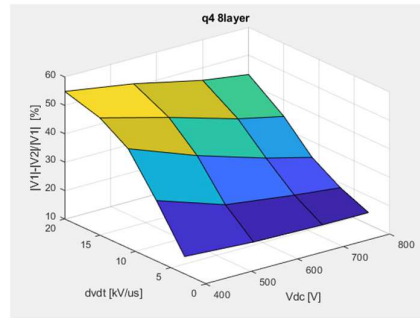
Fig. 7.15: $v_{1,2}$ vs. dv/dt and VDC for TYPE A : a) q2 4layer ; b) q2 4layer ; c) q4 8layer.



a)



b)



c)

Fig. 7.16: $v_{1,12}$ vs. dv/dt and VDC for TYPE B : a) q2 4layer ; b) q2 4layer ; c) q4 8layer.

7.5 Experimental Results

In the previous section, the simulation results obtained from the model developed to study the uneven voltage distribution in machine windings have been detailed. A sensitivity analysis has been performed with the aim of understanding the parameters which mostly influence such phenomenon when these windings are supplied by steep-fronted surges. A specific reference system has been considered as case study. To replicate as closely as possible the stator slot of the reference electrical machine, all three motorettes have been built to validate the modelling results. A picture of the motorette is provided below in Fig. , where all turns have been made accessible for voltage probing.

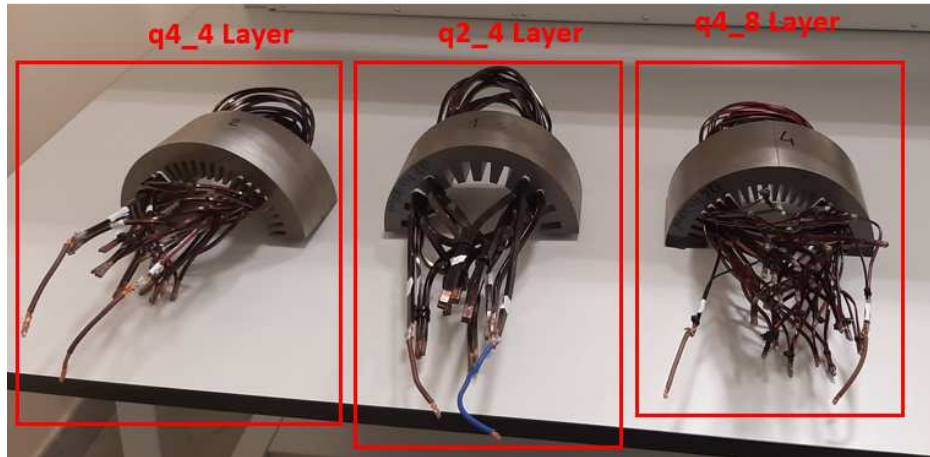


Fig. 7.17. Built motorette.

7.5.1 Test set-up and preliminary investigations

The aim of this section is to prove that the phenomena under investigation occur experimentally. The validation of the modelling results requires additional steps which will be clarified in Section 7.6 and is thus postponed to a later stage. The test set up, Fig. 7.18, consists of a DC power supply feeding a SiC-based H-bridge whose output is directly connected to the motorette. A Hall effect probe is used to measure the current and passive differential voltage probes are used to record the voltages (either turn to converter output terminal or turn-to-turn) results. The attenuation differential voltage probe has been set equal to 100 X, it means that to have the real value measured we need to multiply by 100 the oscilloscope value. The user interface allows to start any test, select a unipolar or bipolar converter output, modify duty cycle and dv/dt , etc.

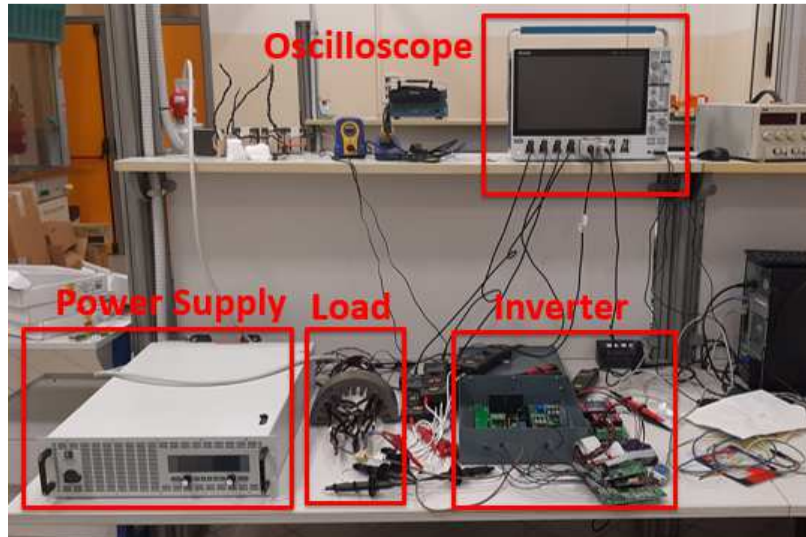


Fig. 7.18. Experimental set-up.

7.5.2 No Load Test Results

The schematic that represent the No Load and On Load test is described in Fig 7.19 .For all of the three motorette has been chosen to capture the first four turns of the winding being the physical phenomena present mainly on the first turns. Having null current it is possible to neglect the contribution of self and mutual inductances in the model a provide a first validation of the ohmic-capacitive circuit. A 1500 V, 30 A DC power supply is used to provide the desired voltage values. The additional inductance of 1 mH is removed and only 1 motorette is used. All differential voltage probes are connected to the negative terminal of the DC-link thus guaranteeing the null current operation at steady state.

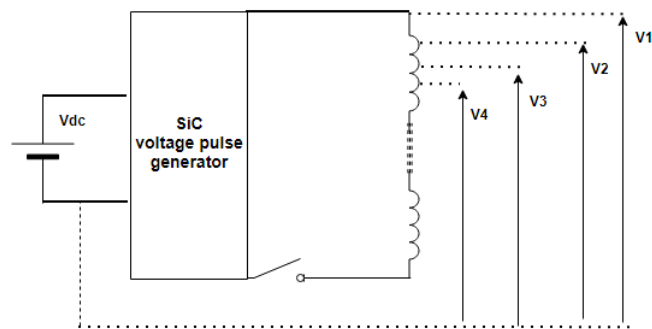


Fig. 7.19. No Load Test schematic.

7.5.2.1 General trends

Under these testing conditions the dv/dt and DC-link voltage are the Figures which mostly influence the voltage distribution, 3 different input voltage levels (i.e. 200 V, 275 V, 350 V) and 2 dv/dt values (8ns and 17ns) are investigated for each different voltage level. Higher voltage values are not considered due to the voltage limits of the capacitance that otherwise would fail. The supply frequency is set at 30 kHz and the duty cycle at 0.5 for these first set of measurements, given their negligible influence on the studied phenomena. According to the No Load Schematic, the node voltages at the 1st (namely V_1) , 2nd (namely V_2), 3th (namely V_3) and 4th (namely V_4) turns of the motorette coil (using the negative terminal of the DC-link as reference) are recorded .The oscilloscope channel 1 ,2,3 and 4 capture the V_1 , V_2 , V_3 , V_4 respectively. Fig 7.20 reports the oscilloscope capture of node voltages for motorette with q2_4layer at $k_{DC}=0.5$, with $f_{PWM}=30kHz$, $V_{DC}=200$ V, rise time=8 ns (Fig. 7.22.a) and 17 ns (Fig. 7.22.b) .This Figure highlight how the dv/dt influence the overshoot voltage to the first turns. The peak voltage is over 400 V in the first case and less 300 V in the second case with a smoother step voltage front.

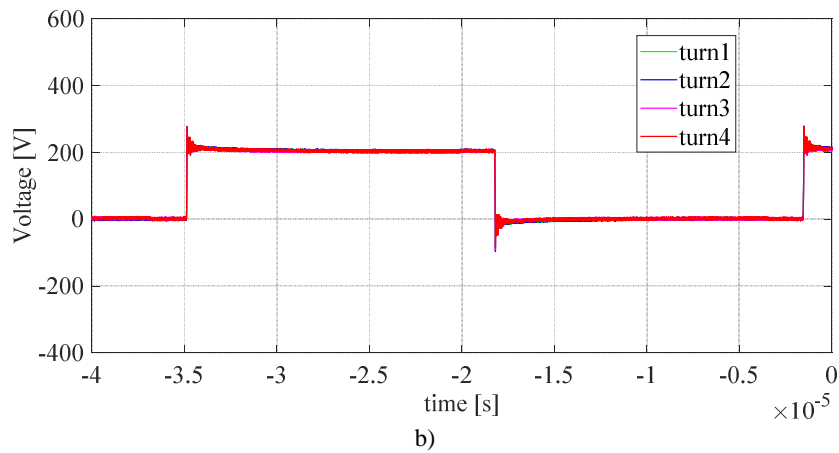
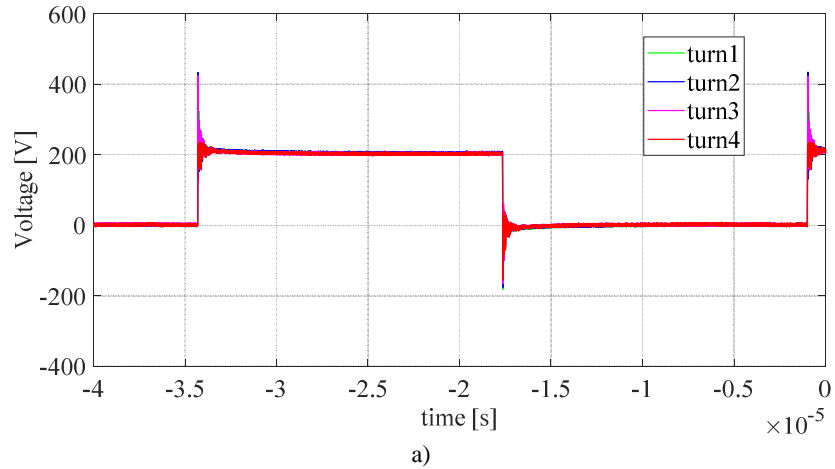


Fig. 7.20: oscilloscope capture for node voltages with motorette q2_4Layer at $k_{DC}=0.5$, with $f_{PWM}=30\text{kHz}$, $V_{DC}=200\text{ V}$: a)rise time = 8 ns ; b) rise time 17 ns.

The results before confirms that the voltage difference between turns in no load conditions is negligible and the overshoot voltages are due from rise time value and from the inverter gate voltage waveforms, the last one has usually some overshoot itself that gives an important contribute to increase the peak voltages in the turns. Fig. 7.21, 7.22 and 7.23 reports the oscilloscope acquisitions of node voltages for motorette the three motorette tested at $k_{DC}=0.5$, rise time=8ns, $f_{PWM}=30\text{kHz}$, $V_{DC}=200\text{ V}$, $V_{DC}=275\text{ V}$ and $V_{DC}=350\text{ V}$.

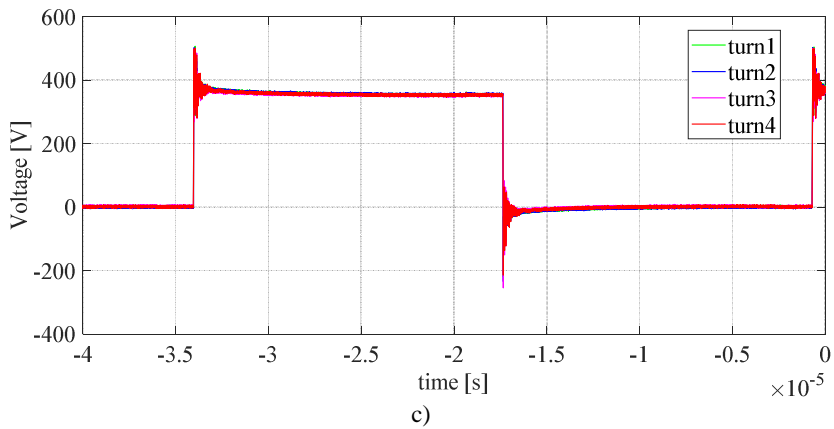
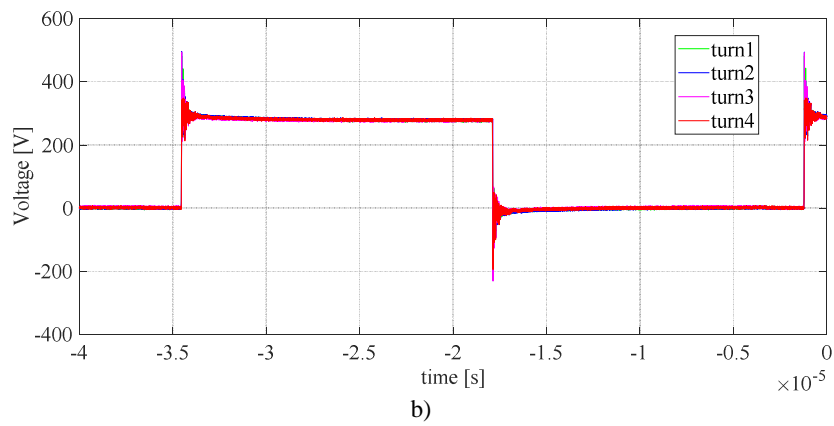
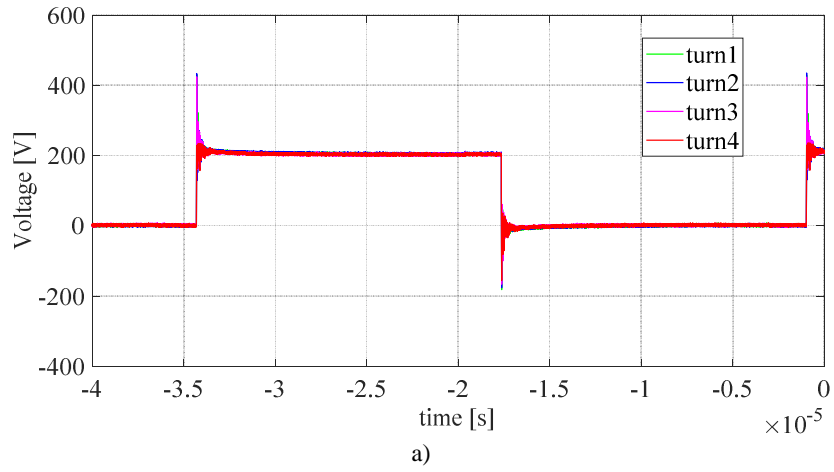


Fig. 7.21: oscilloscope capture for node voltages with motorette q2_4Layer at $k_{DC}=0.5$, with $f_{PWM}=30\text{kHz}$: a) $V_{DC}=200\text{ V}$; b) $V_{DC}=275\text{ V}$; $V_{DC}=350\text{ V}$.

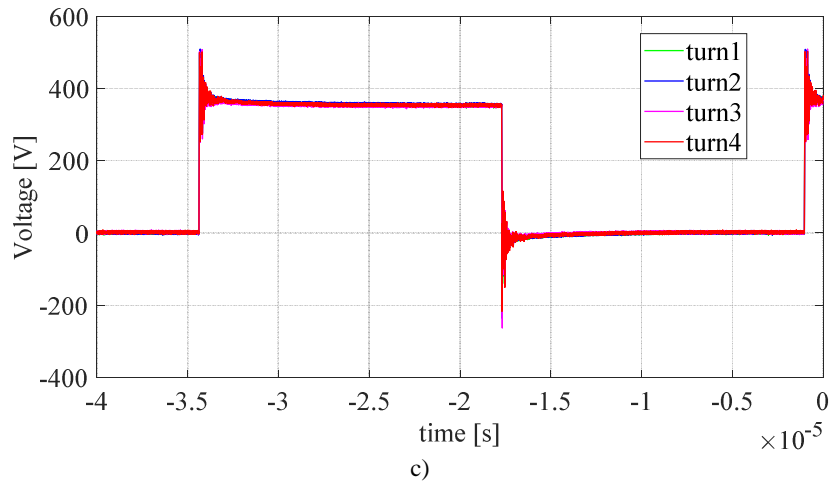
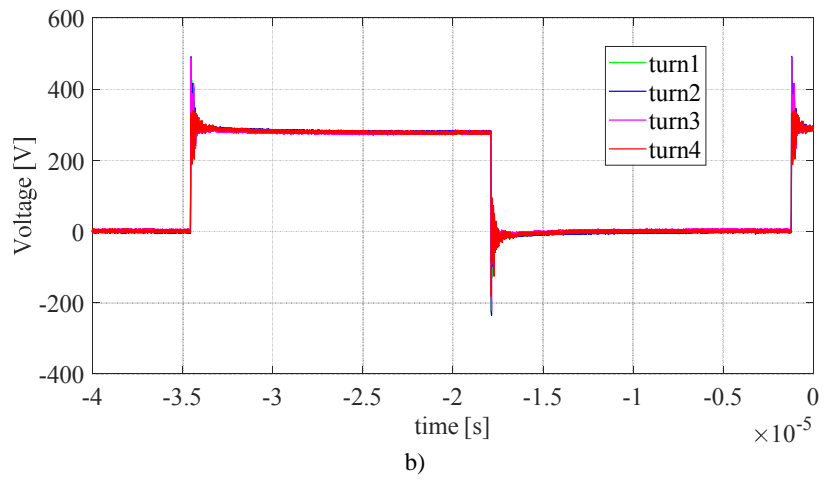
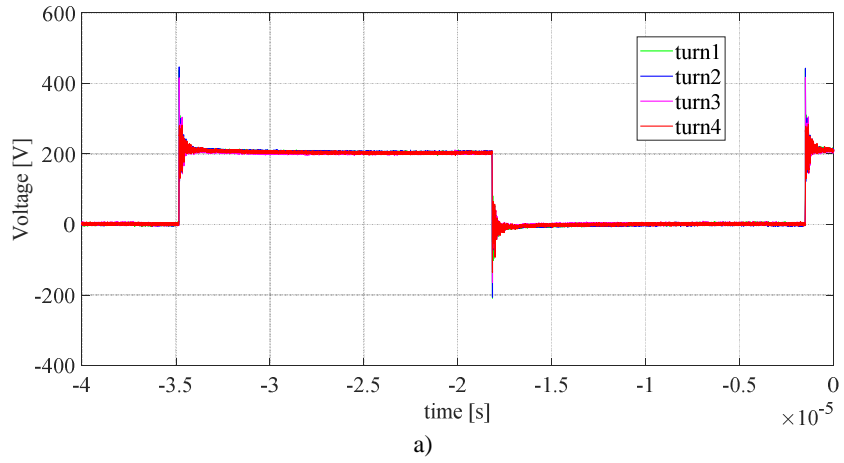


Fig. 7.22: oscilloscope capture for node voltages with motorette q4_4Layer at $k_{DC}=0.5$, with $f_{PWM}=30\text{kHz}$: a) $V_{DC}=200\text{ V}$; b) $V_{DC}=275\text{ V}$; $V_{DC}=350\text{ V}$.

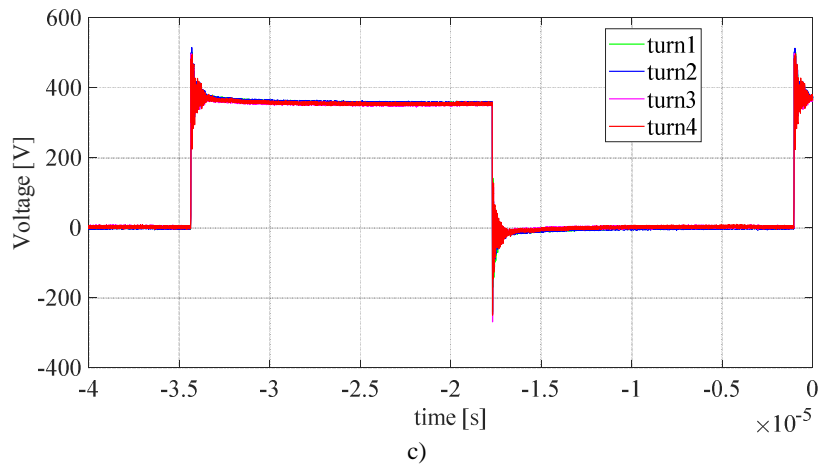
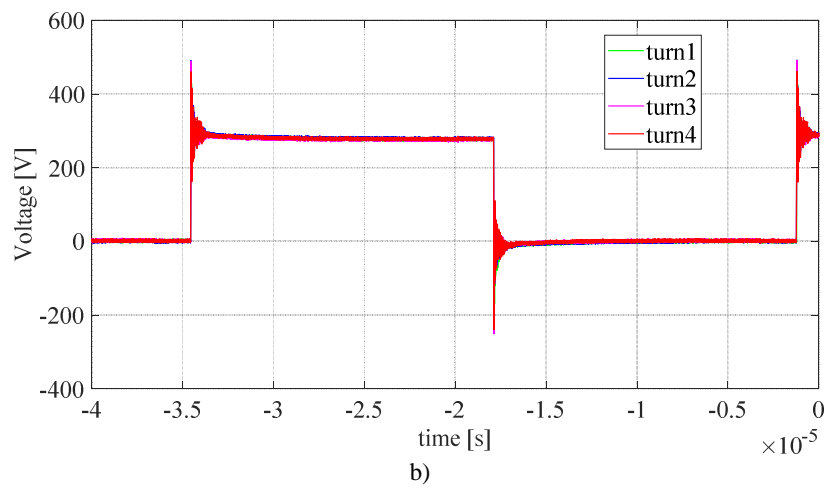
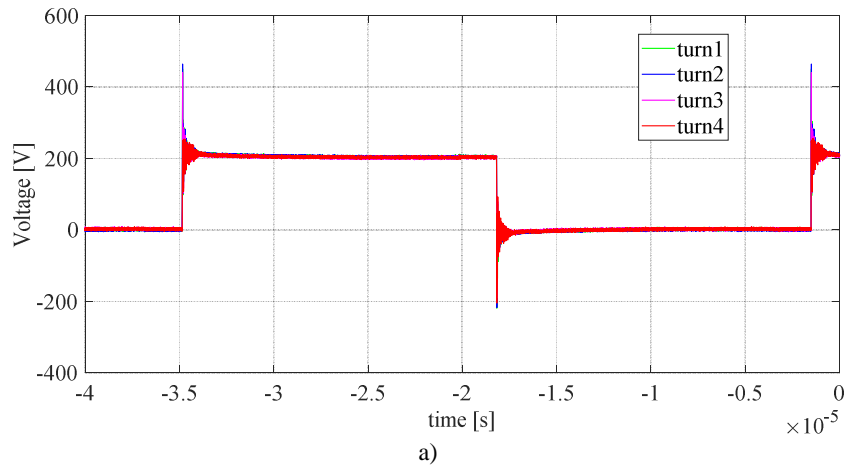


Fig. 7.23 oscilloscope capture for node voltages with motorette q4_8Layer at $k_{DC}=0.5$, with $f_{PWM}=30\text{kHz}$: a) $V_{DC}=200\text{ V}$; b) $V_{DC}=275\text{ V}$; $V_{DC}=350\text{ V}$.

7.5.3 On Load Test Results

The schematic that represent the No Load and On Load test is described in Fig.7.24 .For all of the three motorette has been chosen to capture the first four turns of the winding being the physical phenomena present mainly on the first turns. All differential voltage probes are connected to the negative terminal of the DC-link thus guaranteeing the null current operation at steady state.

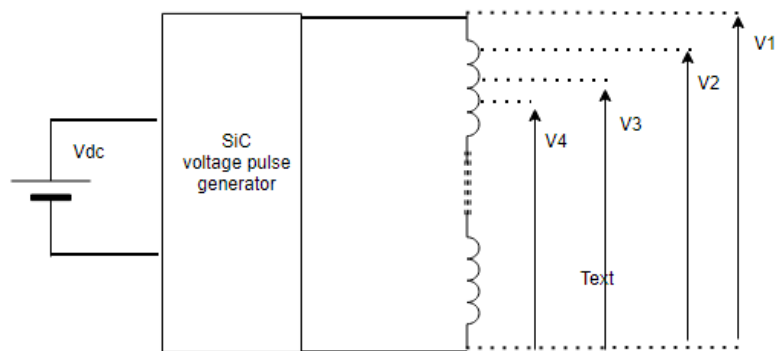
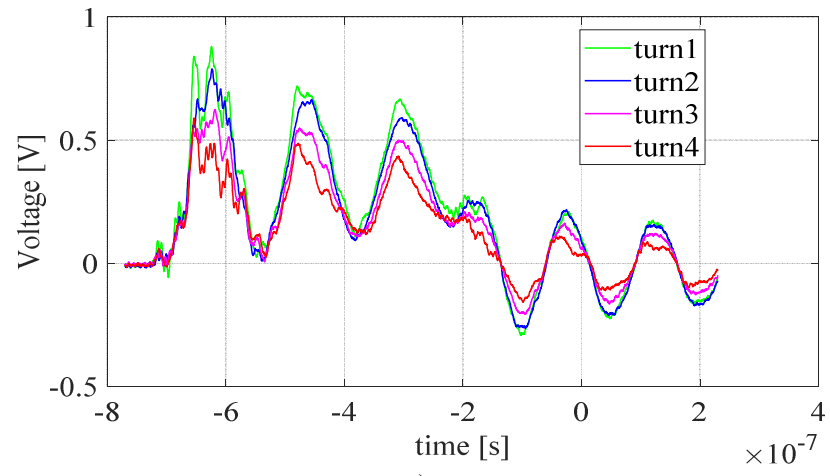


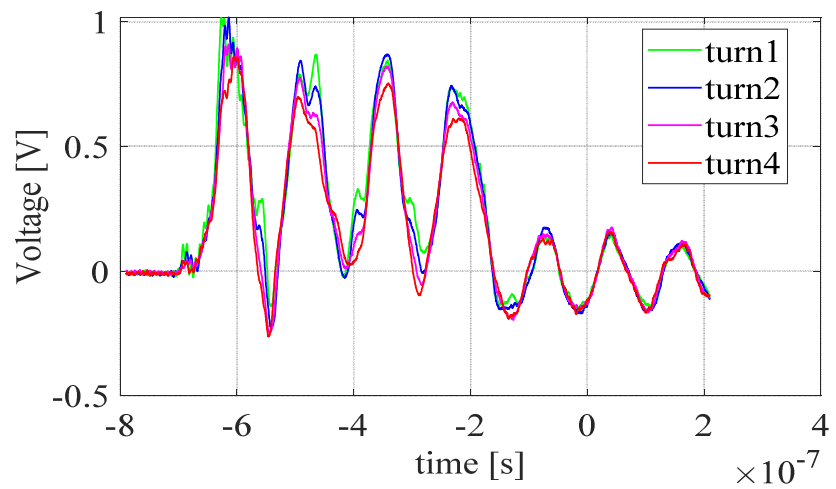
Fig. 7.24. On Load Test schematic.

7.5.3.1 General trends

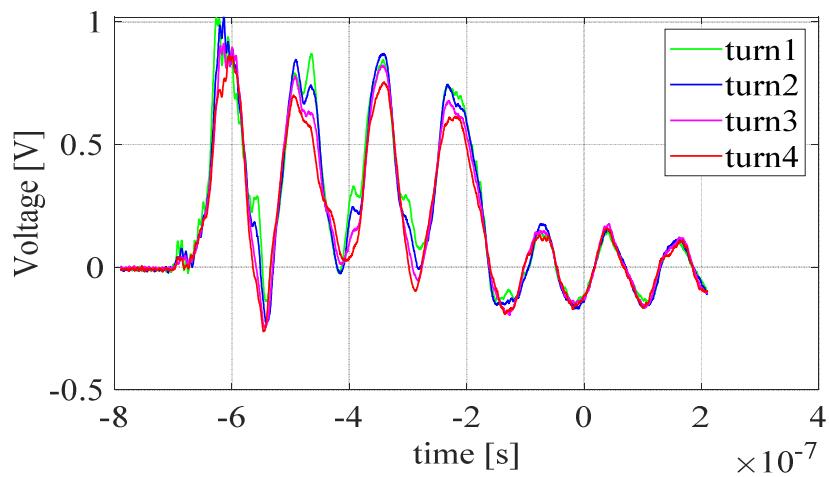
The supply frequency is set at 30 kHz and the duty cycle at 0.05 for these first set of measurements, given their negligible influence on the studied phenomena. According to the No Load Schematic, the node voltages at the 1st (namely V_1), 2nd (namely V_2), 3th (namely V_3) and 4th (namely V_4) turns of the motorette coil (using the negative terminal of the DC-link as reference) are recorded . The attenuation differential voltage probe has been set equal to 100 X and connected to the oscilloscope channel 1 ,2,3 and 4 which refer to the V_1 , V_2 , V_3 , V_4 values respectively. Fig. 7.25 reports the node voltages for the three motorette with $k_{DC}=0.5$, $f_{PWM}=30kHz$, $V_{DC}=40 V$, rise time=8 ns (Fig. 7.25.) ns (Fig. 7.25a) .These figures highlight an important overvoltage in the first instant in the first turns achieving up to 100 V, two times more than the V_{DC} .



a)



b)



c)

Figure 7.25. Experimental acquisition of the voltage distribution: a) Q2_4layer; b) Q4_4layer; c) Q8_4layer.

7.6. Comparison between Numerical model and Experimental Model

In section before the slot models has been used to calculated the slot parameters (R-L-C). According to the work [123] the matrixes of R-L-C representing the total winding has to be modified considering that the legs making the hairpin interest at least two different slots and because of the transpositions rules the legs are positioned in different layers such as per Fig. 7.26.

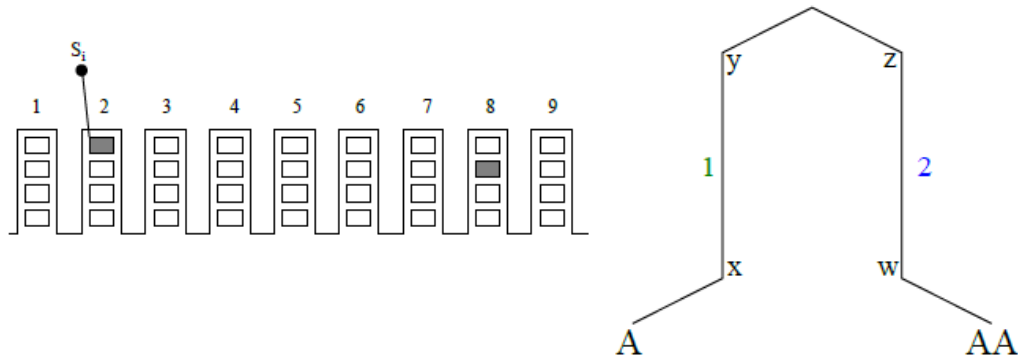


Fig. 7.26. Turn has active sides in first and second layers.

Referring to the winding diagram of the motorette (presented in Annex 1) under analysis (Q2_4layer), the matrix Csw become as per eq. 7.13, the matrix R as per eq. 7.14 and the matrix L as per eq. 7.15 still estimated via finite element calculations.

$$\begin{pmatrix} C_{3,1} & 0 & 0 & 0 & 0 & 0 & C_{3,31} & 0 \\ 0 & C_{9,2} & 0 & 0 & 0 & 0 & 0 & C_{9,42} \\ 0 & 0 & C_{4,3} & 0 & C_{4,13} & 0 & 0 & 0 \\ 0 & 0 & 0 & C_{10,4} & 0 & C_{10,24} & 0 & 0 \\ 0 & 0 & C_{4,31} & 0 & C_{4,1} & 0 & 0 & 0 \\ 0 & 0 & 0 & C_{10,42} & 0 & C_{10,2} & 0 & 0 \\ C_{3,13} & 0 & 0 & 0 & 0 & 0 & C_{3,3} & 0 \\ 0 & C_{9,24} & 0 & 0 & 0 & 0 & 0 & C_{9,4} \end{pmatrix} \quad (7.13)$$

$$\begin{pmatrix} R_{3,1} & 0 & 0 & 0 & 0 & 0 & 0 & 0 \\ 0 & R_{9,2} & 0 & 0 & 0 & 0 & 0 & 0 \\ 0 & 0 & R_{4,3} & 0 & 0 & 0 & 0 & 0 \\ 0 & 0 & 0 & R_{10,4} & 0 & 0 & 0 & 0 \\ 0 & 0 & 0 & 0 & R_{4,1} & 0 & 0 & 0 \\ 0 & 0 & 0 & 0 & 0 & R_{10,2} & 0 & 0 \\ 0 & 0 & 0 & 0 & 0 & 0 & R_{3,3} & 0 \\ 0 & 0 & 0 & 0 & 0 & 0 & 0 & R_{9,4} \end{pmatrix} \quad (7.14)$$

$$\begin{pmatrix} L_{3,1} & 0 & 0 & 0 & 0 & 0 & L_{3,31} & 0 \\ 0 & L_{9,2} & 0 & 0 & 0 & 0 & 0 & L_{9,42} \\ 0 & 0 & L_{4,3} & 0 & L_{4,13} & 0 & 0 & 0 \\ 0 & 0 & 0 & L_{10,4} & 0 & L_{10,24} & 0 & 0 \\ 0 & 0 & L_{4,31} & 0 & L_{4,1} & 0 & 0 & 0 \\ 0 & 0 & 0 & L_{10,42} & 0 & L_{10,2} & 0 & 0 \\ L_{3,13} & 0 & 0 & 0 & 0 & 0 & L_{3,3} & 0 \\ 0 & L_{9,24} & 0 & 0 & 0 & 0 & 0 & L_{9,4} \end{pmatrix} \quad (7.15)$$

In the Fig. 7.28 the match between the numerical model and the experimental results has been showed. The model estimate a quite well the voltage distribution during the first instants, also the overvoltage is quite close with the realty. The error is due to the numerical parameters evaluations. Being the contribute of the end winding not negligible a 2D model is not enough to predict what we have in the realty, a finite element 3D model is need to calculate the parameters.

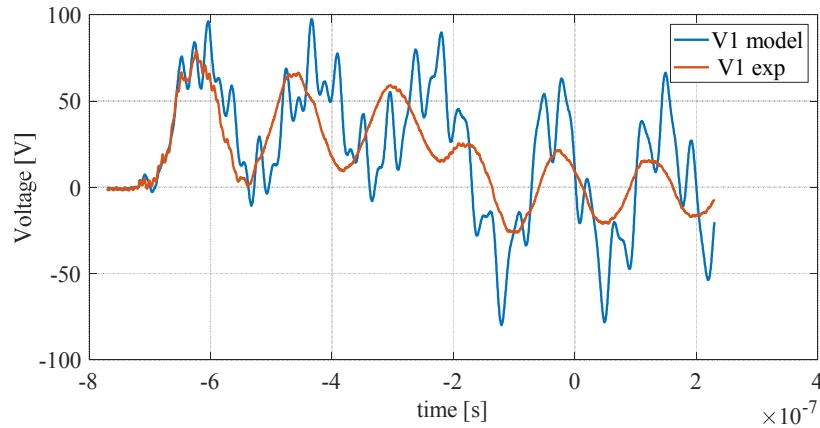


Fig. 7.28: Comparison between numerical and experimental results (q2_4layers).

7.7. Conclusion and next steps

This part of the project dealt with the modelling aspects of voltage distribution within machine hairpin windings when converters, which generate step-fronted transient voltages, supply these. Three different case study are analysed. Two of them have the number of slot per pole per phase (q) equal to 4 and the last one equal to 2. The cases

study with $q=4$ have two different winding topology, the first one has a hairpin winding with 4 layer and the second one with 8 layer. Instead, the case study with $q=2$ has the hairpin winding with four layer. These different cases present different sizes of the conductors, also the matrixes $R - L$ and C will be different each other. All the three case study consider two different way to make the winding useful to find in industry applications (called in this work TYPE A and TYPE B). The fundamental concepts and principles behind such phenomenon were first described and then the modelling approach was presented in detail. In particular, it consists of a lumped-parameter equivalent circuit whose parameters are obtained by electric field and electromagnetic FE evaluations carried out on one slot model. The simulation results were then reported and based on these, a detailed sensitivity was performed. The aim of such study was to capture the most influencing parameters on the voltage distribution. It was found that for the hairpin winding with 4 layers, low DC-link voltage and high dv/dt values significantly impact the phenomenon, different scenario it was found with 8 layers where it is sensitive with all levels of DC-link voltage. No overshoot with respect to the supply voltage is present for all of the three models. Bth way to make the hairpin winding (TYPE A and TYPE B) give results very similar for all of the three case study.

These findings were proven by experimental results carried out at no load conditions, which also confirmed the validity of the modelling approach thanks to excellent match being achieved. Finally, experimental measurements were also performed on load, at low voltage and current levels, highlighting that good match is reached for the first instance after device commutation.

The next step of this work is to validate the models experimentally in order to have a feedback about the accuracy of them and based of this value understand how to improve the models if necessary. Once validated the models onother step forward is necessary to do, a complete converter-cables-motor system will be considered and modelled.

This part of the project dealt to the aspects of voltage distribution within machine windings when these are supplied by converters which generate steep-fronted transient voltages. Three different motorette has been evaluated with three different winding configurations.

The scope of these experimental tests was to evaluate the voltage trends and assure that they are coherent with the trends found with the simulations results. A comparison between the model done to predict the voltage distribution and experimental results has been done. The model describe a quite well the node 1 voltage especially in the first periods, after that the error become too high and the model unreliable. This error is because of the parameters R-L-C calculated via FEM which consider a 2D model instead a 3D model. Being the end winding length comparable with the active length, maybe even more, the 3D effect become important.

Conclusions

The aim of this work was to find some strategies to maximize the electrical machine power density a crucial constraint especially for the automotive market considered the limited space available in the vehicle architecture.

Generally the main contribute in term of losses are given by the iron and copper losses, both dependant with the frequency. In this work after some considerations below discussed, it has been choose to focus all the research activities to the high frequency copper losses. Iron losses are dependant with the material adopted and the manufacturing process, both factors increase a lot the price if has been desired a consistent iron losses reduction. For the mass production such as the automotive industry, costs need big considerations at design and product development stage. Instead, paying attention to the winding topology it is possible to maximize the power density without increasing excessively the material price being the windings often made with copper (or aluminium) independently from hairpin, random solutions. In addition, especially during the peak performance of the machines the copper losses gives the main contribute.

A flexible tool to design optimized electrical machines has been made and presented in this thesis, given the technical specifications an electrical machines has been designed and used as a reference for the research studies. Being in the automotive industry the hairpin and random winding mostly used, both solutions has been analysed.

The copper losses with the random winding are linked to the strand diameter and the relative strands positions. The random winding is very difficult to model in order to predict the losses via finite element simulations and mathematical models. The main issues is about the relative strands position which is unpredictable. In Chapter 4 an Experimental Statistical Method has been presented, which aim to built the basis for future research works. The limit of the method proposed is the cost and the time because a lot of experimental tests are needed, an alternative to reduce costs and time, could be to make a tool able to generate finite element models with different strands position. In this work

only two winding positions have been created through finite element software (“Hz” and “VT”), creating a huge amount of combinations the accuracy will be higher with a lower effort in term of time, facilities and costs.

The hairpin winding present important advantages from manufacturing point of view because a full automated line is possible to realize. However, the designers have to face with this topology because only a few configurations are possible having a limited flexibility due to the manufacturing process. The research in this thesis aimed to find some strategies to reduce high frequency the copper losses within hairpin winding, the main drawback of this kind of winding. In chapter 5 has been presented some theoretical way to reduce the copper losses. In some specific cases, more than 60% of losses reduction has been verified via finite element. However, the electrical machine performance has not evaluated, the work was limited to find out the effect of some geometrical slot parameters to the copper losses in a certain frequency range. This work it could be useful to maximize the power density in some frequency operative range, it seems a bit contradictory but looking for the best trade off, reducing a bit the fill factor and moving farther the conductor from the slot opening as a consequence, permit to us to maximize the power density. In chapter 6 an hairpin solution has been proposed, until around 30% copper losses reduction is possible to achieve. The solution at moment is hard to manufacturer with an automatic line. Nowadays, the research interest is oriented in finding some solutions to make a flexible line to realize hairpin winding, in AUTO-MEA a Clean Sky 2 project many steps forward has been done.

As showed in chapter 6 which compare the random and hairpin winding adopted for the same electrical machine, it appears that it is very difficult to say which winding solution is better. The choice it depends a lot from the range frequency adopted, from the manufacturing facilities and from the experience of the designers.

Being necessary to drive the electrical machines through power electronic cause of winding overvoltages, in Chapter 7 a bidimensional model has been done to predict the overvoltage due to the presence of the power electronics. The model has been experimentally

evaluated and the match is quite good at least in the first periods of the signal being able to keep the right order of magnitude of the voltage.

REFERENCES

- [1] "BP Energy Outlook 2018, British Petroleum," ed, 2018. Available: <https://www.bp.com/en/global/corporate/energy-economics/energyoutlook.html>.
- [2] "A technical summary of Euro 6/VI vehicle emission standards," ed, 2016, Available: https://www.theicct.org/sites/default/files/publications/ICCT_Euro6VI_briefing_jun2016_.pdf
- [3] "Global EV Outlook 2018, International Energy Agency," ed, 2018, Available: https://www.theicct.org/sites/default/files/publications/ICCT_Euro6VI_briefing_jun2016_.pdf
- [4] M. Barcaro, "Design and Analysis of Interior Permanent Magnet Synchronous Machines for Electric Vehicles," University of Padova, 2011.
- [5] "EU FP7 Marie_Curie Initial Training network," ed, 2015, Available: <http://erean.eu/wordpress/rare-earth-magnets-still-optimum-choice-saysmotor-design-expert/>
- [6] W. Tong, Mechanical Design of Electric Motors. Taylor & Francis, 2014.
- [7] "Technical Data for Copper Magnet Wire by Size acc. to IEC 60317," ed, 2012, Available: <https://www.sis.se/api/document/preview/571790/>
- [8] <https://mswire.com/magnet-wire/coil-winding-wire/>
- [9] "NEMA Magnet Wire Thermal Class Ratings, Available: https://www.superioressex.com/uploadedFiles/News/White_Papers/emcwanema_magnet-thermal-class-ratings.pdf," ed.
- [10] P. E. Alexander, "Thermal classification of magnet wire in NEMA MW-1000," in 1983 EIC 6th Electrical/Electrical Insulation Conference, 1983, pp. 110-113.
- [11] "Technical data for winding wire, Available: <http://www.lww.se/wpcontent/uploads/2017/06/LWW-brochure-2016.pdf>," ed, 2016.
- [12] "LitzWire," ed., Available: <https://www.packlitzwire.com/products/litzwires/rupalitsafety>
- [13] M. G. MagNet Suite 7.8.3, "KB Article ID# MG601132," ed, 2018.
- [14] A. M. V.N. Mittle, Design of Electrical Machines. 2012.
- [15] M. Schiefer and M. Doppelbauer, "Indirect slot cooling for high-powerdensity machines with concentrated winding," in 2015 IEEE International Electric Machines Drives Conference (IEMDC), 2015, pp. 1820-1825.
- [16] M. van der Geest, H. Polinder, J. A. Ferreira, and D. Zeilstra, "Stator winding proximity loss reduction techniques in high speed electrical machines," in 2013 International Electric Machines Drives Conference, 2013, pp. 340-346.

- [17] A. Kampker, P. Burggräf, and C. Nee, "Costs, quality and scalability: Impact on the value chain of electric engine production," in 2012 2nd International Electric Drives Production Conference (EDPC), 2012, pp. 1-6.
- [18] M. Popescu and D. G. Dorrell, "Proximity Losses in the Windings of High Speed Brushless Permanent Magnet AC Motors with Single Tooth Windings and Parallel Paths," IEEE Transactions on Magnetics, vol. 49, no. 7, pp. 3913-3916, 2013.
- [19] H. M. Hamalainen, J. J. Pyrhonen, and J. Puranen, "Minimizing skin effect in random wound high-speed machine stator," in IEEE EUROCON 2009, 2009, pp. 752-757.
- [20] D. A. Gonzalez and D. M. Saban, "Study of the Copper Losses in a High-Speed Permanent-Magnet Machine with Form-Wound Windings," IEEE Transactions on Industrial Electronics, vol. 61, no. 6, pp. 3038-3045, June 2014.
- [21] A. D. Podoltsev, I. N. Kucheryavaya, and B. B. Lebedev, "Analysis of effective resistance and eddy-current losses in multiterm winding of high-frequency magnetic components," IEEE Transactions on Magnetics, vol. 39, no. 1, pp. 539-548, Jan 2003.
- [22] J. Pyrhonen, Design of rotating electrical machines / Juha Pyrhönen, Tapani Jokinen, Valéria Hrabovcová, Second edition. ed. 2014.
- [23] R. P. Wojda and M. K. Kazimierczuk, "Analytical Optimization of Solid- Round-Wire Windings," IEEE Transactions on Industrial Electronics, vol. 60, no. 3, pp. 1033-1041, March 2013.
- [24] P. H. Mellor, R. Wrobel, and N. McNeill, "Investigation of Proximity Losses in a High Speed Brushless Permanent Magnet Motor," in Conference Record of the 2006 IEEE Industry Applications Conference Forty-First IAS Annual Meeting, 2006, vol. 3, pp. 1514-1518.
- [25] C. R. Sullivan, "Optimal choice for number of strands in a litz-wire transformer winding," IEEE Transactions on Power Electronics, vol. 14, no. 2, pp. 283-291, March 1999.
- [26] J. Haldemann, "Transpositions in stator bars of large turbogenerators," IEEE Transactions on Energy Conversion, vol. 19, no. 3, pp. 553-560, Sept 2004.
- [27] J. Gyselinck, P. Dular, N. Sadowski, P. Kuo-Peng, and R. V. Sabariego, "Homogenization of Form-Wound Windings in Frequency and Time Domain Finite-Element Modeling of Electrical Machines," IEEE Transactions on Magnetics, vol. 46, no. 8, pp. 2852-2855, Aug 2010.
- [28] H. Hämäläinen, J. Pyrhönen, J. Nerg, and J. Talvitie, "AC Resistance Factor of Litz-Wire Windings Used in Low-Voltage High-Power Generators," IEEE Transactions on Industrial Electronics, vol. 61, no. 2, pp. 693-700, Feb 2014.
- [29] X. Thang and C. R. Sullivan, "Stranded wire with uninsulated strands as a low-cost alternative to litz wire," in IEEE 34th Annual Conference on Power Electronics Specialist, 2003. PESC '03., 2003, vol. 1, pp. 289-295 vol.1.
- [30] X. Nan and C. R. Sullivan, "An Equivalent Complex Permeability Model for Litz-Wire Windings," IEEE Transactions on Industry Applications, vol. 45, no. 2, pp. 854-860, March 2009.

- [31] P. B. Reddy, T. M. Jahns, and T. P. Bohn, "Transposition effects on bundle proximity losses in high-speed PM machines," in 2009 IEEE Energy Conversion Congress and Exposition, 2009, pp. 1919-1926.
- [32] M. van der Geest, H. Polinder, J. A. Ferreira, and D. Zeilstra, "Current Sharing Analysis of Parallel Strands in Low-Voltage High-Speed Machines," IEEE Transactions on Industrial Electronics, vol. 61, no. 6, pp. 3064-3070, June 2014.
- [33] https://e-magnetica.pl/file/proximity_effect_proximity_loss_magnetica.png.
- [34] P. B. Reddy, Z. Q. Zhu, S. H. Han, and T. M. Jahns, "Strand-level proximity losses in PM machines designed for high-speed operation," in 2008 18th International Conference on Electrical Machines, 2008, pp. 1-6.
- [35] P. B. Reddy, T. M. Jahns, and T. P. Bohn, "Modeling and analysis of proximity losses in high-speed surface permanent magnet machines with concentrated windings," in 2010 IEEE Energy Conversion Congress and Exposition, 2010, pp. 996-1003.
- [36] M. Klauz and D. G. Dorrell, "Eddy Current Effects in a Switched Reluctance Motor," IEEE Transactions on Magnetics, vol. 42, no. 10, pp. 3437-3439, Oct 2006.
- [37] M. Spang and M. Albach, "Optimized Winding Layout for Minimized Proximity Losses in Coils With Rod Cores," IEEE Transactions on Magnetics, vol. 44, no. 7, pp. 1815-1821, July 2008.
- [38] R. Wrobel, A. Mlot, and P. H. Mellor, "Contribution of End-Winding Proximity Losses to Temperature Variation in Electromagnetic Devices," IEEE Transactions on Industrial Electronics, vol. 59, no. 2, pp. 848-857, Feb 2012.
- [39] S. Iwasaki, R. P. Deodhar, Y. Liu, A. Pride, Z. Q. Zhu, and J. J. Bremner, "Influence of PWM on the Proximity Loss in Permanent-Magnet Brushless AC Machines," IEEE Transactions on Industry Applications, vol. 45, no. 4, pp. 1359-1367, 2009.
- [40] A. Fatemi, D. M. Ionel, N. A. O. Demerdash, D. A. Staton, R. Wrobel, and Y. C. Chong, "A computationally efficient method for calculation of strand eddy current losses in electric machines," in 2016 IEEE Energy Conversion Congress and Exposition (ECCE), 2016, pp. 1-8.
- [41] M. van der Geest, H. Polinder, J. A. Ferreira, and D. Zeilstra, "Stator winding proximity loss reduction techniques in high speed electrical machines," in 2013 International Electric Machines Drives Conference, 2013, pp. 340-346.
- [42] M. Popescu and D. G. Dorrell, "Proximity Losses in the Windings of High Speed Brushless Permanent Magnet AC Motors with Single Tooth Windings and Parallel Paths," IEEE Transactions on Magnetics, vol. 49, no. 7, pp. 3913-3916, 2013.
- [43] A. Lehtikoinen and A. Arkkio, "Efficient Finite-Element Computation of Circulating Currents in Thin Parallel Strands," IEEE Transactions on Magnetics, vol. 52, no. 3, pp. 1-4, March 2016.
- [44] A. Tessarolo, F. Agnolet, F. Luise, and M. Mezzarobba, "Use of Time-Harmonic Finite-Element Analysis to Compute Stator Winding EddyCurrent Losses Due to Rotor Motion in Surface Permanent-Magnet Machines," IEEE Transactions on Energy Conversion, vol. 27, no. 3, pp. 670- 679, 2012.

- [45] H. Rossmann, M. Doebroenti, M. Albach, and D. Exner, "Measurement and Characterization of High Frequency Losses in Nonideal Litz Wires," *IEEE Transactions on Power Electronics*, vol. 26, no. 11, pp. 3386-3394, Nov 2011.
- [46] P. B. Reddy and T. M. Jahns, "Analysis of bundle losses in high speed machines," in *The 2010 International Power Electronics Conference - ECCE ASIA -*, 2010, pp. 2181-2188.
- [47] D. Bauer, P. Mamuschkin, H. Reuss, and E. Nolle, "Influence of parallel wire placement on the AC copper losses in electrical machines," in *2015 IEEE International Electric Machines Drives Conference (IEMDC)*, 2015, pp. 1247-1253.
- [48] M. Vetuschi and F. Cupertino, "Minimization of Proximity Losses in Electrical Machines With Tooth-Wound Coils," *IEEE Transactions on Industry Applications*, vol. 51, no. 4, pp. 3068-3076, July 2015.
- [49] I. Petrov, M. Polikarpova, P. Ponomarev, P. Lindh, and J. Pyrhönen, "Investigation of additional AC losses in tooth-coil winding PMSM with high electrical frequency," in *2016 XXII International Conference on Electrical Machines (ICEM)*, 2016, pp. 1841-1846.
- [50] P. Arumugam, "Design Optimization on Conductor Placement in the Slot of Permanent Magnet Machines to Restrict Turn-Turn Short-Circuit Fault Current," *IEEE Transactions on Magnetics*, vol. 52, no. 5, pp. 1-8, May 2016.
- [51] A. Lehtikainen, N. Chiodetto, E. Lantto, A. Arkkio, and A. Belahcen, "Monte Carlo Analysis of Circulating Currents in Random-Wound Electrical Machines," *IEEE Transactions on Magnetics*, vol. 52, no. 8, pp. 1-12, 2016.
- [52] A. Vagati, G. Pellegrino and P. Guglielmi, "Comparison between SPM and IPM motor drives for EV application," *The XIX International Conference on Electrical Machines - ICEM 2010, Rome, 2010*, pp. 1-6.
- [53] G. Pellegrino, A. Vagati and P. Guglielmi, "Design Tradeoffs Between Constant Power Speed Range, Uncontrolled Generator Operation, and Rated Current of IPM Motor Drives," in *IEEE Transactions on Industry Applications*, vol. 47, no. 5, pp. 1995-2003, Sept.-Oct. 2011.
- [54] N. Bianchi and S. Bolognani, "Parameters and volt-ampere ratings of a synchronous motor drive for flux-weakening applications," in *IEEE Transactions on Power Electronics*, vol. 12, no. 5, pp. 895-903, Sept. 1997.
- [55] Clarich, Alberto, R. Russo, and M. Carriglio. "Multi-objective optimization with modefrontier interfaces for ansa and metapost." *4th ANSA & μ ETA International Conference*. Thessaloniki, Greece. 2011.
- [56] D. Gerada, A. Mebarki, N. L. Brown, C. Gerada, A. Cavagnino, A. Boglietti, "High speed electrical machines—Technologies trends and developments", *IEEE Trans. Ind. Electron.*, vol. 61, no. 6, pp. 2946-2959, Jun. 2014.
- [57] A. Krings and C. Monissen, "Review and Trends in Electric Traction Motors for Battery Electric and Hybrid Vehicles," *2020 International Conference on Electrical Machines (ICEM)*, Gothenburg, Sweden, 2020, pp. 1807-1813. doi:10.1109/ICEM49940.2020.9270946

- [58] "Electrical and Electronics Technical Team Roadmap," [Online]. Available: <https://www.energy.gov/sites/prod/files/2017/11/f39/EETT%20Roadmap%2010-27-17.pdf>, Accessed on: Dec. 12, 2018.
- [59] P. L. Dowell, "Effects of eddy currents in transformer windings," *Proc.IEE*, vol. 113, no. 8, pp. 1387–1394, Aug. 1966.
- [60] J. A. Ferreira, "Improved analytical modeling of conductive losses in magnetic components," in *IEEE Transactions on Power Electronics*, vol. 9, no. 1, pp. 127-131, Jan. 1994.
- [61] R. P. Wojda and M. K. Kazimierczuk, "Analytical optimization of solidround-wire windings," *IEEE Trans. Ind. Electron.*, vol. 60, no. 3, pp. 1033–1041, Mar. 2013
- [62] M. M. Liwschitz-Garik, "Computation of skin effect in bars of squirrelcage rotors," *Trans. Amer. Inst. Elect. Eng. Part III, Power App. Syst.*, vol. 74, no. 3, pp. 768–771, Jan. 1955.
- [63] A. Reatti and M. K. Kazimierczuk, "Comparison of various methods for calculating the AC resistance of inductors," *IEEE Trans. Magn.*, vol. 38, no. 3, pp. 1512–1518, May 2002.
- [64] T. Lubin, S. Mezani, and A. Rezzoug, "Analytical calculation of eddy currents in the slots of electrical machines: application to cage rotor induction motors," *IEEE Trans. Magn.*, vol. 47, no. 11, pp. 4650–4659, Nov. 2011.
- [65] L. J. Wu, Z. Q. Zhu, D. Staton, M. Popescu, and D. Hawkins, "Analytical model of eddy current loss in windings of permanent-magnet machines accounting for load," *IEEE Trans. Magn.*, vol. 48, no. 7, pp. 2138–2151, Jul. 2012.
- [66] C. Roth, F. Birnkammer and D. Gerling, "Analytical Model for AC Loss Calculation Applied to Parallel Conductors in Electrical Machines," 2018 XIII International Conference on Electrical Machines (ICEM), Alexandroupoli, 2018, pp. 1088-1094.
- [67] P. Mellor, R. Wrobel, D. Salt and A. Griffo, "Experimental and analytical determination of proximity losses in a high-speed PM machine," 2013 IEEE Energy Conversion Congress and Exposition, Denver, CO, 2013, pp. 3504-3511.
- [68] I. Petrov, M. Polikarpova, P. Ponomarev, P. Lindh and J. Pyrhönen, "Investigation of additional AC losses in tooth-coil winding PMSM with high electrical frequency," 2016 XXII International Conference on Electrical Machines (ICEM), Lausanne, 2016, pp. 1841-1846.
- [69] D. Bauer, P. Mamuschkin, H. Reuss and E. Nolle, "Influence of parallel wire placement on the AC copper losses in electrical machines," 2015 IEEE International Electric Machines & Drives Conference (IEMDC), Coeur d'Alene, ID, 2015, pp. 1247-1253.
- [70] A. Bardalai et al., "Reduction of Winding AC Losses by Accurate Conductor Placement in High Frequency Electrical Machines," in *IEEE Transactions on Industry Applications*, vol. 56, no. 1, pp. 183-193, Jan.-Feb. 2020.
- [71] H. Hämmäläinen, J. Pyrhönen and J. Nerg, "AC Resistance Factor in One-Layer Form-Wound Winding Used in Rotating Electrical Machines," in *IEEE Transactions on Magnetics*, vol. 49, no. 6, pp. 2967-2973, June 2013.
- [72] S. Xu and H. Ren, "Analytical Computation for AC Resistance and Reactance of Electric Machine Windings in Ferromagnetic Slots," in *IEEE Transactions on Energy Conversion*, vol. 33, no. 4, pp. 1855-1864, Dec. 2018

- [73] N. Bianchi and G. Berardi, "Analytical Approach to Design Hairpin Windings in High Performance Electric Vehicle Motors," 2018 IEEE Energy Conversion Congress and Exposition (ECCE), Portland, OR, 2018, pp. 4398-4405.
- [74] George E. P. Box, J. Stuart Hunter, William G. Hunter - *Statistics for Experimenters_ Design, Innovation, and Discovery*, Second Edition (2005).
- [75] Q. H. Quadri, S. Nuzzo, C. Gerada and M. Galea, "Analysis and Modelling of High Frequency Effects on Synchronous Generator's Armature Conductors," 2020 IEEE 29th International Symposium on Industrial Electronics (ISIE), Delft, Netherlands, 2020, pp. 253-258, doi: 10.1109/ISIE45063.2020.9152456.
- [76] P. Mellor, R. Wrobel and N. Simpson, "AC losses in high frequency electrical machine windings formed from large section conductors," 2014 IEEE Energy Conversion Congress and Exposition (ECCE), Pittsburgh, PA, 2014, pp. 5563-5570.
- [77] P. Giangrande, A. Galassini, S. Papadopoulos, A. Al-Timimy, G. L. Calzo, M. Degano, C. Gerada and M. Galea, "Considerations on the Development of an Electric Drive for a Secondary Flight Control Electromechanical Actuator," IEEE Transactions on Industry Applications, vol.55, no. 4, pp. 3544-3554, 2019.
- [78] A. Arzillo et al., "Challenges and Future opportunities of Hairpin Technologies," 2020 IEEE 29th International Symposium on Industrial Electronics (ISIE), Delft, Netherlands, 2020, pp.277-282. doi: 10.1109/ISIE45063.2020.9152417
- [79] A. Riedel et al., "Challenges of the Hairpin Technology for Production Techniques," 2018 21st International Conference on Electrical Machines and Systems (ICEMS), Jeju, 2018, pp. 2471-2476.
- [80] F. Wirth, T. Kirgor, J. Hofmann and J. Fleischer, "FE-Based Simulation of Hairpin Shaping Processes for Traction Drives," 2018 8th International Electric Drives Production Conference (EDPC), Schweinfurt, Germany, 2018, pp. 1-5.
- [81] N. Bianchi and G. Berardi, "Analytical Approach to Design Hairpin Windings in High Performance Electric Vehicle Motors," 2018 IEEE Energy Conversion Congress and Exposition (ECCE), Portland, OR, 2018, pp. 4398-4405.
- [82] P. Fyhr, G. Domingues, A. Reinap, M. Andersson and M. Alaküla, "Performance and manufacturability tradeoffs of different electrical machine designs," 2017 IEEE International Electric Machines and Drives Conference (IEMDC), Miami, FL, 2017, pp. 1-7.
- [83] M. Popescu, J. Goss, D. A. Staton, D. Hawkins, A. Boglietti, Y. C. Chong; "Electrical Vehicles - Practical Solutions for Power Traction Motor Systems," in IEEE Transactions on Industry Applications 2018
- [84] I. Lope, C. Carretero, J. Acero, R. Alonso and J. M. Burdio, "AC Power Losses Model for Planar Windings With Rectangular Cross-Sectional Conductors," in IEEE Transactions on Power Electronics, vol. 29, no. 1, pp. 23-28, Jan. 2014.
- [85] E. Preci et al., "Experimental Statistical Method Predicting AC Losses on Random Windings and PWM Effect Evaluation," in IEEE Transactions on Energy Conversion. doi: 10.1109/TEC.2020.3040265
- [86] D. B. Pinhal and D. Gerling, "A Review of the Analytical Calculation of the AC-Resistance of Armature Windings," 2020 23rd International Conference on Electrical Machines and Systems (ICEMS), Hamamatsu, Japan, 2020, pp. 906-911.

- [87] W. Zhang and T. M. Jahns, "Analytical model for predicting AC losses in form-wound machine windings due to stator current interactions," 2015 IEEE International Electric Machines & Drives Conference (IEMDC), Coeur d'Alene, ID, 2015, pp. 1131-1137.
- [88] E. Preci et al., "Rectangular and Random Conductors: AC Losses Evaluations and Manufacturing Considerations," IECON 2020 The 46th Annual Conference of the IEEE Industrial Electronics Society, Singapore, Singapore, 2020, pp. 1076-1081.
- [89] N. Bianchi and G. Berardi, "Analytical Approach to Design Hairpin Windings in High Performance Electric Vehicle Motors," 2018 IEEE Energy Conversion Congress and Exposition (ECCE), Portland, OR, 2018, pp. 4398-4405.
- [90] W. Zhang and T. M. Jahns, "Analytical 2-D slot model for predicting AC losses in bar-wound machine windings due to armature reaction," 2014 IEEE Transportation Electrification Conference and Expo (ITEC), Dearborn, MI, 2014, pp. 1-6.
- [91] E. Preci et al., "Hairpin Windings: Sensitivity Analysis and Guidelines to Reduce AC losses", proceeding on 2021 IEEE Workshop on Electrical Machines Design, Control and Diagnosis (WEMDCD), Modena, Italy, 2021.
- [92] C. Du-Bar, A. Mann, O. Wallmark and M. Werke, "Comparison of Performance and Manufacturing Aspects of an Insert Winding and a Hairpin Winding for an Automotive Machine Application," 2018 8th International Electric Drives Production Conference (EDPC), Schweinfurt, Germany, 2018, pp. 1-8.
- [93] M. S. Islam, I. Husain, A. Ahmed and A. Sathyan, "Asymmetric Bar Winding for High-Speed Traction Electric Machines," in IEEE Transactions on Transportation Electrification, vol. 6, no. 1, pp. 3-15, March 2020.
- [94] A. Arzillo et al., "An Analytical Approach for the Design of Innovative Hairpin Winding Layouts," 2020 International Conference on Electrical Machines (ICEM), Gothenburg, Sweden, 2020, pp. 1534-1539.
- [95] E. Preci et al., "Rectangular and Random Conductors: AC Losses Evaluations and Manufacturing Considerations," IECON 2020 The 46th Annual Conference of the IEEE Industrial Electronics Society, Singapore, 2020, pp. 1076-1081.
- [96] E. Preci et al., "Experimental Statistical Method Predicting AC Losses on Random Windings and PWM Effect Evaluation," in IEEE Transactions on Energy Conversion. doi: 10.1109/TEC.2020.3040265
- [97] <http://www.automea.unimore.it/>
- [98] H. Hämäläinen, J. Pyrhönen and J. Nerg, "AC Resistance Factor in One-Layer Form-Wound Winding Used in Rotating Electrical Machines," in IEEE Transactions on Magnetics, vol. 49, no. 6, pp. 2967-2973, June 2013.
- [99] J. A. Ferreira, "Improved analytical modeling of conductive losses in magnetic components," in IEEE Transactions on Power Electronics, vol. 9, no. 1, pp. 127-131, Jan. 1994.

- [100] M. van der Geest, H. Polinder, J. A. Ferreira and D. Zeilstra, "Stator winding proximity loss reduction techniques in high speed electrical machines," 2013 International Electric Machines & Drives Conference, Chicago, IL, USA, 2013, pp. 340-346.
- [101] J. P. Holman, Heat Transfer. New York: McGraw-Hill, 1997
- [102] E. Preci *et al.*, "Rectangular and Random Conductors: AC Losses Evaluations and Manufacturing Considerations," *IECON 2020 The 46th Annual Conference of the IEEE Industrial Electronics Society*, Singapore, 2020, pp. 1076-1081. doi: 10.1109/IECON43393.2020.9254278
- [103] K. Shirabe *et al.*, "Advantages of high frequency PWM in AC motor drive applications," 2012 IEEE Energy Conversion Congress and Exposition (ECCE), Raleigh, NC, 2012, pp. 2977-2984.
- [104] K. S. Boutros, R. Chu and B. Hughes, "GaN power electronics for automotive application," 2012 IEEE Energytech, Cleveland, OH, 2012, pp. 1-4.
- [105] G. Skibinski, D. Leggate and R. Kerkman, "Cable characteristics and their influence on motor over-voltages," Proceedings of APEC 97 - Applied Power Electronics Conference, Atlanta, GA, USA, 1997, pp. 114-121 vol.1.
- [106] G. Pietrini, D. Barater, C. Concari, M. Galea and C. Gerada, "Closed-form approach for predicting overvoltage transients in cable-fed PWM motor drives for MEA," 2016 IEEE Energy Conversion Congress and Exposition (ECCE), Milwaukee, WI, 2016, pp. 1-7. doi: 10.1109/ECCE.2016.7854917.
- [107] J. He, G. Y. Sizov, P. Zhang and N. A. O. Demerdash, "A review of mitigation methods for overvoltage in long-cable-fed PWM AC drives," 2011 IEEE Energy Conversion Congress and Exposition, Phoenix, AZ, 2011, pp. 2160-2166.
- [108] A. von Jouanne and P. N. Enjeti, "Design considerations for an inverter output filter to mitigate the effects of long motor leads in ASD applications," in *IEEE Transactions on Industry Applications*, vol. 33, no. 5, pp. 1138-1145, Sept.-Oct. 1997.
- [109] M. J. Scott *et al.*, "Reflected wave phenomenon in motor drive systems using wide bandgap devices," 2014 IEEE Workshop on Wide Bandgap Power Devices and Applications, Knoxville, TN, 2014, pp. 164-168.
- [110] L. Ru and L. Ying-zi, "A kind of new simulation of electric field distribution in a PWM inverter-fed motor stator winding subjected to steep-fronted surge voltages," 2011 6th IEEE Conference on Industrial Electronics and Applications, Beijing, 2011, pp. 2787-2790.
- [111] L. Wang, C. Ngai-Man Ho, F. Canales and J. Jatskevich, "High-Frequency Modeling of the Long-Cable-Fed Induction Motor Drive System Using TLM Approach for Predicting Overvoltage Transients," in *IEEE Transactions on Power Electronics*, vol. 25, no. 10, pp. 2653-2664, Oct. 2010. doi: 10.1109/TPEL.2010.2047027.
- [112] G. Skibinski, "Design methodology of a cable terminator to reduce reflected voltage on AC motors," IAS '96. Conference Record of the 1996 IEEE Industry Applications Conference Thirty-First IAS Annual Meeting, San Diego, CA, USA, 1996, pp. 153-161 vol.1.

- [113] P. Mart-ro, W. Sae-Kok and S. Khomfoi, "Analysis of dv/dt filter installation for PWM AC drive applications," 2011 IEEE Ninth International Conference on Power Electronics and Drive Systems, Singapore, 2011, pp. 177-184. doi: 10.1109/PEDS.2011.6147243.
- [114] H. Kim, B. Kim and S. Bhattacharya, "An Analytical Design Strategy and Implementation of a Dv/Dt Filter for WBG Devices Based High Speed Machine Drives," IECON 2018 - 44th Annual Conference of the IEEE Industrial Electronics Society, Washington, DC, 2018, pp. 385-390. doi: 10.1109/IECON.2018.8591737.
- [115] J. He et al., "Multi-Domain Design Optimization of dv/dt Filter for SiC-Based Three-Phase Inverters in High-Frequency Motor-Drive Applications," 2018 IEEE Energy Conversion Congress and Exposition (ECCE), Portland, OR, 2018, pp. 5215-5222.
- [116] C. Vadstrup, X. Wang and F. Blaabjerg, "LC filter design for wide band gap device based adjustable speed drives," 2014 International Power Electronics and Application Conference and Exposition, Shanghai, 2014, pp. 1291-1296. doi: 10.1109/PEAC.2014.7038049.
- [117] M. M. Swamy and M. A. Baumgardner, "New Normal Mode dv/dt Filter With a Built-In Resistor Failure Detection Circuit," in IEEE Transactions on Industry Applications, vol. 53, no. 3, pp. 2149-2158, May-June 2017. doi: 10.1109/TIA.2017.2672519.
- [118] T. G. Habetler, R. Naik and T. A. Nondahl, "Design and implementation of an inverter output LC filter used for dv/dt reduction," in IEEE Transactions on Power Electronics, vol. 17, no. 3, pp. 327-331, May 2002. doi: 10.1109/TPEL.2002.1004240.
- [119] R. Mini, S. R. Resna and M. N. Dinesh, "LC clamp filter for voltage reflection due to long cable in induction motor drives," 2014 Annual International Conference on Emerging Research Areas: Magnetics, Machines and Drives (AICERA/icMMD), Kottayam, 2014, pp. 1-6.
- [120] Y. Liu, L. Wang, H. Gao, H. Zhang and D. Xu, "Overvoltage mitigation of submersible motors with long cables of different lengths," 2014 17th International Conference on Electrical Machines and Systems (ICEMS), Hangzhou, 2014, pp. 638-644.
- [121] N. B. Elsayed, M. E. Ibrahim and M. A. Izzularab, "Mitigation of Overvoltages at Induction Motor Terminals Fed from an Inverter Through Long Cable," 2018 Twentieth International Middle East Power Systems Conference (MEPCON), Cairo, Egypt, 2018, pp. 595-602.
- [122] K. K. Yuen and H. S. Chung, "A Low-Loss "RL-Plus-C" Filter for Overvoltage Suppression in Inverter-Fed Drive System With Long Motor Cable," in IEEE Transactions on Power Electronics, vol. 30, no. 4, pp. 2167-2181, April 2015. doi: 10.1109/TPEL.2014.2325824.
- [123] X. Chen, D. Xu, F. Liu and J. Zhang, "A Novel Inverter-Output Passive Filter for Reducing Both Differential- and Common-Mode dv/dt at the Motor Terminals in PWM Drive Systems," in IEEE Transactions on Industrial Electronics, vol. 54, no. 1, pp. 419-426, Feb. 2007.

APPENDIX I

Current feed 14A peak				
N. of Strand	Current Magnitude[A] (100Hz)	Current Phase[deg] (100Hz)	Current Magnitude[A] (1000Hz)	Current Phase [deg] (1000Hz)
std_1	0.3225	120.1707	1.4907	55.4069
std_2	0.3123	123.5903	1.2845	56.4774
std_3	0.3033	127.3562	1.0627	56.1116
std_4	0.2966	130.5625	0.8935	58.3325
std_5	0.2968	130.7627	0.8982	61.0247
std_6	0.2904	135.1495	0.6687	62.9771
std_7	0.2931	133.2445	0.7817	64.6410
std_8	0.2853	140.2952	0.4336	72.8716
std_9	0.2868	138.8261	0.5303	74.8621
std_10	0.2842	142.2109	0.3868	85.2137
std_11	0.2827	145.6857	0.2676	106.2678
std_12	0.2841	142.9230	0.3956	92.8664
std_13	0.2829	145.9057	0.3015	111.2562
std_14	0.2827	148.7372	0.2850	137.3870
std_15	0.2830	150.7003	0.3026	155.2289
std_16	0.2836	145.6505	0.3579	112.3733
std_17	0.2830	147.7654	0.3136	128.3960
std_18	0.2838	153.0753	0.3789	169.6308
std_19	0.2832	151.9412	0.3439	163.1039
std_20	0.2863	157.8326	0.5398	-169.3068
std_21	0.2848	155.4351	0.4455	-177.2674
std_22	0.2903	161.8625	0.6979	-157.2514
std_23	0.2840	149.5010	0.3798	141.2501
std_24	0.2838	148.3380	0.3559	133.1618
std_25	0.2923	163.4509	0.7798	-156.8086
std_26	0.2856	155.9823	0.4785	-176.7925
std_27	0.2947	165.1303	0.8525	-152.4830
std_28	0.2917	162.5267	0.7506	-160.2148
std_29	0.2930	163.9012	0.7974	-154.9253
std_30	0.2942	164.5212	0.8289	-154.5316
std_31	0.2963	165.9291	0.8978	-153.1514
std_32	0.2923	163.2944	0.7701	-155.9107
std_33	0.3173	175.7477	1.4164	-143.2975
std_34	0.2936	164.4193	0.8147	-152.0885
std_35	0.3203	176.7372	1.4790	-143.9528

TABLE A1. Magnitude and phase values of the current through the parallel strands.

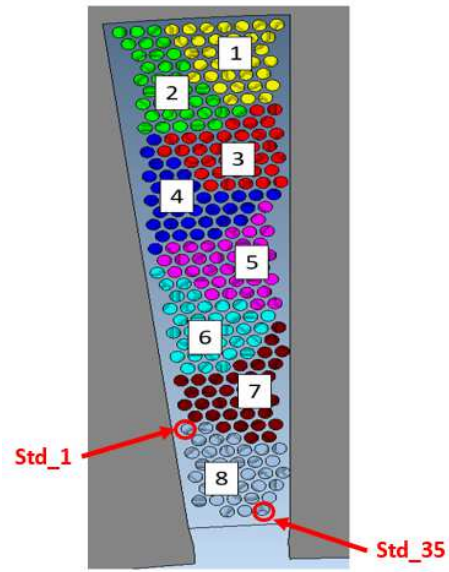


Fig.A1.1. Parallel strand positions.

APPENDIX 2

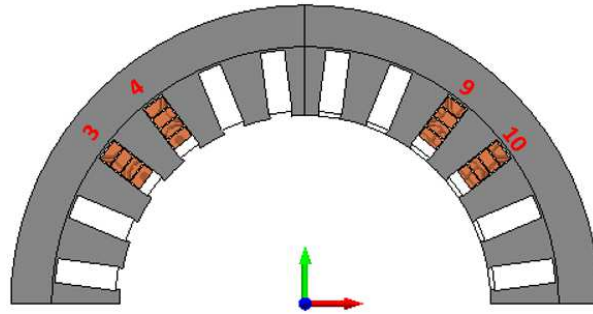


Fig. A2.1. Motorette cross section with $q=2$ and $K=4$.

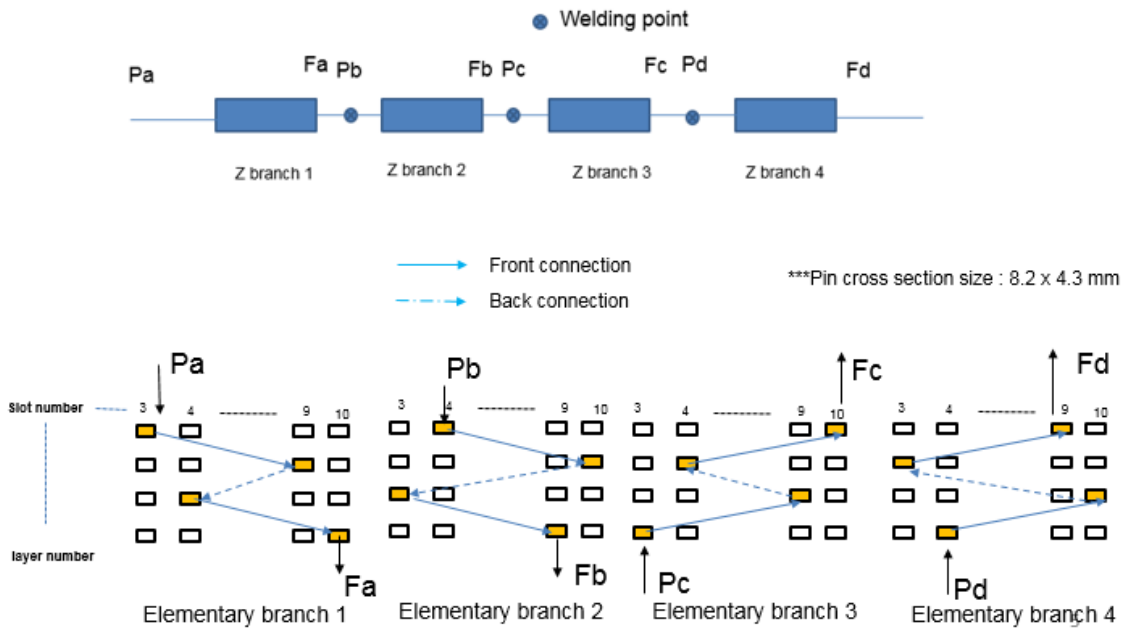


Fig. A2.2. Hairpin wiring diagram connection with $q=2$ and $K=4$.

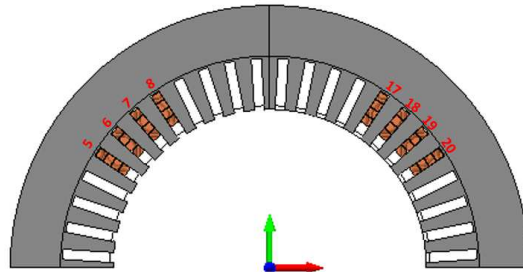


Fig. A2.3. Motorette cross section with $q=4$ and $K=4$.

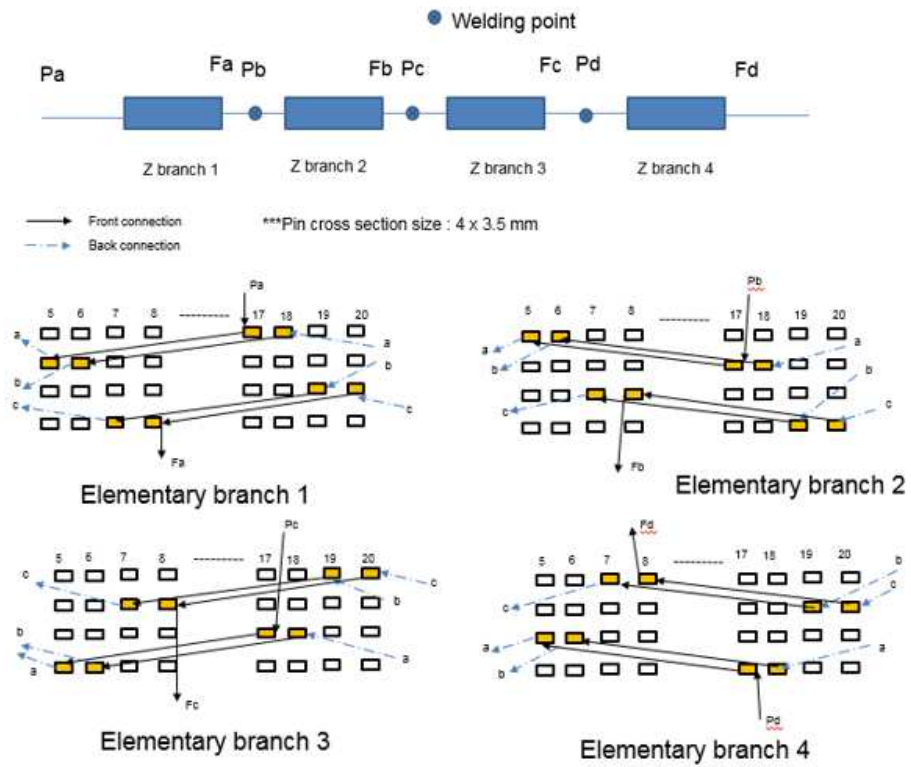


Fig. A2.4. Hairpin wiring diagram connection and electrical scheme, with $q=4$ and $K=4$.

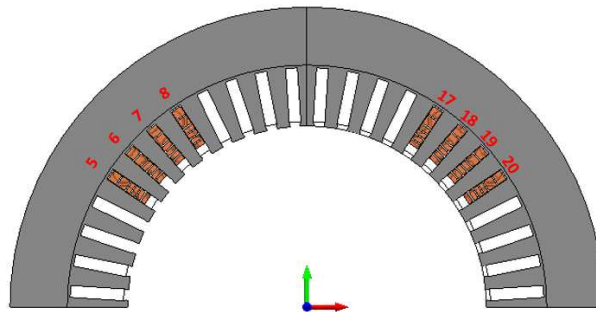


Fig. A2.5. Motorette cross section with $q=4$ and $K=4$ segmented.

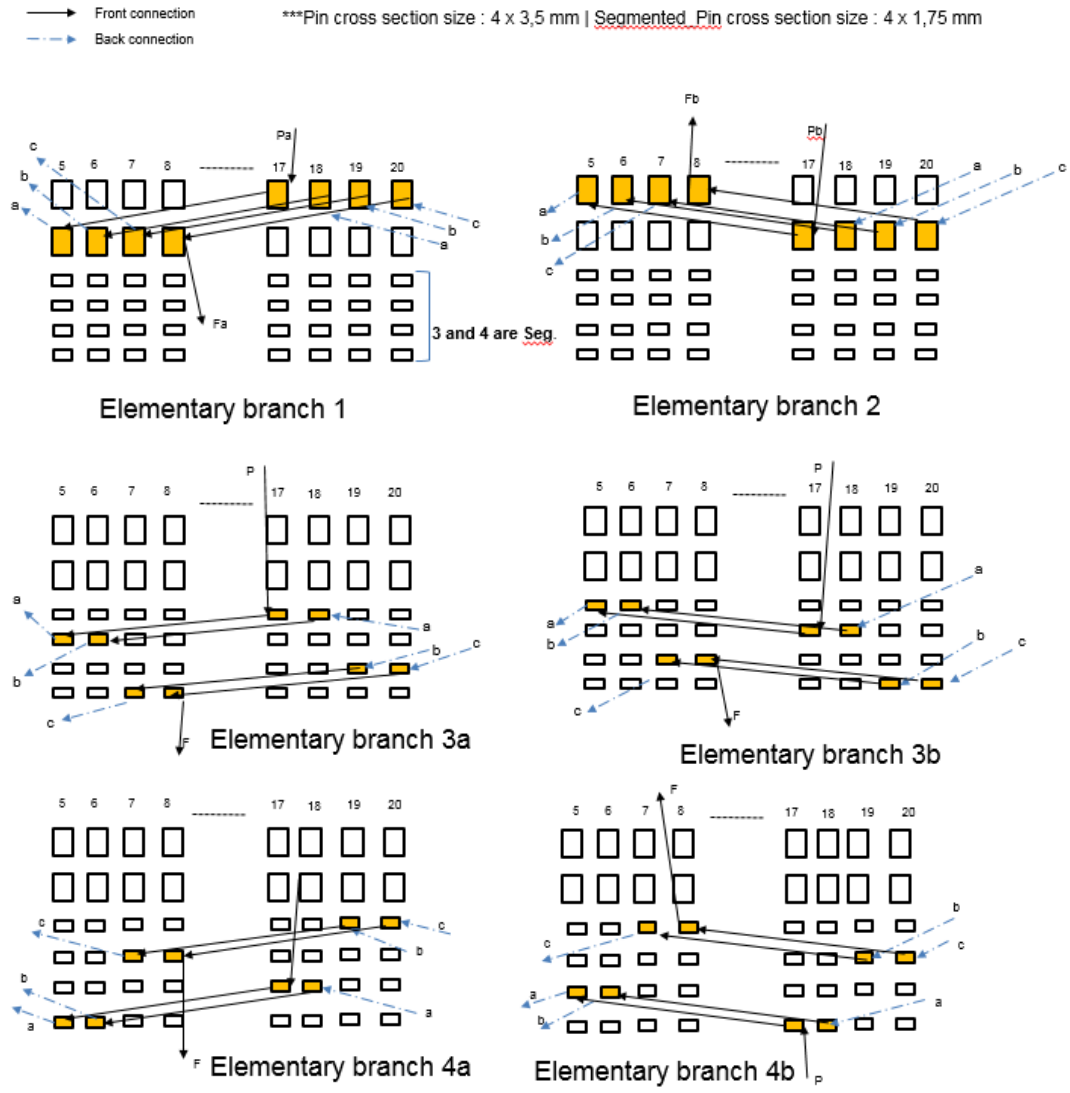


Fig. A2.6. Hairpin wiring diagram connection with $q=4$ and $K=4$ segmented.

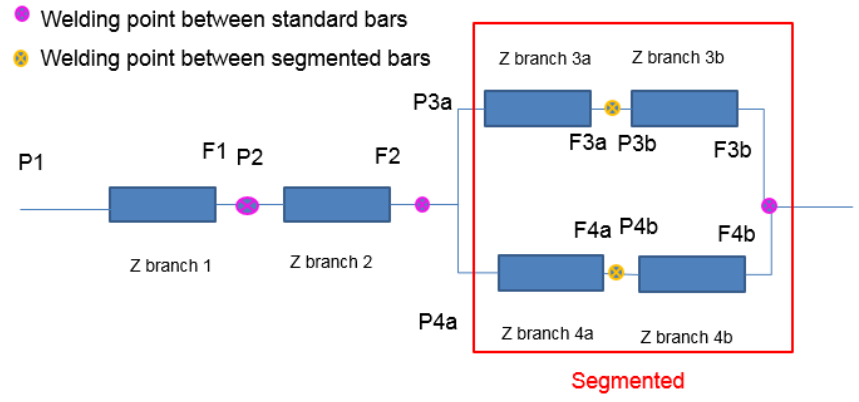


Fig. A2.7. Electrical scheme of the wiring connections with $q=4$ and $K=4$ segmented.

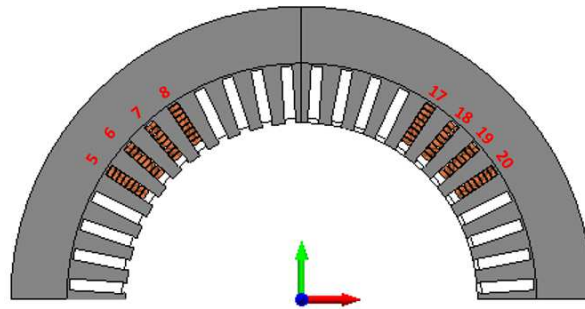


Fig. A2.8. Motorette cross section with $q=4$ and $K=8$.

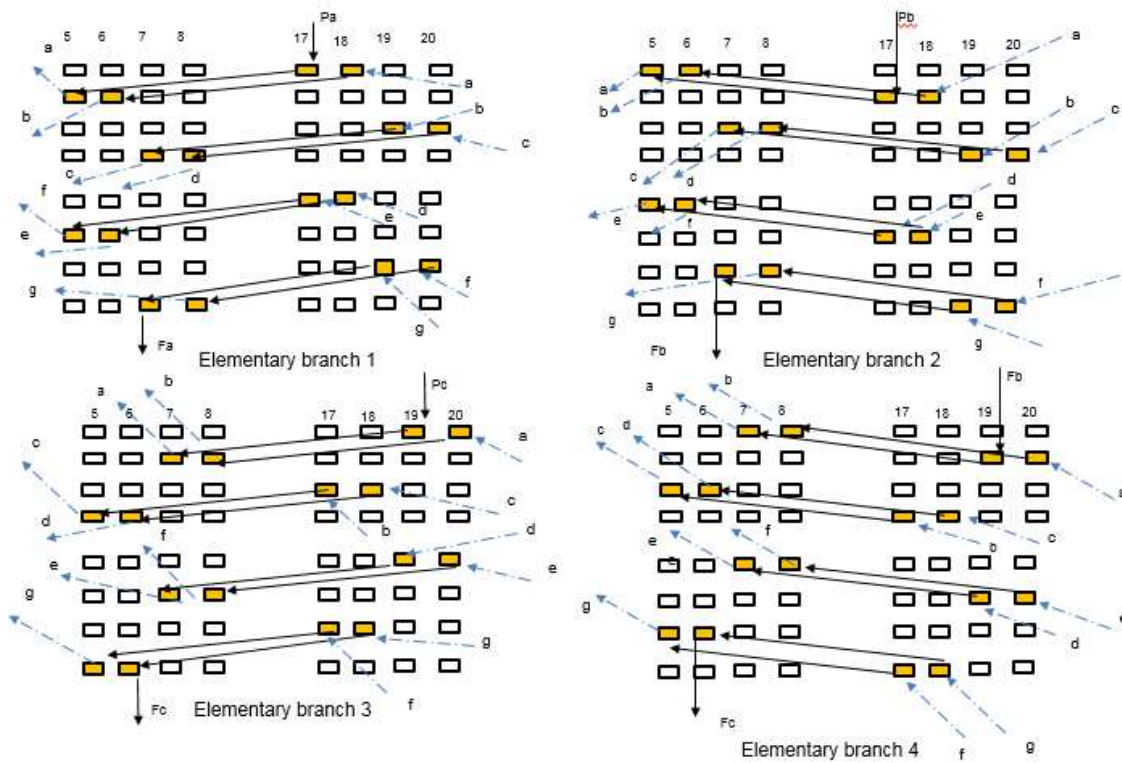


Fig. A2.9. Hairpin wiring diagram connection with $q=4$ and $K=8$.

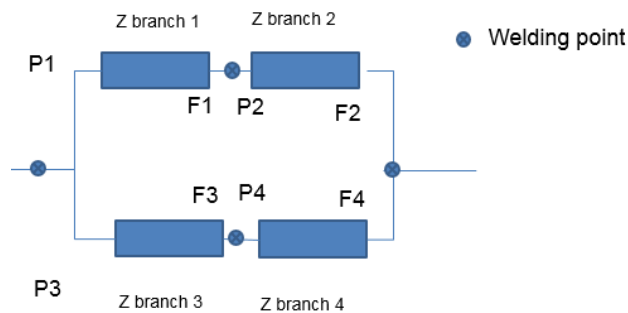


Fig. A2.10. Electrical scheme of the wiring connections with $q=4$ and $K=8$